



UNIL | Université de Lausanne

Unicentre

CH-1015 Lausanne

<http://serval.unil.ch>

---

*Year : 2017*

## DEVELOPMENT OF SYNTHETIC CHEMOTAXIS BASED BACTERIAL BIOREPORTERS

Roggo Clémence

Roggo Clémence, 2017, DEVELOPMENT OF SYNTHETIC CHEMOTAXIS BASED BACTERIAL BIOREPORTERS

Originally published at : Thesis, University of Lausanne

Posted at the University of Lausanne Open Archive <http://serval.unil.ch>

Document URN : urn:nbn:ch:serval-BIB\_7C8C3CFFF8261

### **Droits d'auteur**

L'Université de Lausanne attire expressément l'attention des utilisateurs sur le fait que tous les documents publiés dans l'Archive SERVAL sont protégés par le droit d'auteur, conformément à la loi fédérale sur le droit d'auteur et les droits voisins (LDA). A ce titre, il est indispensable d'obtenir le consentement préalable de l'auteur et/ou de l'éditeur avant toute utilisation d'une oeuvre ou d'une partie d'une oeuvre ne relevant pas d'une utilisation à des fins personnelles au sens de la LDA (art. 19, al. 1 lettre a). A défaut, tout contrevenant s'expose aux sanctions prévues par cette loi. Nous déclinons toute responsabilité en la matière.

### **Copyright**

The University of Lausanne expressly draws the attention of users to the fact that all documents published in the SERVAL Archive are protected by copyright in accordance with federal law on copyright and similar rights (LDA). Accordingly it is indispensable to obtain prior consent from the author and/or publisher before any use of a work or part of a work for purposes other than personal use within the meaning of LDA (art. 19, para. 1 letter a). Failure to do so will expose offenders to the sanctions laid down by this law. We accept no liability in this respect.



**UNIL** | Université de Lausanne

Faculté de biologie  
et de médecine

**Département de Microbiologie Fondamentale**

# **DEVELOPMENT OF SYNTHETIC CHEMOTAXIS BASED BACTERIAL BIOREPORTERS**

**Thèse de doctorat ès sciences de la vie (PhD)**

présentée à la

Faculté de biologie et de médecine  
de l'Université de Lausanne

par

**Clémence ROGGO**

Master of Science en sciences moléculaires du vivant  
de l'Université de Lausanne

**Jury**

Prof. Bengt Kayser, Président  
Prof. Jan Roelof van der Meer, Directeur de thèse  
Prof. Victor de Lorenzo, expert  
Prof. Victor Sourjik, expert

Lausanne 2017



UNIL | Université de Lausanne

Faculté de biologie  
et de médecine

Ecole Doctorale

Doctorat ès sciences de la vie

# Imprimatur

Vu le rapport présenté par le jury d'examen, composé de

<i>Président·e</i>	Monsieur	Prof. Bengt Kayser
<i>Directeur·rice de thèse</i>	Monsieur	Prof. Jan Roelof Van der Meer
<i>Experts·es</i>	Monsieur	Prof. Victor De Lorenzo
	Monsieur	Prof. Victor Sourjik

le Conseil de Faculté autorise l'impression de la thèse de

**Madame Clémence Roggo**

Master en Sciences moléculaires du vivant de l' Université de Lausanne

intitulée

**DEVELOPMENT OF SYNTHETIC CHEMOTAXIS  
BASED BACTERIAL BIOREPORTERS**

Lausanne, le 22 septembre 2017

pour le Doyen  
de la Faculté de biologie et de médecine

Prof. Bengt Kayser







# TABLE OF CONTENT

<b>SUMMARY (English)</b>	<b>iii</b>
<b>RESUME (Français)</b>	<b>vii</b>
<b>CHAPTER 1</b>	<b>1</b>
General introduction	
<b>CHAPTER 2</b>	<b>33</b>
Quantitative chemical sensing by bacterial chemotaxis in microfluidic chips	
<b>CHAPTER 3</b>	<b>69</b>
Characterization of single cell chemotaxis responses using a microfluidic chip	
<b>CHAPTER 4</b>	<b>91</b>
Engineering a split-Gfp fusion to measure CheY and CheZ interaction	
<b>CHAPTER 5</b>	<b>123</b>
Measuring proton flow from chemotaxis through the cytoplasmic membrane using pH-sensitive fluorescent protein	
<b>CHAPTER 6</b>	<b>145</b>
Changing chemotaxis specificity of <i>Escherichia coli</i> by introducing heterologous methyl-accepting chemoreceptors	
<b>CHAPTER 7</b>	<b>169</b>
General discussion	
<b>CURRICULUM VITAE AND PUBLICATION LIST</b>	<b>179</b>
<b>ACKNOWLEDGEMENTS</b>	<b>183</b>



# SUMMARY

With increasing industrialization and the increasing amount of chemical compounds produced every day, the need of a proper monitoring of the environment is crucial. The use of biosensors based on living microorganisms is an interesting alternative to common chemical analysis. Since microorganisms are easy and cheap to produce, and thanks to their small size, they can be implemented in miniaturized portable devices, which may be used directly in the field. Common whole-cell bacterial bioreporters produce an easy detectable signal by induction of expression of a reporter protein in presence of either a specific molecule or a general stress reaction. Whole-cell bioreporter analysis is robust, but requires a couple of hours to obtain a clear reporter signal.

In this thesis, we envisioned to develop bacterial biosensors based on a different physiological response than *de novo* gene expression that could lead to a faster response time while keeping target sensitivity and specificity. In particular, we tried to exploit chemotaxis, the behaviour of motile bacteria to sense their environment and swim in the direction of or away from chemical compounds. Chemotaxis is rapid (sec–min scale) and some species show naturally chemotaxis towards compounds of environmental interest.

In Chapter 2, we quantified bacterial chemotaxis from direct measurements of cellular motility. We developed a microfluidic chip, which generated a stable attractant gradient and into which motile bacteria could be added. The bacteria sensed the chemical gradient and accumulated where the concentration of attractant is highest. Accumulation of cells was quantified over time by epifluorescence microscopy. As a proof of concept, we used chemotaxis of *Escherichia coli* towards serine, aspartate and methylaspartate. Notably, *E. coli* accumulated to 10  $\mu\text{M}$  serine within 10 minutes, but showed maximum accumulation to 100  $\mu\text{M}$  serine after 20 minutes or longer. Secondly, we quantified chemotaxis of *Cupriavidus pinatubonensis* JMP134 to 2,4-dichlorophenoxyacetate, a commonly used herbicide. Unfortunately, accumulation of



JMP134 was not very sensitive and could only be observed with 1 mM 2,4-dichlorophenoxyacetic acid or higher. Steady-state chemodynamic and chemotaxis modelling was used to support the observed cellular response in the microfluidic chip as a function of attractant concentration.

In Chapter 3, we wanted to facilitate the manipulation of the microfluidic chip by the development of a different chip that integrates valves inside the structure. This could facilitate the control of the liquid flow inside the chip, as well as enable sample exchange. By focusing on individual cell movement, we expected we might achieve very short response times upon addition of attractants. The gradient was generated by alternating valve opening and motile *E. coli* were inserted in the middle of this pre-established gradient. Individual cell trajectories were monitored in the few first minutes of response. Contrary to our expectations, no significant difference in trajectory characteristics was measured in presence compared to absence of a gradient. Mathematical simulations of single cell chemotaxis response suggested that more time is required to observe cell accumulation, or that cells would have to be introduced closer to the source.

In Chapter 4, I focused on chemotaxis responses at the molecular and single cell level by measuring CheY–CheZ interactions. I fused two non-fluorescent parts of the green fluorescent protein (Gfp) to CheY and CheZ, components of chemotaxis pathway. I could demonstrate that Gfp fluorescent foci appear in single cells as a genuine interaction between CheY and CheZ. By mutant analysis, I showed that foci form mostly at the motor complex and less frequently at the sites of chemoreceptors. Not completely unexpected, the reformed split-Gfp was relatively stable and little dynamics in position or fluorescent intensity of foci was detected. However, single cell analysis indicated that the turnover of split-Gfp is more important immediately after addition of 100  $\mu$ M nickel as repellent.

In Chapter 5, I attempted to measure chemotaxis response through pH changes at single cell levels. Notably, the flagellar motor is powered by an influx of protons through the cytoplasmic membrane. I deployed the pH-sensitive fluorescent protein pHluorin, either expressed inside the cytoplasm or in the periplasm of *E. coli*, to measure pH differences in chemotactically active cells. For this, I used a modified agarose-block test as attractant and recorded fluorescent changes in accumulating cells. Interestingly, a 100  $\mu$ M serine source induced an increase of pH in the cytoplasm and a decrease in the periplasm in cells close to the source, but not in cells further away. This suggests an active export of protons from the cytoplasm to the periplasm during chemotaxis in order to compensate for the increased flux needed for the flagellar motors.

Finally in chapter 6, I attempted to change *E. coli* chemotaxis specificity by introducing receptors coming from *Pseudomonas putida*. I focused on two *P. putida* receptors, one for benzoate and the other for toluene. I demonstrated expression of both receptors in *E. coli* – although we cannot be completely certain that the proteins inserted into the membrane. Agarose-block tests with serine, toluene and benzoate, in comparison to no attractants, showed that *E. coli* cell accumulation close to a source of toluene was significantly higher in strains expressing the toluene receptor. *E. coli* without benzoate receptor accumulated as well as those with benzoate receptor near sources with benzoate.

In this work, we investigated different approaches to exploit chemotaxis in order to produce biosensing signals. Our results are promising and show that functional biosensors based on chemotaxis may be achieved in a variety of ways.



# RESUME

En raison de l'avancée de l'industrialisation et de l'augmentation du nombre et de la quantité de composés chimiques produits chaque jour, la surveillance de la pollution touchant notre environnement est cruciale. L'utilisation de biosenseurs basés sur des micro-organismes vivants est une alternative intéressante aux analyses chimiques couramment utilisées. Ces micro-organismes sont faciles et peu coûteux à produire et, grâce à leur petite taille, ils peuvent être facilement implémentés dans des appareils miniaturisés et portables pouvant être utilisés directement sur le terrain. Les biorapporteurs bactériens usuels produisent un signal facilement détectable conséquence de l'induction de l'expression d'une protéine rapportrice en présence d'une molécule spécifique ou en réponse à un stress. Les biorapporteurs sont des outils d'analyse robustes mais requièrent quelques heures pour obtenir un signal clair.

Dans cette thèse, nous avons eu pour but de développer des biosenseurs bactériens basés sur une autre réponse physiologique que l'expression *de novo* de gènes, ceci dans le but de produire une réponse plus rapide tout en conservant la sensibilité et la spécificité pour la molécule cible. En particulier, nous avons exploité le chimiotactisme, soit le comportement des bactéries mobiles qui peuvent sentir leur environnement et se déplacer pour s'approcher ou s'éloigner de composés chimiques. Le chimiotactisme présente l'avantage de fournir une réponse rapide, prenant de quelques secondes à quelques minutes. De plus, certaines espèces bactériennes sont connues pour montrer naturellement une attraction pour des composés d'intérêt environnemental comme des polluants.

Dans le chapitre 2, nous avons quantifié le chimiotactisme bactérien par mesure directe de la mobilité cellulaire. Nous avons développé une puce micro-fluidique qui génère un gradient stable d'attractant dans lequel des bactéries mobiles peuvent être ajoutées. Les bactéries sentent le gradient chimique et s'accumulent là où la concentration d'attractant est la plus élevée. Cette accumulation de cellules est quantifiée au cours du temps par microscopie à épifluorescence. Comme preuve de concept, nous avons utilisé le chimiotactisme d'*Escherichia coli* vers la sérine,

l'aspartate et le méthylaspartate. *E. coli* est attiré par 10  $\mu\text{M}$  de sérine en 10 minutes, mais montre une accumulation maximale avec 100  $\mu\text{M}$  de sérine après au moins 20 minutes. Nous avons également quantifié le chimiotactisme de *Cupriavidus pinatubonensis* JMP134 pour le 2,4-dichlorophenoxyacetate, un herbicide communément utilisé. Malheureusement JMP134 n'était pas très sensible et la réponse n'a pu être observée qu'avec un minimum de 1 mM de 2,4-dichlorophenoxyacetate. La modélisation mathématique du chimiotactisme en fonction de la concentration d'attractant a été utilisée pour appuyer les résultats obtenus expérimentalement en utilisant la puce micro-fluidique.

Dans le chapitre 3, nous avons voulu faciliter la manipulation de la puce micro-fluidique en développant un autre type de puce qui intègre des valves à l'intérieure de leur structure. Cela facilite le contrôle du flux de liquide dans la puce, et permet ainsi un potentiel échange d'échantillons. En se focalisant sur le mouvement de cellules individuelles, nous nous attendions à obtenir un temps de réponse plus court après l'ajout d'attractant. Le gradient d'attractant est généré par des ouvertures alternées des valves et des cellules d'*E. coli* sont ensuite insérées au milieu du gradient préétabli. Les trajectoires de cellules individuelles sont enregistrées pendant les premières minutes de réponse. Contrairement à nos attentes, aucune différence significative dans les caractéristiques des trajectoires n'a été mesurée en présence ou en absence de gradient. Des simulations mathématiques de la réponse chimiotactique de cellules individuelles suggère la nécessité d'un plus long temps d'observation ou encore d'introduire les cellules plus proche de la source d'attractant.

Dans le chapitre 4, nous nous sommes focalisés sur le chimiotactisme aux niveaux cellulaire et moléculaire en mesurant l'interaction entre deux acteurs de la signalisation. Pour cela, deux parties non-fluorescentes de la protéine fluorescente verte (GFP) ont été fusionnées aux protéines CheY et CheZ, composants de la signalisation du chimiotactisme. J'ai pu démontrer que les *foci* de fluorescence apparaissant dans les cellules individuelles montrent l'interaction entre

CheY et CheZ. Par l'analyse de mutants, j'ai montré que les *foci* se forment principalement au niveau du moteur des flagelles et moins fréquemment au niveau des récepteurs. La GFP reformée lors de l'interaction de CheY et CheZ est relativement stable et se révèle peu dynamique dans la position ou dans l'intensité de fluorescence des *foci*. Néanmoins, l'analyse des cellules individuelles indique que le turnover de la GFP est plus important immédiatement après ajout de 100  $\mu\text{M}$  de nickel, utilisé comme substance répulsive.

Dans le chapitre 5, j'ai mesuré la réponse chimiotactique à travers les changements de pH au niveau des cellules individuelles. Le moteur des flagelles est énergisé par un influx de protons à travers la membrane cytoplasmique. J'ai donc exprimé une protéine fluorescente sensible au pH, la pHluorin, soit dans le cytoplasme ou le périplasme d'*E. coli* et mesuré les différences de pH dans des cellules actives pour le chimiotactisme. Pour cela, j'ai utilisé un bloc d'agarose contenant la source d'attractant et mesuré les changements de fluorescence des cellules attirées. Une source de 100  $\mu\text{M}$  de serine induit une augmentation du pH dans le cytoplasme et inversement, une diminution dans le périplasme dans les cellules proches de la source mais pas dans les cellules plus éloignées. Cela suggère un export actif de protons depuis le cytoplasme dans le périplasme pendant le chimiotactisme afin de compenser l'augmentation de l'influx de protons nécessaire à la rotation des flagelles.

Finalement dans le chapitre 6, j'ai changé la spécificité du chimiotactisme d'*E. coli* en y introduisant des récepteurs venant de *Pseudomonas putida*. Je me suis intéressée à deux récepteurs de *P. putida*, l'un liant le benzoate et l'autre le toluène. J'ai démontré que l'expression des deux récepteurs se fait de façon correcte chez *E. coli*, même si l'on ne peut pas être complètement certain que les protéines soient correctement repliées ou encore bien insérées dans la membrane. Les tests par bloc d'agarose contenant la sérine, le toluène ou le benzoate en comparant à l'absence d'attractant, montrent que l'accumulation d'*E. coli* proche de la source est significativement plus important pour la souche exprimant le récepteur pour le toluène. D'autre

part, la souche n'exprimant pas le récepteur au benzoate s'accumule aussi bien que la souche avec récepteur autour d'une source de benzoate.

Dans ce travail, nous avons investigué différentes approches pour exploiter le chimiotactisme dans le but de produire des signaux par des biosenseurs bactériens. Nos résultats sont prometteurs et montrent que des biosenseurs fonctionnels basés sur le chimiotactisme peuvent être obtenu par différentes approches.

# CHAPTER 1

## GENERAL INTRODUCTION

Parts published previously as Roggo, C. and J.R. van der Meer, *Miniaturized and integrated whole cell living bacterial sensors in field applicable autonomous devices*. *Curr Opin Biotechnol*, 2017.

**45:** p. 24-33.



## Introduction

Increasing industrialization in human societies leads to more and more chemical compounds being released into and finishing in the environment. As many of those compounds are toxic at low concentrations, their increased presence in all environmental compartments increases the likelihood of harm caused to human health, plant and animal life. Monitoring of chemicals in the environment is thus critical in order to identify regions of elevated concentrations and to unveil concealed pollution sources. Monitoring results can subsequently be used as basis for appropriate pollution mitigation, treatment or removal strategies [1, 2]. The most common method for environmental monitoring is to have fixed stations sampling at regular intervals or to conduct periodical field sampling campaigns. Samples of different matrices (aqueous, soil, air or other) are then transported to the laboratory to analyze their chemical content with advanced methods and instruments (e.g., solid-phase micro-extraction, gas chromatography coupled to mass spectrometry). These methods give excellent results, but are expensive and time-consuming, and their sampling strategies do not easily capture temporal and spatial dynamics of the contamination. Increasingly, therefore, fixed or manual sampling is replaced by mobile samplers (e.g., gliders, drones, buses or ships) equipped with miniaturized sensors focusing on a single or small, defined group of target chemicals, in order to, ultimately, allow real-time assessment of recurring pollutants [3-5].

The development of sensors that are sufficiently small, target-specific and precise, and which can fit miniaturized mobile samplers, is an active field of research that requires integration and collaboration between various disciplines. One of the possible types of sensors that may be integrated in mobile and autonomous samplers are those based on living cells or live microorganisms [6]. The major incentive for deploying live cells in sensors is that they reproduce to some extent the biological effects expected to occur in living organisms exposed to or in the (contaminated) environment [7, 8]. Whereas biological effects can be manifold and difficult to discern, in particular the design of synthetic implanted genetic circuits inside live cells (microorganisms or other) has enabled to target specific compounds, compound groups, as

well as general distress pathways, with the concomitant output of an easily detectable signal [9-12]. There is more than two decades experience with bioassays based on live microorganisms or *bioreporters* (as they are more commonly referred to), which therefore appear to be an interesting option for miniaturized sensor development. Bioreporters based on bacteria or yeast are, in principle, extremely easy to reproduce and cheap compared to conventional analytical machines. Due to their small size (1-20  $\mu\text{m}$ ) and low population numbers needed for signal detection ( $10^4$ - $10^6$  cells), the integration of bioreporters into field applicable miniaturized and autonomous devices is a realistic option. Nonetheless, important technical and biological challenges remain before such mobile and autonomous live-biosensor devices can be routinely deployed.

In this chapter, we describe recent attempts to integrate bioreporters into miniaturized devices while focusing on the specific obstacles challenging their field deployment. We will first discuss the different signal outputs of bioreporters and their connection to small integrated detectors. Then we will briefly explore recent studies demonstrating survival, long-term maintenance and activity of bioreporter cells, which may be used to obtain longer biosensor instrument shelf-lives. Finally, we will present some examples of integrated bioreporter instruments and critically review potential field deployment of automated biosensors.

### **Generating the signal: transmission between live bioreporters and detectors**

The principle of a bioreporter is to produce an easy detectable signal that changes in presence of or upon exposure to the target compound(s). Bioreporter cells are frequently equipped with purposely designed genetic circuits allowing the production of a cellular sensor (protein or aptamer) that can influence expression from the reporter gene [13, 14]. To achieve this, the reporter gene itself is fused directly or via some relay to a specific promoter that is controlled by the cellular sensor (for a very simplified conceptual idea, see Fig. 1A). Details of synthetic circuitry design have been reviewed elsewhere and will not be repeated here [15, 16]. The outcome of the reaction of an exposed bioreporter cell is a proportional production of the

reporter protein as a function of the target compound availability (concentration or flux) in the sample (Fig. 2A) [17, 18].

Reporter proteins come in a wide variety of flavors and their activity or spectroscopic properties (e.g., color, fluorescence, bioluminescence) is routinely detected with macro-size instruments. Miniaturization of bioreporter assays into devices, however, leads to lower overall signal intensity from the cells, and requires both improved signal transmission to the detector and detector sensitivity. The type of coupling depends to a large extent on the type of reporter protein or biological signal [18, 19]. Frequently, fluorescence is used as output for bioreporters, being produced from genes for autofluorescent proteins that are non-native to the cell. This results in their specific fluorescence being detected at high sensitivity without too much interference from other fluorescing molecules in the cell. Specific genetic design, however, may be needed to reduce background reporter gene expression in the circuit in absence of the target, in order to obtain the highest signal-to-noise ratio in the assay (see, for example, Ref [20, 21]). In most bioreporter designs, exposure to the target compound induces an increase in the expression of the fluorescent protein. The increase is to some extent dose-dependent and allows the establishment of a calibration curve, from which the target's presence in the environmental sample can be deduced (Fig. 2A). Importantly, because of the inherent flexibility and cross-reactivity of the cellular sensors on which bioreporters are based, the cells inevitably react to compound classes rather than a single individual chemical. Consequently, bioreporter reactions to unknown samples can only be interpreted from calibration curves as concentrations *equivalent* to the effect provoked by known target chemicals, when incubated with the bioreporter cells under the same conditions and assay duration. For illustration, the well-known bacterial bioreporters to mercury or arsenic are relatively compound specific, but respond slightly differently depending on Hg or As chemical speciation [22, 23]. An extreme case of compound unspecificity is formed by yeast and bacterial bioreporters for genotoxicity, which react to any type of molecule or condition resulting in DNA damage [12]. The fluorescent signal produced by such reporters upon sample exposure can only be interpreted as reaction

equivalent to exposure to defined concentrations of known DNA damaging agents (e.g., nalidixic acid) [23, 24]. Fluorescence from bioreporters can be relatively easily detected by specific illumination through inexpensive laser or light emitting diodes, selective filters, collimating lenses and photodiode detectors that are sufficiently small (mm-size) to allow fabrication of a miniaturized biosensor [25, 26].

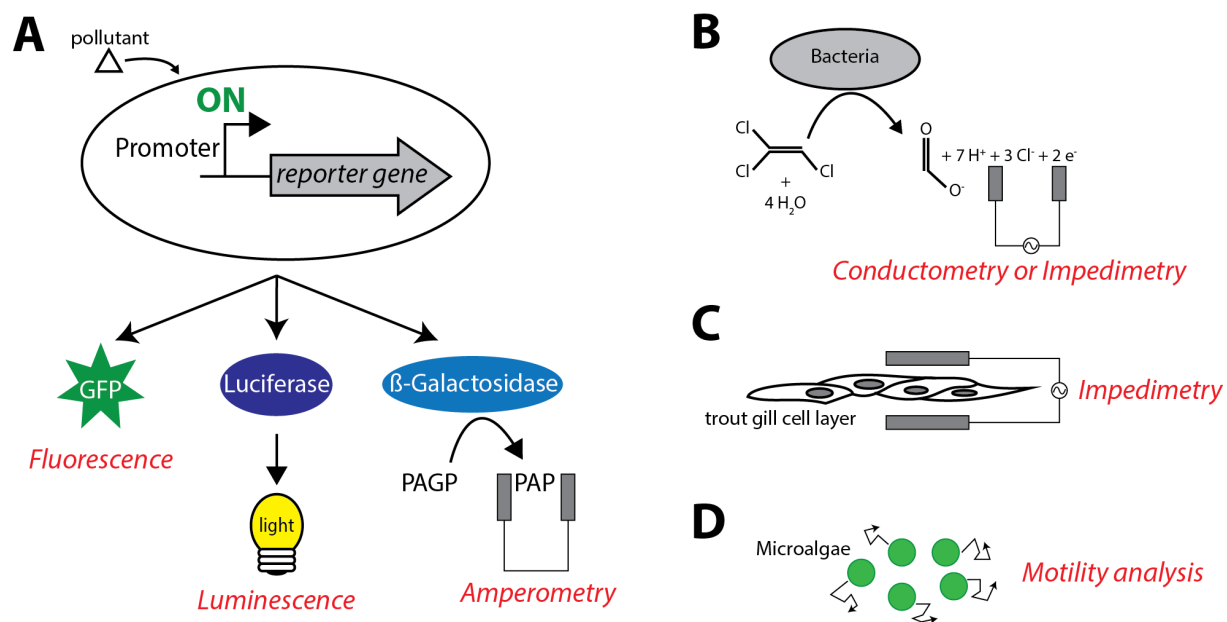


**Figure 1: Concept of live-cell based assays and their output. (A)** Bioreporter cells are genetically engineered to carry a synthetic DNA construct permitting to sense a polluting chemical (or condition) and turn on expression of a reporter gene. The output of the reporter protein can be measured by e.g., fluorescence, luminescence or by electrochemistry. **(B)** Electron release from native enzymes, such as toluene dioxygenase, can be measured by conductivity or impedance, and can be used to measure the presence of trichloroethylene [26, 27]. **(C)** Release of tight cell-cell junctions as a measure for toxicity response can be detected by impedance [28, 29]. **(D)** Changes in random cell motility can be used for detecting the presence of heavy metals [30].

Bioluminescence is also a commonly used output for bioreporters because it is - again, non-native to most cells, which have no bioluminescence background themselves, and is easily detectable with light detectors. Numerous different bioluminescence-based bacterial bioreporters have been developed that detect diverse compound classes and which have been used for environmental analysis [31-34]. Both the concept of increase of light production in presence of the target, as well as decreasing light production have been used [35, 36]. Increasing light production allows coupling to a specific signaling chain of events leading to *de novo* reporter gene induction, as explained above for fluorescence-based bioreporters. This has the advantage of measuring an increase of signal intensity against low background, but the disadvantage of requiring induction time (in practice mostly longer than 30 min). The decreasing light production bioreporter is based on fact that the light-emitting enzyme (luciferase) is highly dependent on cellular ATP levels. Any change in the physiological state of the bioreporter cells that impacts ATP levels as a consequence of sample exposure will thus be almost instantly detected in the level of luminescence emitted [37]. The principle is deployed in the commercial Microtox® acute toxicity test that uses the natural bioluminescent bacterium *Allovibrio fischeri*, but has been adapted in newer studies for potential integration in microdevices. In a recent example, Roda *et al.* [36] expressed constitutively a red-emitting luciferase in *Magnetospirillum gryphiswaldense* strain MSR-1, which may be used for more easy on-chip manipulation through magnetic cell concentration (see below). The *M. gryphiswaldense* cells showed dose-dependent decrease of bioluminescence with increasing concentrations (2.5 % - 40 %) of dimethyl-sulfoxide and (0.1-10 mM) of taurochenodeoxycholic acid, a detergent bile acid that impairs membrane stability [36]. Although bioluminescence is very sensitive it used to require rather expensive photomultiplier or charge-coupled detectors that were not so easy to miniaturize (alternative concepts have appeared, see below). More recently, miniaturized photomultiplier detectors have appeared on the market, whose size (2×4 mm) enables capturing light signals from bioreporters in e.g., tiny incubation wells or microfluidic devices.

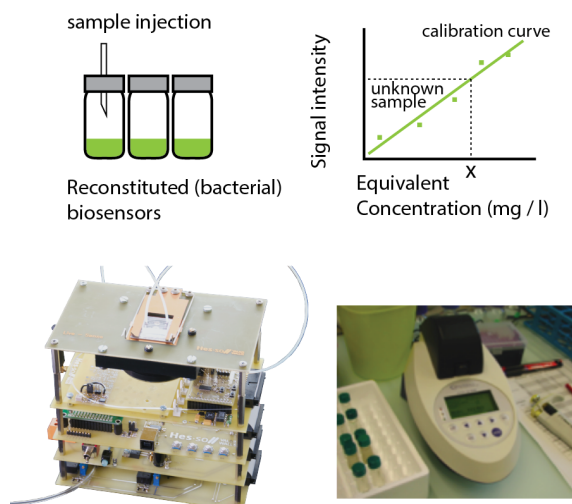
Finally, the activity of certain reporter proteins, such as beta-galactosidase, can be captured through electrochemistry [18, 38]. This is interesting because no optical device is needed to illuminate or detect the reporter signal (Fig. 1A). Instead, reporter activity can be recorded by electrodes that can be miniaturized and integrated into microfluidic devices, easily multiplexed to obtain multisample capacity. As example, Cortes-Salzar *et al.* used a commercial electrode-integrated microdevice with 16-wells to measure the induction of beta-galactosidase by *Escherichia coli* bioreporter cells in presence of arsenic [39]. Beta-galactosidase can catalyze cleavage of *p*-aminophenyl- $\beta$ -galactopyranoside into *p*-aminophenol, which is an electrochemically active species detectable by amperometry. The results from the electrochemical biosensor on groundwater samples were in good agreement with arsenic measurements conducted with atomic absorption spectroscopy [39]. A disadvantage of the beta-galactosidase electrochemical reaction is that it requires substrate addition, which may complicate fluidic flows in a miniaturized device. Electrochemical detection does not necessarily require specific reporter proteins but can probe other (natural) cellular pathways in a label-free sensitive manner (Fig. 1B). For example, Hnaïen *et al.* measured trichloroethylene and toluene presence from electrons released during transformation by the toluene dioxygenase in *Pseudomonas putida* F1 cells, using conductometry [26] or impedimetry [27]. Changes in impedance are also a global measure for distress caused by toxicant exposure to surface-grown eukaryotic cell layers, which results in disruption of tight cell-cell-junctions and increased ion flux (Fig. 1C, see elsewhere in this issue) [28, 29].

### **Immobilization techniques to retain the responsiveness of live cell sensors.**

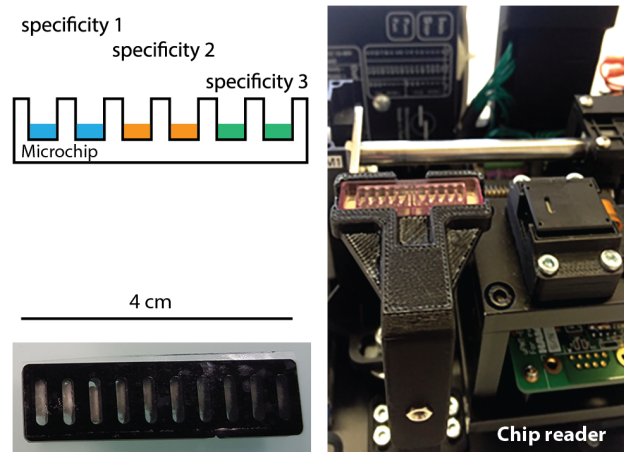
In order to develop autonomous and integrated live-cell biosensors, it is crucial to maintain or restore the cells in a physiologically active state at the time of exposure to the sample [40]. This is a non-trivial issue, since most bioreporters are developed in rapidly growing species such as *E. coli*, which tend to survive better in stationary phase, but are poorly inducible

in that state [41]. Essentially three approaches have appeared to tackle this issue. The first approach is to lyophilize or encapsulate the bioreporter cells in such a state that both good survival and (immediate) inducibility upon contact to the sample are guaranteed. The second approach is to exploit species with different biological properties allowing them to naturally survive well (e.g., sporulation) and/or retain immediate activation (e.g., fish cell lines or algae adapted to lower temperatures [29, 42, 43]). The third alternative is to maintain a constant pool of actively growing cells that can be deployed for instant sample measurements [44, 45]. All three approaches have specific requirements in terms of their integration into small sensor devices.

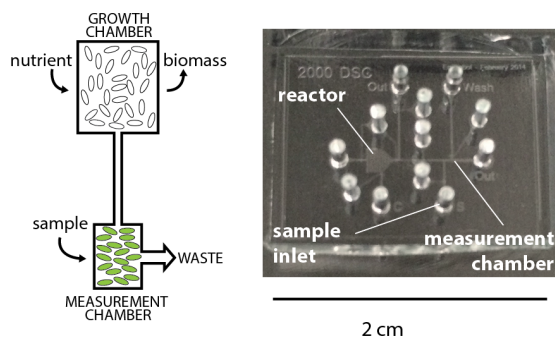
**A** Single measurement



**B** Multiplexing for measurements with multiple strains



**C** Multiple measurements



**D** Continuous measurements

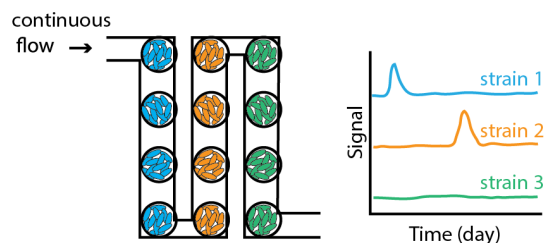


**Figure 2: Concepts for conducting integrated live-cell measurements in microstructures.**

**(A)** Single use devices with single type bioreporter strains [46, 47]. Cells can be preserved

through lyophilization or encapsulation. A calibration series is conducted in parallel, from which the equivalent concentration in an unknown sample can be derived. Picture on the left shows a standalone device to measure fluorescence from agarose-bead immobilized *E. coli* cells for arsenic detection (reproduced with permission from ref. [25]). Picture on the right: an example of a portable field luminometer with incubation vials (Picture by the authors). **(B)** Multiplexed single use device to contain multiple different types of bioreporters [48]. Picture below shows a ten-well microchip for bioluminescence measurements. Picture to the right shows a compact luminometer reader for such chips (Pictures: Courtesy of Yoann le Digabel, University of Lausanne). **(C)** Constant growth devices, allowing multiple consecutive sample measurements with new batches of cells, and kinetic detection of the reporter signal [41]. Picture in the middle shows a PDMS chip with a microreactor and measurement zone (Picture courtesy: Siham Beggah, University of Lausanne). **(D)** Continuous measurements over multi-strain devices with slow-decay of the reporter protein in absence of a target compound in the sample, as in the example of Ref. [49].

Bioreporter lyophilization has allowed excellent and reproducible results, at least in closed milliliter-size vials and multi-well structures. In this strategy the bioreporter cells are first cultured, washed and pretreated with cryoprotecting agents, aliquoted and lyophilized, and then kept under specific storage conditions to optimally retain cellular survival and activity. The assay is started by injecting the aqueous sample or extract into the vial with the dried bioreporters to revive the cells, which are subsequently incubated for the necessary time duration to develop the reporter signals [46]. Ideally, the vials with the dried bioreporters require minimal liquid handling, fit directly the detector for the reporter signal and remain "closed" at all times, in order to be legally considered as a closed-system (with genetically modified organisms, Fig. 2A). The concept was successfully demonstrated by e.g., Siegfried and co-workers, who assayed dozens of groundwaters in the field in Bangladesh and Argentina for the presence of arsenic with single-use lyophilized cells in glass vials [46, 47]. Although single-



use vials per sample seems time- and labor-intensive, the authors showed that sample analysis could be massively parallelized, allowing rapid screening of all potable water wells in e.g., a small village in an afternoon. Furthering this concept, Yagur-Kroll *et al.* deposited and lyophilized six different fluorescence-based bacterial bioreporters on a porous 1.5 × 3 cm aluminum oxide chip with 3 mm diameter wells that was fixed in a flow cell for exposure to the sample [50]. Their procedure enabled long-term storage (3 months) of the chips while maintaining good bioreporter induction after sample contact. One could imagine lyophilizing and preserving bioreporter cells in even much smaller sealed chip microcavities, which are punctured and automatically filled to revive the cells and start sample analysis. After the measurement is completed the chip with the cells can be inactivated and destroyed.

Cellular immobilization and encapsulation have also been extensively used to preconcentrate and maintain bioreporter cells in an active physiological state. This has been adapted to microfluidic compartments to allow precise sample flow or reagent mixing across the cells, and to enhance subsequent signal detection. For example, Axelrod and coworkers developed a sensor "pad" with bioreporters encapsulated in 4 mm diameter alginate beads, which are loaded in a glass well and exposed to the sample [51]. By encapsulating the bioreporter cells in alginate beads the bioluminescent signal remained confined to a smaller area [51]. Ahn and coworkers encapsulated different bioreporter strains, which were mixed and differentiated in a single assay by co-immobilization of different color fluorescent beads [52]. In another study, Buffi *et al.* encapsulated *E. coli* bioreporter cells in 50 μm diameter agarose beads, which were loaded into a permeable 'cage' on a microfluidic chip [53]. This permitted easy sample flow over the bioreporters and yielded a more concentrated signal from the cells in a specific zone on the chip. Preloading of reporter cell-encapsulated beads on the chip enabled storage at -20 °C for a month, whereupon the cells rapidly regained activity by simple preflushing of nutrient solution during 30 min before starting sample analysis [54]. The aforementioned genotoxicity yeast reporter was used for microfluidic embodiment with help of

coated magnetic nanoparticles, which facilitated cell concentration in a specific chamber by a magnet [23]. Also the constant-ON bioluminescent reporter in the naturally magnetic strain *M. gryphiswaldense* MSR1 enabled easy liquid and cell manipulation by magnetism in a microfluidic device [36]. Immobilized bioreporter cells have also successfully been deposited and printed on surfaces in order to obtain multi-analyte arrays (Fig. 2B) that can give a "fingerprint" of a contaminated sample. Melamed *et al.* printed nanoliter spots of *E. coli* bioreporter bacteria on different types of surface (polystyrene, PVC and glass), which remained responsive even after 2 months of storage at 4 °C [55].

To exploit the natural capacity of some species for long-term survival, some groups have developed bioreporter bacteria in spore-forming bacteria such as *Bacillus subtilis* or *Bacillus megaterium*. In this case, the vegetative cells are pregrown, spore formation is induced and the spores are preserved and loaded in the assay device. Before sample exposure, the spores are again germinated to vegetative cells, and these subsequently react to the target chemical [56, 57]. Studies showed examples of spore-based *Bacillus* bioreporters producing GFP upon induction with arsenic and zinc in blood serum or water samples within 2.5 to 3 h [58], or to indicate spoilage of packaged meat [56, 57].

As an alternative to preservation it is also possible to maintain reporter cells in a constant active state by continuous growth and cell division [44, 45]. Continuous bacterial growth can be achieved in e.g., chemostats, allowing constant growth rates, and recent studies have shown that these can be miniaturized to mm<sup>2</sup>-scale or smaller, embedded in microfluidic structures [59-61]. The bioreporter cells are inoculated into the micro-reactors and cultured as in macro-size chemostats, with constant inflow of nutrients and removal of excess biomass (Fig. 2C). A recent study then showed that it is possible to use the constantly grown biomass for sample analysis [41]. For this purpose a two-layered microfluidic chip was fabricated with integrated valves in order to more easily manipulate the pressure-driven nutrient, cell and sample flows on the chip. Cells were removed from the micro-reactor into a specifically designed

sample exposure chamber, with filter channels so small that bioreporter cells were retained but liquid sample passes through. The pre-concentrated bioreporter cells were brought here in contact with the sample and induced the reporter protein, which was visible more easily because of the confined spot of accumulated cells. After measurement, the cells were washed from exposure chamber upon which a next measurement could be started with fresh cells transported from the micro-reactor into the exposure chamber. The authors demonstrated the working principle of the microchemostat sensor chip and showed that multiple sample measurements could be performed during one week with the same *E. coli* bioreporter batch [41].

### **Toward integrated autonomous biosensor instruments**

There is thus ample proof of successful miniaturization of bioreporter assays into microstructures, signal perception by integrated detectors and of bioreporter cells preserved in such a way to allow storage and/or semi-continuous measurements in integrated small devices. A few integrated systems have appeared and allow a first assessment of their deployment and measurement capacity [4]. Many specific questions and challenges remain, however, some of which we will elude to below. A first important distinction is whether a system is designed for single-use disposable cartridges or enables multiple consecutive measurements. Several of the examples discussed above allow single-use measurement; others may permit multiple measurements in parallel or consecutively. Single-use disposable cartridges with integrated microfluidics, prefilled and preserved bioreporter cells that are activated by the sample could be useful for hand-held devices. These may be deployed by people in field situations needing near real-time measurements of e.g., water quality. As a proof-of-concept, Truffer and colleagues developed a small ( $10 \times 16 \times 25 \text{ cm}^3$ ) fully integrated device that holds a single-use fluidic biochip with bioreporter cells encapsulated in agarose beads as in Ref [53] inside flow cages [62]. A pumping system brings the aqueous sample in contact with the bioreporters, and integrated optics excite, collect and read the fluorescence signal at short time intervals during three hours, after which the results can be send and displayed on a mobile phone. This chip carried two

parallel fluidic lines and cages, allowing duplicate measurements of the sample. In addition, the system allowed an estimation of the number of reporter cells in beads through light scattering, which can be used to normalize signal variations resulting from different cell numbers in the assay. Despite the success of the proof-of-principle standalone bacterial biosensor to measure arsenic in water samples, the essential problem in the single-use disposable cartridge remains the signal calibration. Since the bioreporter signal development depends on the duration and conditions of the assay, and the amount (and quality) of bioreporter cells in the assay, one cannot immediately interpret the actual target concentration in the sample from only a single (or duplicate) assay. At least one calibration standard would have to be measured independently to compare to the sample output, unless one could guarantee the exact performance of preserved batches of bioreporter cells.

Addition of calibration standards and of blank samples (without the target) to be measured simultaneously with one (or more) unknown samples facilitates the interpretation of results, but requires multiplexing the miniaturized assay in separate parallel cavities. This was successfully done, e.g., in the electrochemical bioreporter assays mentioned above using the commercial 16-well minidevice to measure arsenic in aqueous samples [39]. However, this device still required manual liquid handling and interpretation of results. Alternatively, some form of internal calibration may be carried out even on single sample measurements by spiking known concentrations of the target compound and comparing both signals in time.

Multiplexing has also been used to develop (single use) miniaturized assays with bioreporters carrying different target specificities. This is illustrated by the work of Tsai *et al.*, who developed a 16-well chip that contained multiple bioreporters reacting to different toxicants [48]. The 16-wells with the bacteria were etched in an aluminum chip, with an oxygen-permeable microfluidic channel on top to bring the sample in contact with the bioreporter cells. A linear charged-coupled device (CCD) camera captured the bioluminescence from the cells, and was integrated in a 15×30 cm<sup>2</sup> footprint portable device that further automatically computed the results by a custom-developed program in *python*. As proof of principle, the authors loaded

two *E. coli* bioreporter strains, one for genotoxicity and the other targeting nitroaromatic compounds. They showed dose-dependent responses of both strains and further demonstrated how 2 or 4 samples can be analyzed in parallel [48].

A general toxicity portable device with single use exchangeable assays-on-chip was also developed for rainbow trout gill cells and successfully used to detect major toxicants in water [29]. These cell lines are not equipped with synthetic reporter gene circuits but toxic effects can be judged from impedance changes on mono-layered cells through loss of tight junctions. Cells can thus be pregrown on top of electrode pads integrated in a fluidic chip, that can be stored at 4°C for several months without loss of activity of the cells [28]. The chip contains separate channels for a control and a sample measurement and is inserted in a portable impedance reader (14×22.9×8.9 cm<sup>3</sup>). The reader measures impedance every minute during one hour and displays whether the sample is 'contaminated' or 'not contaminated' (i.e., being significantly different from the control channel). The system appears to be robust although toxicant concentrations need to be quite high for the fish cells to respond within the 1 h response time.

Systems with single-use disposable cartridges are feasible as long as manual operations are intended, but they become much more cumbersome in automated remotely operated instruments. In that case the instrument itself will have to (i) fill the sample in the cartridges, (ii) run the measurement, (iii) collect and integrate (or report) the data, (iv) remove the cartridge after use and (v) renew the cartridge from some storage unit for subsequent measurement. In addition, the instrument may have to carry standard solutions for calibration, nutrient solutions to revive cells, pretreat the sample and so on. Alternatively, the instrument may use a multi-use biosensor unit, which simplifies the automated handling of single-use cartridges. Very little experience yet exists with instruments that can carry out all such biosensor tasks autonomously. Elad *et al.* proposed an integrated system with luminescent bacterial reporters for continuous water monitoring [49]. Three parallel microfluidic chips containing 12-wells are loaded with bacterial bioreporters immobilized in agarose, allowing sample replicates and controls on the same chip (Fig. 2D). Sample flow was driven with a peristaltic pump through all wells via a

serpentine channel. Single-photon avalanche diode devices, which are moved above the microfluidic chip with a motorized arm, record bioluminescence emitted by the bioreporter bacteria. The authors applied three different bacterial bioreporter strains that respectively responded to DNA damage, oxidative stress or heavy metals within 2 h exposure. They showed that the system could be operated continuously for 10 days with five consecutive sample measurements, thanks to spontaneous decay of the bioluminescence signal after sample induction down to background level (~2 days) [49].

A different semi-continuous multi-use biosensor disposable cartridge was developed using the aforementioned naturally bioluminescent marine bacterium *Allivibrio fischeri* [35]. This disposable cartridge contained three channels with agarose-encapsulated *A. fischeri* cells that can be exposed to the sample by means of a peristaltic pump. Bioluminescence is continuously monitored during one hour with a CCD camera and any decrease in light emission is a sign for potential toxicants in the sample. After sample exposure, fresh media can be flowed into the device to restore the cells for a subsequent sample analysis [35].

### **Future applications**

Integrated sensors with miniaturized bioreporter assays clearly have potential for monitoring of toxicants in environmental samples, but we see two critical issues that need to be solved which otherwise may strongly limit their deployment. The first is the assay response time and the second is the compound detection limit. Most bioreporters engineered to produce reporter proteins need some 30 min to a few hours before sufficient signal has accumulated in reaction to (low concentrations of) target compounds. This may be sufficient if sample analysis is to be carried out at regular time intervals (e.g., every day) on a remote fixed platform (e.g., a buoy), but is clearly insufficient for autonomous mobile systems (e.g., vehicles, boats) where response times of at most a few minutes would be required.

Current bioreporters that potentially react very rapidly (e.g., decrease in light emission from luciferase) are not very specific nor very sensitive. New approaches are needed here, which

may exploit natural processes directly or enhance those through specific engineering. Such approaches may include rapidly detecting specific enzyme activities (see above [26] [27]), or capturing activity of (eukaryotic) membrane receptor channels that control ion in- and efflux [62]. A further potentially exploitable cellular process is motility, which is fast (seconds), adaptive and reversible (Fig. 1D) [63]. Many microorganisms are motile and can bias the direction of their swimming in response to gradients of chemical compounds, both attractive or repulsive. As an illustration, Zheng *et al.* showed that changes in random motility of two marine microalgae, *Platymonas subcordiformis* and *Platymonas helgolandica* var. *tsingtaoensis*, was suitable to assess toxicity of copper or cadmium in the  $\mu\text{M}$ -range [30].

Another very interesting way to decrease the time response of bioreporters is not to focus on *de novo* induction of reporter gene expression, but to follow subcellular changes in the localization of key proteins in signaling chains, which prelude the actual change in gene expression. The proof of concept of this idea was recently demonstrated in a series of papers on budding yeast quantifying kinase activation and protein synthesis at single cell level from fluorescent protein relocalisation into and out from the nucleus [64, 65]. Relocalisation occurred at a time scale of a few minutes and was reversible upon removal of the target. This principle may be interesting to adapt for environmental monitoring purposes although for now high resolution microscopes and rapid image analysis are required to quantify the signals.

The second crucial issue to solve is the relatively poor detection limit for many live cell bioreporters that are incubated directly (or with marginal dilution) with the sample. As argued above, this may be an accurate reflection of the biology of the cell (hence: compound availability to the cell), but poor detection limits are not very useful for the practice of environmental monitoring. Exceptions exist, which completely fulfill required environmental standards, such as the heavy metal bioreporters for Hg or As that react in the  $\mu\text{g l}^{-1}$  range or below. In particular bioreporter assays for As have been shown to produce accurate results on field samples, comparable to chemical analytics but with the advantage of being carried out on the spot with

almost instant results [46, 47]. In contrast, most other bioreporters respond in the low mg l<sup>-1</sup> range. They can still be used directly on samples in cases of severe pollution as a recent study with bacterial bioreporters on oil spills in the North Sea showed [66], but will be unable to detect low pollutant concentrations without further sample preconcentration. Of note that many of the above-presented miniaturized devices for bioreporter embodiment were made of materials (e.g., PDMS) that are non-inert to organic pollutants. Chemical analytics has recognized and solved this problem by using more resistant materials, by extracting and concentrating target compounds from samples before bringing them on the detectors. So far such methods have not really been adapted to bioreporter assays, mostly because regular extraction solvents (e.g., hexane, dichloromethane) are incompatible with live cells. Extraction techniques also have the advantage of removing potentially negative matrix effects. This may enormously facilitate assay interpretations using bioreporter cells, in particular when toxic compounds other than the target inhibit the performance of the bioreporters. Creative alternative solutions are thus required to be able to purify and concentrate target chemicals before exposure to bioreporter cells, which may help to lower the apparent detection limit.

Undoubtedly, sample pretreatment adds to the complexity of the analysis, which would reduce some of the attractiveness of the heralded simplicity of bioreporter assays. One might therefore have to choose whether or not sample pretreatment is necessary and a yes/no answer by the bioreporter assay on the presence in the sample of a target compound (in comparison to a specified threshold or concentration range) is sufficient, or whether precise quantification of compounds is necessary. In the first case, the bioreporters may be used as simple and cheap first warning systems, followed by advanced broad chemical analysis of samples if required. In particular recurrent contamination cases (e.g., As or Hg contamination) it may be advantageous to develop a more sophisticated miniaturized bioreporter instrument that can conduct quantitative analysis. Both approaches may be useful for environmental monitoring requiring repetitive measurements of samples coming from different localizations in order to characterize the size or the precise position of a contamination but also its evolution through the time.



What will the future of environmental monitoring (with bioreporter assays) look like? Sensors will become more and more miniaturized thanks to microfluidics and micro-printing technologies. The development of autonomous vehicles such as drones, robots, gliders or boats is revolutionizing many areas and would permit screening the environment for potential pollution [67-70]. Bioengineers can profit from this technology revolution by developing accurate biological sensors and by looking for ways to integrate those biosensors in such autonomous vehicles. Robust software will have to be developed to integrate and interpret biosensor results, be it quantitatively or with yes/no answers. How this may look like is illustrated by a study fixing a multi-channel microfluidic chip below a drone to produce an air pollution biosensor [71]. Environmental monitoring may also largely benefit from widely dispersed technologies such as mobile phones. Easy connecting devices may be developed for reading bioluminescence from cell-based assays. For example, a 3D-printed device was developed to measure chemiluminescence as a response from an enzymatic sensor measuring cholesterol and bile acids in oral fluids [72]. Ultimately, everyone may contribute to measuring the quality of his or her "personal environment", which may help to develop detailed pollution maps and better control the contamination in our environment.

## Context of the project

Whole cell bacterial biosensors based on the induction of the expression of a reporter protein are excellent and simple tools for accurate water monitoring of toxicants. The induction process typically requires between 30 min and several hours; the total time needed for *de novo* transcription upon detection of the signal (several minutes [73, 74]), translation (minutes [75]), maturation of proteins (minutes to hours [76]) and accumulation of sufficient reporter protein to provide a signal (hour-scale). For applications requiring detection times in the order of minutes, regular reporter gene expression takes too long. The goal of this project is to search for possibilities that would maintain the flexibility (and sensitivity) of the whole cell bioreporters for a large diversity of potential chemical targets, but which would respond in a second-to-minute rather than an hour-timescale. These types of sensors could be used in diverse field applications, such as integrated into automatized robot platforms.

If we want to achieve this, it is probably necessary to exploit different physiological responses of cells than molecule-dependent *de novo* gene induction. Cellular chemotaxis could possibly achieve this goal. Chemotaxis is a rapid response of bacteria to specific compounds, which is based only on protein-protein interactions and phosphorylations, and has a very defined output (i.e., motility). Chemotaxis is very conserved among motile bacteria, and some strains are even chemotactic toward toxic compounds [77, 78]. These properties make bacterial chemotaxis a suitable pathway to potentially engineer more rapid whole cell biosensors. On the other hand, the readout of chemotaxis is very different than reporter protein activity, and is not necessarily very easy to quantify.

## Bacterial chemotaxis

Chemotaxis is the behavior by motile bacteria to sense their environment and swim in the direction of or away from chemical compounds. Chemotaxis has been intensively studied in *Escherichia coli* during the last decades. *E. coli* motility is characterized by a combination of

straight runs and tumbling, to randomly reorient its swimming direction. In a uniform environment, *E. coli* cells swim randomly with an alternation of “runs” (~ 1 s) and “tumbles” (~0.1 s) in order to explore the maximal accessible volume (Fig. 3A) [79]. In presence of an attractant gradient, cells bias the direction of swimming toward the highest concentration of attractant, with longer runs and fewer periods of tumble (Fig. 3B). The “run” and “tumble” events are determined by the rotation direction of the flagella: when the flagella turn counterclockwise (CCW), all flagella form a bundle and cells swim straight. When the flagella turn clockwise (CW), they destabilize the bundle and the cell starts to tumble [78, 79].

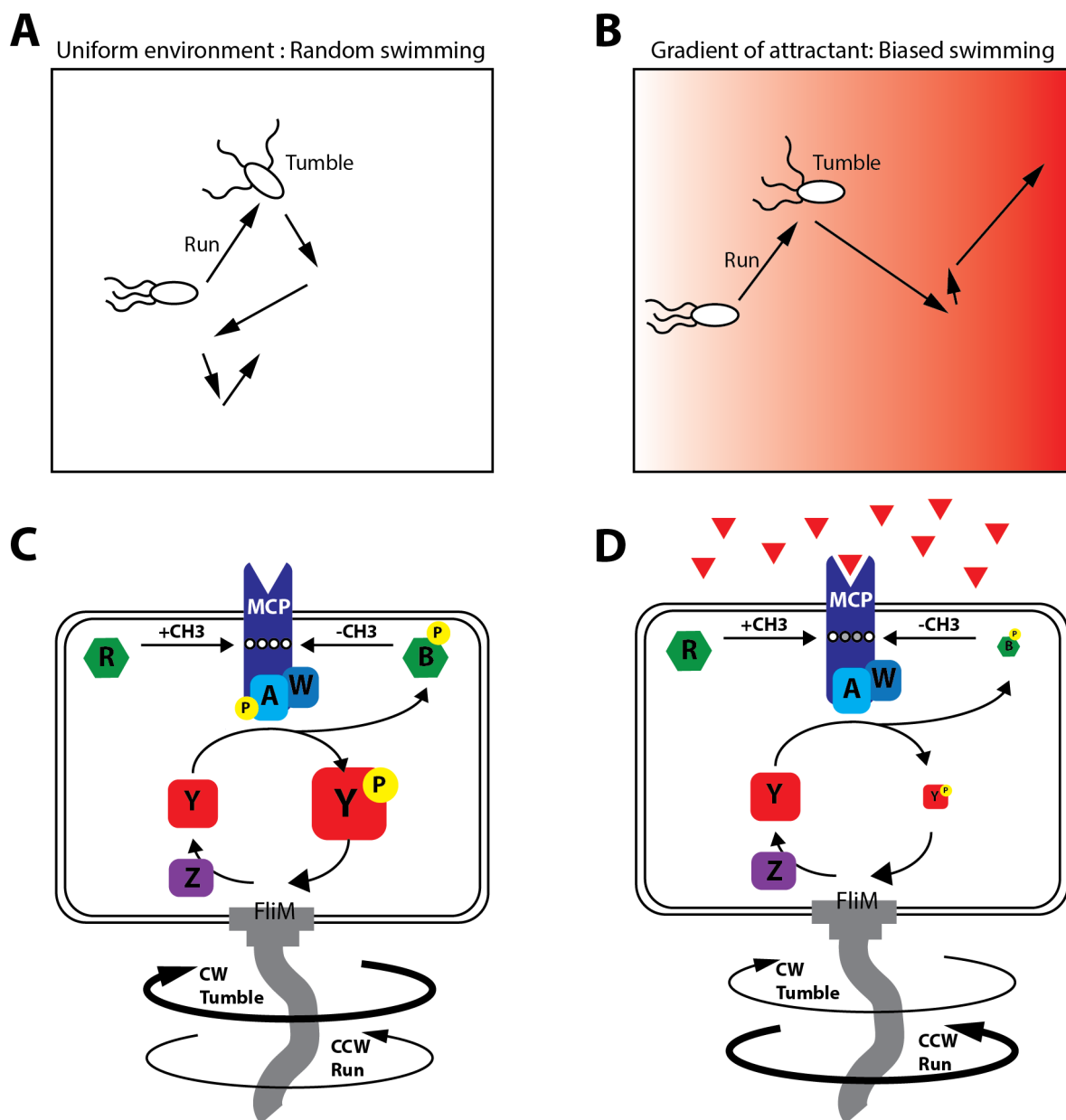


**Figure 3: Bacterial chemotaxis. (A)** Bacterial swimming pattern in a uniform environment, **(B)** bias of swimming pattern in direction of the highest concentration of attractant, **(C-D)** Molecular pathway of chemotaxis from the receptor to the flagellum, in absence of attractant **(C)** and in presence of attractant **(D)**.

At the molecular level, in absence of attractant, the methyl-accepting chemotaxis receptors (MCP) are active, and the associated kinase protein CheA is autophosphorylated and can phosphorylate the response regulator protein CheY. The phosphorylated form of CheY (CheY~P) interacts with the flagellar motor (FliM) and induces CW rotation, leading to more tumbling. At the same time, the phosphatase CheZ constantly dephosphorylates CheY, keeping a basal ratio of “run” and “tumble” events (Fig. 3C). Ligand-binding to the receptor inhibits CheA kinase activity, which decreases the level of CheY~P. A lower CheY~P/CheY ratio on average leads to a decrease of tumble events and more straight runs (Fig. 3D) [78, 79]. On top of the phosphorylation cascade, the chemotaxis system has a “memory”, which allows the cell to temporally compare the level of attractant through chemoreceptor methylation. Methylation of the chemoreceptor at specific amino acids is thought to increase its activity. The methylation state is a result of competition between a methyltransferase named CheR and the methylesterase CheB. Demethylation only occurs from the phosphorylated form CheB~P, whose balance is again maintained by CheA (Fig. 3C-D). This feedback loop allows the cells to swim in direction of the highest concentration of the attractant by the re-establishment of the basal activity level of the receptor through time [80].

*E. coli* possesses five MCP receptors that bind mainly amino acids and sugars. However, methyl-accepting receptors are highly conserved among bacteria, and some are known to mediate chemotaxis toward toxic compounds [77, 78, 81]. Furthermore, it has been shown that functional hybrid receptors can be constructed with the periplasmic binding domain coming from one and the phosphorylation cascade from another receptor, as well as combinations of

chemoreceptors originated from different species [82, 83]. This has been further used to create de novo (reporter) gene expression from chemoreceptor input [84]. One could thus imagine a sort of combinatorial exercise in which the chemoreceptor diversity is exploited to obtain different target specificities, which is somehow coupled to chemotaxis- or phosphorylation-related measurable output [83].

## **Aim of the project and approaches**

The aim of this project is to find new ways to decrease the time-response of whole cell bioreporters, while maintaining target flexibility and sensitivity.

We focus specifically on the chemotaxis pathway because it offers both target flexibility (potentially through different chemoreceptors in a single host or strains with different chemoreceptors) and rapidity (cellular motility). We focus on *E. coli* as a model, because its chemotaxis pathway has been very well characterized and is amenable to genetic manipulation. The project is divided in three different parts.

### *1. Direct quantification of chemotaxis through cellular motility.*

In the first part, we exploited *E. coli* motility directly as a proxy for chemoreceptor-ligand binding. Once cellular motility is robustly quantified, one could imagine that by changing the chemoreceptor or using another bacterial species one could target a different chemical, such as a pollutant. Using microfluidic technology, we attempt to quantify cellular motility in real-time in response to a gradient of the target molecule. The use of micron-scale observation devices decreases the time of the measurement. We have developed microfluidic chips that create a gradient of attractant, toward which the bacteria react. *E. coli* chemotaxis towards standard attractants was quantified at a population level in Chapter 2. Additionally, we studied the response of *Cupriavidus pinatubonensis* towards the herbicide 2,4-dichlorophenoxyacetic acid. Chapter 3 focuses on the design of a different microfluidic chip that would allow a more direct measurement of chemotaxis at the individual cell level.

## *2. The molecular approach.*

In the second part, we manipulated and directly interrogated parts of the chemotaxis pathway as proxies for quantifiable chemoreceptor ligand binding, such as CheY-CheZ interactions using split-Gfp fusions (Chapter 4) and proton flow through the flagellar motor using as reporter a pH-dependent fluorescent protein (Chapter 5)

## *3. Change of attractant specificity of *E. coli**

Finally, in the last part, we investigated the possibilities to change chemoreceptor ligand-specificity of *E. coli* by expressing heterologous methyl-accepting chemoreceptors targeting non-cognate attractants for *E. coli* such as toluene and benzoate (Chapter 6).

## References

1. Bakker K (2012) Water management. Water security: research challenges and opportunities. *Science* 337(6097):914-915.
2. Maxwell SL, Milner-Gulland EJ, Jones JP, Knight AT, Bunnefeld N, Nuno A, Bal P, Earle S, Watson JE, & Rhodes JR (2015) Environmental science. Being smart about SMART environmental targets. *Science* 347(6226):1075-1076.
3. Brinkmann C & Eisentraeger A (2008) Completely automated short-term genotoxicity testing for the assessment of chemicals and characterisation of contaminated soils and waste waters. *Environ Sci Pollut Res Int* 15(3):211-217.
4. Koprowski R, Wrobel Z, Kleszcz A, Wilczynski S, Woznica A, Lozowski B, Pilarczyk M, Karczewski J, & Migula P (2013) Mobile sailing robot for automatic estimation of fish density and monitoring water quality. *Biomed Eng Online* 12:e60.
5. Duarte M, Costa V, Gomes J, Rodrigues T, Silva F, Oliveira SM, & Christensen AL (2016) Evolution of collective behaviors for a real swarm of aquatic surface robots. *PLoS One* 11(3):e0151834.
6. van der Meer JR & Belkin S (2010) Where microbiology meets microengineering: design and applications of reporter bacteria. *Nat Rev Microbiol* 8(7):511-522.
7. Harms H, Wells MC, & van der Meer JR (2006) Whole-cell living biosensors: Are they ready for environmental application? *Appl Microbiol Biotechnol* 70(3):273-280.
8. Spurgeon DJ, Jones OA, Dorne JL, Svendsen C, Swain S, & Sturzenbaum SR (2010) Systems toxicology approaches for understanding the joint effects of environmental chemical mixtures. *Sci Total Environ* 408(18):3725-3734.
9. Daunert S, Barrett G, Feliciano JS, Shetty RS, Shrestha S, & Smith-Spencer W (2000) Genetically engineered whole-cell sensing systems: coupling biological recognition with reporter genes. *Chem Rev* 100(7):2705-2738.

10. Belkin S (2003) Microbial whole-cell sensing systems of environmental pollutants. *Curr Opin Microbiol* 6(3):206-212.
11. Yagi K (2007) Applications of whole-cell bacterial sensors in biotechnology and environmental science. *Appl Microbiol Biotechnol* 73(6):1251-1258.
12. Woutersen M, Belkin S, Brouwer B, van Wezel AP, & Heringa MB (2011) Are luminescent bacteria suitable for online detection and monitoring of toxic compounds in drinking water and its sources? *Anal Bioanal Chem* 400(4):915-929.
13. Park M, Tsai SL, & Chen W (2013) Microbial biosensors: engineered microorganisms as the sensing machinery. *Sensors (Basel)* 13(5):5777-5795.
14. Way JC, Collins JJ, Keasling JD, & Silver PA (2014) Integrating biological redesign: where synthetic biology came from and where it needs to go. *Cell* 157(1):151-161.
15. van der Meer JR (2010) Bacterial sensors: synthetic design and application principles. *Synthesis Lectures on Synthetic Biology* 2(1):1-167
16. Tecon R, Wells M, & van der Meer JR (2006) A new green fluorescent protein-based bacterial biosensor for analysing phenanthrene fluxes. *Environ Microbiol* 8(4):697-708.
17. van der Meer JR, Tropel D, & Jaspers M (2004) Illuminating the detection chain of bacterial bioreporters. *Environ Microbiol* 6(10):1005-1020.
18. Shacham-Diamand Y, Belkin S, Rishpon J, Elad T, Melamed S, Biran A, Yagur-Kroll S, Almog R, Daniel R, Ben-Yoav H, Rabner A, Vernick S, Elman N, & Popovtzer R (2010) Optical and electrical interfacing technologies for living cell bio-chips. *Curr Pharm Biotechnol* 11(4):376-383.
19. Merulla D & van der Meer JR (2016) Regulatable and modifiable background expression control in prokaryotic synthetic circuits by auxiliary repressor binding sites. *ACS Synth Biol* 5(1):36-45.
20. Prindle A, Samayoa P, Razinkov I, Danino T, Tsimring LS, & Hasty J (2011) A sensing array of radically coupled genetic 'biopixels'. *Nature* 481(7379):39-44.



21. Baumann B & van der Meer JR (2007) Analysis of bioavailable arsenic in rice with whole cell living bioreporter bacteria. *J Agric Food Chem* 55(6):2115-2120.
22. Ivask A, Rolova T, & Kahru A (2009) A suite of recombinant luminescent bacterial strains for the quantification of bioavailable heavy metals and toxicity testing. *BMC Biotechnol* 9:41.
23. Garcia-Alonso J, Fakhrullin RF, Paunov VN, Shen Z, Hardege JD, Pamme N, Haswell SJ, & Greenway GM (2011) Microscreening toxicity system based on living magnetic yeast and gradient chips. *Anal Bioanal Chem* 400(4):1009-1013.
24. Bakhrat A, Eltzov E, Finkelstein Y, Marks RS, & Raveh D (2011) UV and arsenate toxicity: a specific and sensitive yeast bioluminescence assay. *Cell Biol Toxicol* 27(3):227-236.
25. Truffer F, Buffi N, Merulla D, Beggah S, van Lintel H, Renaud P, van der Meer JR, & Geiser M (2014) Compact portable biosensor for arsenic detection in aqueous samples with *Escherichia coli* bioreporter cells. *Rev Sci Instrum* 85(1):e015120.
26. Hnaien M, Lagarde F, Bausells J, Errachid A, & Jaffrezic-Renault N (2011) A new bacterial biosensor for trichloroethylene detection based on a three-dimensional carbon nanotubes bioarchitecture. *Anal Bioanal Chem* 400(4):1083-1092.
27. Hnaien M, Bourigua S, Bessueille F, Bausells J, Errachid A, Lagarde F, & Jaffrezic-Renault N (2011) Impedimetric microbial biosensor based on single wall carbon nanotube modified microelectrodes for trichloroethylene detection. *Electrochimica Acta* 56(28):10353-10358.
28. Brennan LM, Widder MW, Lee LE, & van der Schalie WH (2012) Long-term storage and impedance-based water toxicity testing capabilities of fluidic biochips seeded with RTgill-W1 cells. *Toxicol In Vitro* 26(5):736-745.
29. Widder MW, Brennan LM, Hanft EA, Schrock ME, James RR, & van der Schalie WH (2015) Evaluation and refinement of a field-portable drinking water toxicity sensor utilizing electric cell-substrate impedance sensing and a fluidic biochip. *J Appl Toxicol* 35(7):701-708.

30. Zheng G, Wang Y, & Qin J (2012) Microalgal motility measurement microfluidic chip for toxicity assessment of heavy metals. *Anal Bioanal Chem* 404(10):3061-3069.
31. Bazin I, Seo HB, Suehs CM, Ramuz M, De Waard M, & Gu MB (2017) Profiling the biological effects of wastewater samples via bioluminescent bacterial biosensors combined with estrogenic assays. *Environ Sci Pollut Res Int* 24(33-41).
32. Preveral S, Brutesco C, Descamps EC, Escoffier C, Pignol D, Ginet N, & Garcia D (2017) A bioluminescent arsenite biosensor designed for inline water analyzer. *Environ Sci Pollut Res Int* 24(1):25-32.
33. Cayron J, Prudent E, Escoffier C, Gueguen E, Mandrand-Berthelot MA, Pignol D, Garcia D, & Rodrigue A (2017) Pushing the limits of nickel detection to nanomolar range using a set of engineered bioluminescent *Escherichia coli*. *Environ Sci Pollut Res Int* 24(1):4-14.
34. Cardemil CV, Smulski DR, Larossa RA, & Vollmer AC (2010) Bioluminescent *Escherichia coli* strains for the quantitative detection of phosphate and ammonia in coastal and suburban watersheds. *DNA Cell Biol* 29(9):519-531.
35. Jouanneau S, Durand-Thouand MJ, & Thouand G (2016) Design of a toxicity biosensor based on *Aliivibrio fischeri* entrapped in a disposable card. *Environ Sci Pollut Res Int* 23(5):4340-4345.
36. Roda A, Cevenini L, Borg S, Michelini E, Calabretta MM, & Schuler D (2013) Bioengineered bioluminescent magnetotactic bacteria as a powerful tool for chip-based whole-cell biosensors. *Lab on a Chip* 13(24):4881-4889.
37. Ulitzur S, Lahav T, & Ulitzur N (2002) A novel and sensitive test for rapid determination of water toxicity. *Environ Toxicol* 17(3):291-296.
38. Scott DL, Ramanathan S, Shi W, Rosen BP, & Daunert S (1997) Genetically engineered bacteria: electrochemical sensing systems for antimonite and arsenite. *Anal Chem* 69(1):16-20.
39. Cortes-Salazar F, Beggah S, van der Meer JR, & Girault HH (2013) Electrochemical As(III) whole-cell based biochip sensor. *Biosensors & Bioelectronics* 47:237-242.

40. Bitton G & Koopman B (1992) Bacterial and enzymatic bioassays for toxicity testing in the environment. *Rev Environ Contam Toxicol* 125:1-22.
41. Buffi N, Beggah S, Truffer F, Geiser M, van Lintel H, Renaud P, & van der Meer JR (2016) An automated microreactor for semi-continuous biosensor measurements. *Lab Chip* 16(8):1383-1392.
42. Escher BI, Quayle P, Muller R, Schreiber U, & Mueller JF (2006) Passive sampling of herbicides combined with effect analysis in algae using a novel high-throughput phytotoxicity assay (Maxi-Imaging-PAM). *J Environ Monit* 8(4):456-464.
43. Guo Y & Tan J (2013) Applications of delayed fluorescence from photosystem II. *Sensors (Basel)* 13(12):17332-17345.
44. Gu MB, Gil GC, & Kim JH (1999) A two-stage minibioreactor system for continuous toxicity monitoring. *Biosens Bioelectron* 14(4):355-361.
45. Gu MB & Gil GC (2001) A multi-channel continuous toxicity monitoring system using recombinant bioluminescent bacteria for classification of toxicity. *Biosens Bioelectron* 16(9-12):661-666.
46. Siegfried K, Endes C, Bhuiyan AF, Kuppardt A, Mattusch J, van der Meer JR, Chatzinotas A, & Harms H (2012) Field testing of arsenic in groundwater samples of Bangladesh using a test kit based on lyophilized bioreporter bacteria. *Environ Sci Technol* 46(6):3281-3287.
47. Siegfried K, Hahn-Tomer S, Koelsch A, Osterwalder E, Mattusch J, Staerk HJ, Meichtry JM, De Seta GE, Reina FD, Panigatti C, Litter MI, & Harms H (2015) Introducing simple detection of bioavailable arsenic at Rafaela (Santa Fe province, Argentina) using the ARSOLux biosensor. *Int J Environ Res Public Health* 12(5):5465-5482.
48. Tsai HF, Tsai YC, Yagur-Kroll S, Palevsky N, Belkin S, & Cheng JY (2015) Water pollutant monitoring by a whole cell array through lens-free detection on CCD. *Lab Chip* 15(6):1472-1480.

49. Elad T, Almog R, Yagur-Kroll S, Levkov K, Melamed S, Shacham-Diamand Y, & Belkin S (2011) Online monitoring of water toxicity by use of bioluminescent reporter bacterial biochips. *Environ Sci Technol* 45(19):8536-8544.
50. Yagur-Kroll S, Schreuder E, Ingham CJ, Heideman R, Rosen R, & Belkin S (2015) A miniature porous aluminum oxide-based flow-cell for online water quality monitoring using bacterial sensor cells. *Biosensors & Bioelectronics* 64:625-632.
51. Axelrod T, Eltzov E, & Marks RS (2016) Bioluminescent bioreporter pad biosensor for monitoring water toxicity. *Talanta* 149:290-297.
52. Ahn JM, Kim JH, Kim JH, & Gu MB (2010) Randomly distributed arrays of optically coded functional microbeads for toxicity screening and monitoring. *Lab Chip* 10(20):2695-2701.
53. Buffi N, Merulla D, Beutier J, Barbaud F, Beggah S, van Lintel H, Renaud P, & van der Meer JR (2011) Development of a microfluidics biosensor for agarose-bead immobilized *Escherichia coli* bioreporter cells for arsenite detection in aqueous samples. *Lab Chip* 11(14):2369-2377.
54. Buffi N, Merulla D, Beutier J, Barbaud F, Beggah S, van Lintel H, Renaud P, & van der Meer JR (2011) Miniaturized bacterial biosensor system for arsenic detection holds great promise for making integrated measurement device. *Bioeng Bugs* 2(5):296-298.
55. Melamed S, Ceriotti L, Weigel W, Rossi F, Colpo P, & Belkin S (2011) A printed nanolitre-scale bacterial sensor array. *Lab Chip* 11(1):139-146.
56. Date A, Pasini P, & Daunert S (2007) Construction of spores for portable bacterial whole-cell biosensing systems. *Anal Chem* 79(24):9391-9397.
57. Daszczuk A, Dessalegne Y, Drenth I, Hendriks E, Jo E, van Lente T, Oldebesten A, Parrish J, Poljakova W, Purwanto AA, van Raaphorst R, Boonstra M, van Heel A, Herber M, van der Meulen S, Siebring J, Sorg RA, Heinemann M, Kuipers OP, & Veening JW (2014) *Bacillus subtilis* biosensor engineered to assess meat spoilage. *ACS Synth Biol* 3(12):999-1002.

58. Date A, Pasini P, Sangal A, & Daunert S (2010) Packaging sensing cells in spores for long-term preservation of sensors: a tool for biomedical and environmental analysis. *Anal Chem* 82(14):6098-6103.
59. Park J, Wu J, Polymenis M, & Han A (2013) Microchemostat array with small-volume fraction replenishment for steady-state microbial culture. *Lab Chip* 13(21):4217-4224.
60. Denervaud N, Becker J, Delgado-Gonzalo R, Damay P, Rajkumar AS, Unser M, Shore D, Naef F, & Maerkl SJ (2013) A chemostat array enables the spatio-temporal analysis of the yeast proteome. *Proc Natl Acad Sci U S A* 110(39):15842-15847.
61. DeBusschere BD & Kovacs GT (2001) Portable cell-based biosensor system using integrated CMOS cell-cartridges. *Biosens Bioelectron* 16(7-8):543-556.
62. Lim JH, Park J, Hong S, & Park TH (2015) Olfactory receptor screening assay using nanovesicle-immobilized carbon nanotube transistor. *Methods Mol Biol* 1272:189-198.
63. Sourjik V, Vaknin A, Shimizu TS, & Berg HC (2007) *In vivo* measurement by FRET of pathway activity in bacterial chemotaxis. *Methods Enzymol* 423:365-391.
64. Aymoz D, Wosika V, Durandau E, & Pelet S (2016) Real-time quantification of protein expression at the single-cell level via dynamic protein synthesis translocation reporters. *Nat Commun* 7:e11304.
65. Durandau E, Aymoz D, & Pelet S (2015) Dynamic single cell measurements of kinase activity by synthetic kinase activity relocation sensors. *BMC Biol* 13:e55.
66. Brussaard CP, Peperzak L, Beggah S, Wick LY, Wuerz B, Weber J, Samuel Arey J, van der Burg B, Jonas A, Huisman J, & van der Meer JR (2016) Immediate ecotoxicological effects of short-lived oil spills on marine biota. *Nat Commun* 7:e11206.
67. Marjovi A, Arfire A, & Martinoli A (2015) High resolution air pollution maps in urban environments using mobile sensor networks. *2015 International Conference on Distributed Computing in Sensor Systems (DCOSS)*:11-20.

68. Lohmann R & Muir D (2010) Global Aquatic Passive Sampling (AQUA-GAPS): Using Passive Samplers to Monitor POPs in the Waters of the World. *Environmental Science & Technology* 44(3):860-864.
69. Kelly-Gerreyn BA, Hydes DJ, Hartman MC, Siddorn J, Hyder P, & Holt MW (2007) The phosphoric acid leak from the wreck of the MV Ece in the English Channel in 2006: Assessment with a ship of opportunity, an operational ecosystem model and historical data. *Marine Pollution Bulletin* 54(7):850-862.
70. Dong CM, McWilliams JC, Liu Y, & Chen DK (2014) Global heat and salt transports by eddy movement. *Nature Communications* 5:e3294.
71. Lu Y, Macias D, Dean ZS, Kreger NR, & Wong PK (2015) A UAV-mounted whole cell biosensor system for environmental monitoring applications. *IEEE Trans Nanobioscience* 14(8):811-817.
72. Roda A, Guardigli M, Calabria D, Calabretta MM, Cevenini L, & Michelini E (2014) A 3D-printed device for a smartphone-based chemiluminescence biosensor for lactate in oral fluid and sweat. *Analyst* 139(24):6494-6501.
73. Vogel U & Jensen KF (1994) The RNA chain elongation rate in *Escherichia coli* depends on the growth rate. *J Bacteriol* 176(10):2807-2813.
74. Gotta SL, Miller OL, Jr., & French SL (1991) rRNA transcription rate in *Escherichia coli*. *J Bacteriol* 173(20):6647-6649.
75. Proshkin S, Rahmouni AR, Mironov A, & Nudler E (2010) Cooperation between translating ribosomes and RNA polymerase in transcription elongation. *Science* 328(5977):504-508.
76. Iizuka R, Yamagishi-Shirasaki M, & Funatsu T (2011) Kinetic study of *de novo* chromophore maturation of fluorescent proteins. *Anal Biochem* 414(2):173-178.
77. Parales RE & Harwood CS (2002) Bacterial chemotaxis to pollutants and plant-derived aromatic molecules. *Curr Opin Microbiol* 5(3):266-273.

78. Baker MD, Wolanin PM, & Stock JB (2006) Signal transduction in bacterial chemotaxis. *Bioessays* 28(1):9-22.
79. Sourjik V & Wingreen NS (2012) Responding to chemical gradients: bacterial chemotaxis. *Curr Opin Cell Biol* 24(2):262-268.
80. Vladimirov N & Sourjik V (2009) Chemotaxis: how bacteria use memory. *Biol Chem* 390(11):1097-1104.
81. Alexander RP & Zhulin IB (2007) Evolutionary genomics reveals conserved structural determinants of signaling and adaptation in microbial chemoreceptors. *Proc Natl Acad Sci U S A* 104(8):2885-2890.
82. Weerasuriya S, Schneider BM, & Manson MD (1998) Chimeric chemoreceptors in *Escherichia coli*: signaling properties of Tar-Tap and Tap-Tar hybrids. *J Bacteriol* 180(4):914-920.
83. Bi SY, Pollard AM, Yang YL, Jin F, & Sourjik V (2016) Engineering hybrid chemotaxis receptors in bacteria. *Acs Synthetic Biology* 5(9):989-1001.
84. Baumgartner JW, Kim C, Brissette RE, Inouye M, Park C, & Hazelbauer GL (1994) Transmembrane signalling by a hybrid protein: communication from the domain of chemoreceptor Trg that recognizes sugar-binding proteins to the kinase/phosphatase domain of osmosensor EnvZ. *J Bacteriol* 176(4):1157-1163.

## CHAPTER 2

### QUANTITATIVE CHEMICAL SENSING BY BACTERIAL CHEMOTAXIS IN MICROFLUIDIC CHIPS

In an attempt to attain faster readout but maintain flexibility of chemical targeting by bacterial bioreporters, we explored the concept for quantitative chemical sensing by chemotaxis. Cellular motility was quantified from enrichment of cells across a 600  $\mu\text{m}$ -wide chemical gradient stabilized by parallel flow in a microfluidic chip, further supported by transport and chemotaxis modeling. As proof-of-concept, we quantified *Escherichia coli* chemotaxis towards serine, aspartate and methylaspartate as a function of attractant concentration and exposure time. *E. coli* chemotaxis enrichment increased sharply between 0 and 10  $\mu\text{M}$  serine, before saturating at 100  $\mu\text{M}$ . The chemotaxis accumulation rate was maximal at 10  $\mu\text{M}$  serine, leading to observable cell enrichment within 5 min. The potential application for biosensing of environmental toxicants was demonstrated by quantifying chemotaxis of *Cupriavidus pinatubonensis* JMP134 towards the herbicide 2,4-dichlorophenoxyacetate. Our results show that bacterial chemotaxis can be quantified on a scale of minutes and used for developing faster bioreporter assays.



## Introduction

Chemotaxis is the behavior by motile bacteria to sense their environment and swim in the direction of or away from sources of chemicals. Chemotaxis has been intensively studied in *Escherichia coli* [1-4], but various components of the system (e.g., chemoreceptors, flagellar operation) are conserved among motile bacteria [5]. *E. coli* motility is characterized by alternating periods of straight runs and tumbling, during which cells randomly reorient their swimming direction. In a uniform environment, *E. coli* cells swim stochastically with alternating “runs” (~ 1 s) and “tumbles” (~ 0.1 s), in order to explore the maximal accessible space [3]. In presence of an attractant, the cells bias their swimming direction towards the highest concentration of attractant, with longer runs and fewer tumbles [3]. Interestingly, some bacteria show chemotaxis to compounds of environmental interest, which they use as carbon and energy sources [6, 7]. An example of such a bacterium is *Cupriavidus pinatubonensis* (formerly *C. necator* or *Ralstonia eutropha*) JMP134, which is chemotactic towards the herbicide 2,4-dichlorophenoxyacetic acid (2,4-D), that can be metabolized by enzymes encoded on the plasmid pJP4 [8-10].

In this chapter, we attempt to measure chemotaxis via direct cellular motility as a proxy for chemoreceptor-ligand-binding. Chemotaxis has been traditionally studied using different techniques such as swimming plates, capillary assays [11, 12] or agarose plug assays [13], which mostly give a qualitative measurement of the chemotaxis response and take several hours or days for results. On the other hand, microfluidic chips have also been deployed to study and quantify chemotaxis [14-17] and could potentially enable faster and more quantitative cellular readouts. The crucial aspect for inducing cellular chemotaxis in a microfluidic chip is the creation of a micro-scale gradient of the target chemical, which can be formed either by flow or by diffusion [17, 18]. Flow-based gradient generator chips deploy the laminar flow in parallel channels with either attractant or buffer to create a concentration gradient perpendicular to the flow as a consequence of molecular diffusion. This type of chip creates rapid and stable

gradients in which chemotaxis is observed, but the cells undergo a shear stress induced by the flow [19-21]. In the second type of microfluidic chips, the attractant is allowed to diffuse from a source to create a concentration gradient in which cells can react, but the source is separated from the cell compartment by a physical barrier [18, 22-24].

Although chemotaxis has been extensively quantified and modeled, it has rarely been proposed as means for biosensing of target molecules [25]. The main aim of this chapter was thus to test whether chemotactic response from bacterial cells can be reliably quantified and calibrated as a function of attractant concentration. Chemotaxis was quantified in a microfluidic chip similar in concept as in Ref. [18, 22], consisting of three parallel channels, but modified to link the channels by pores so shallow that cells cannot pass (Fig. 1A). Solutions of attractant and buffer are flowing in each of the side channels to create via diffusion a stable gradient across a middle observation channel, where the cells are introduced (Fig. 1B). Cell accumulation on the side of the observation channel closest to the source is recorded and quantified by epifluorescence microscopy. We calibrated the concept by measuring chemotactic response of *E. coli* towards its best known attractants (serine, aspartate and methylaspartate) at different concentrations. Results were compared to numerically modeled steady-state transport of the attractant and biomass in the microfluidic chips. We further used a strain of *Cupriavidus pinatubonensis* JMP134 that was reported to be chemotactic towards 2,4-dichlorophenoxyacetic acid to demonstrate whether chemicals of environmental concern might be detected using a chemotaxis-microfluidic biosensor chip concept.

## Results

### *Fabrication of a stable gradient-forming microfluidic chip*

A polydimethylsiloxane (PDMS) chip was designed in which a stable solute concentration gradient can be established by flowing buffer with and without attractant ("source" and "sink", respectively) in two side-channels (Fig. 1A). The side-channels are connected to the observation channel by series of perpendicular and shallow pores ( $\sim 600$  nm height and  $5 \mu\text{m}$  wide, Fig. 1A, B), allowing attractant diffusion from the source to the sink channel, which creates a gradient perpendicular to the observation channel where cells can be introduced at low flow rate (Fig. 1B). Modeled pressure and flow distribution across the chip in steady-state conditions (see *material and methods*, Fig. 9) shows that the flow in the observation channel is mostly insulated from the side channels, apart from a small inflow through the pores (Fig. 1C, see *streamlines*).

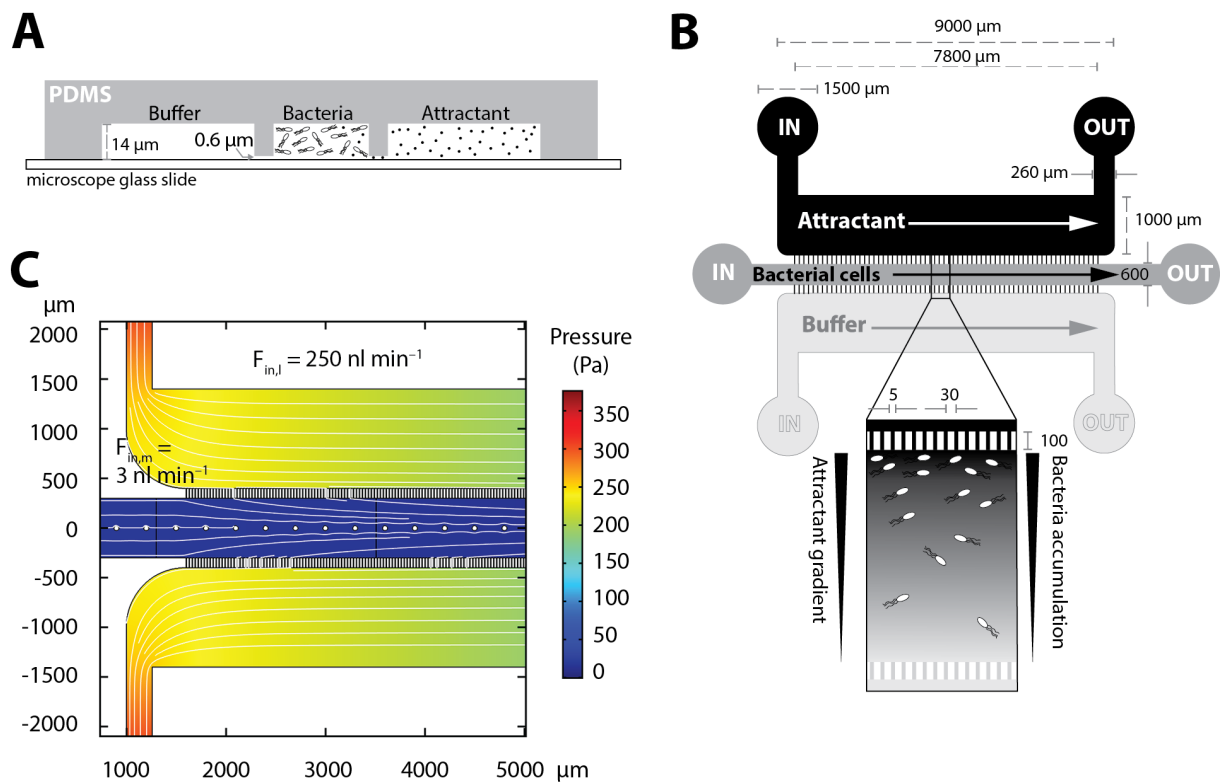


**Figure 1: Concept and design of the chemotaxis microfluidics chip.** (A) Schematic side view of the polydimethylsiloxane (PDMS) chip mounted on a microscope slide. Filter pores ( $0.6 \mu\text{m}$ )

between channels allow chemical diffusion but prevent the passage of bacterial cells. **(B)** Schematic top view of the chip composed of three parallel channels with in- and outlets linked by filters (dimensions in  $\mu\text{m}$ ). Inset illustrates how attractant and buffer flow in the side channels create a gradient perpendicular to the observation channel where the bacteria are introduced. The level of accumulation of cells near the attractant channel is indicative for their chemotaxis response. **(C)** Modeled pressure (color map) and flow distribution (white streamlines) across the chip channels at the used experimental flow settings.

The generation and stability of the chemical gradient was verified by addition of rhodamine B (1 or 10  $\mu\text{M}$ ) to the source buffer and measuring the fluorescence profile across the observation channel near the entry port. The diffusion coefficient of rhodamine in water ( $D = 4.27 \times 10^{-10} \text{ m}^2 \text{ s}^{-1}$  [26]) is in the same order of magnitude as that of small attractant molecules (e.g., serine:  $8.8 \times 10^{-10} \text{ m}^2 \text{ s}^{-1}$  and aspartate:  $8.0 \times 10^{-10} \text{ m}^2 \text{ s}^{-1}$  [27]), and can serve as a proxy for the formation of attractant gradients in the experiments with bacterial cells.

Without flow in the observation channel, rhodamine was detected near the sink channel after 5 minutes and persisted for more than one hour under constant flow ( $0.25 \mu\text{l min}^{-1}$ ) in the side channels (Fig. 2A, B, *red lines*). The introduction of (fluorescently labeled) bacterial cells under slow flow ( $\sim 3 \text{ nl min}^{-1}$ ) in the observation channel slightly changed but did not perturb the stability of the gradient (Fig. 2A, B, *blue lines*). The modeled chemical gradient, based on the steady-state flow and pressure situation as presented in Figure 1C, resembled quite closely the observed rhodamine gradient (Fig. 2C), although we noticed that some rhodamine absorbs to the material of the chip, slightly increasing background fluorescence compared to the model. Notice, however, how the modeled serine concentration at the source border of the observation channel does not completely attain the dosed source concentration in the side flow channel, due to a concentration drop across the filter pores (Fig. 2D).

We concluded that introducing a chemical in the source channel would rapidly (~20 min) lead to the generation of a stable gradient into which the bacterial cells could be introduced with minimal disturbance. We thus expected that the chemotactic cells would react to the chemical gradient by accumulating near the source.

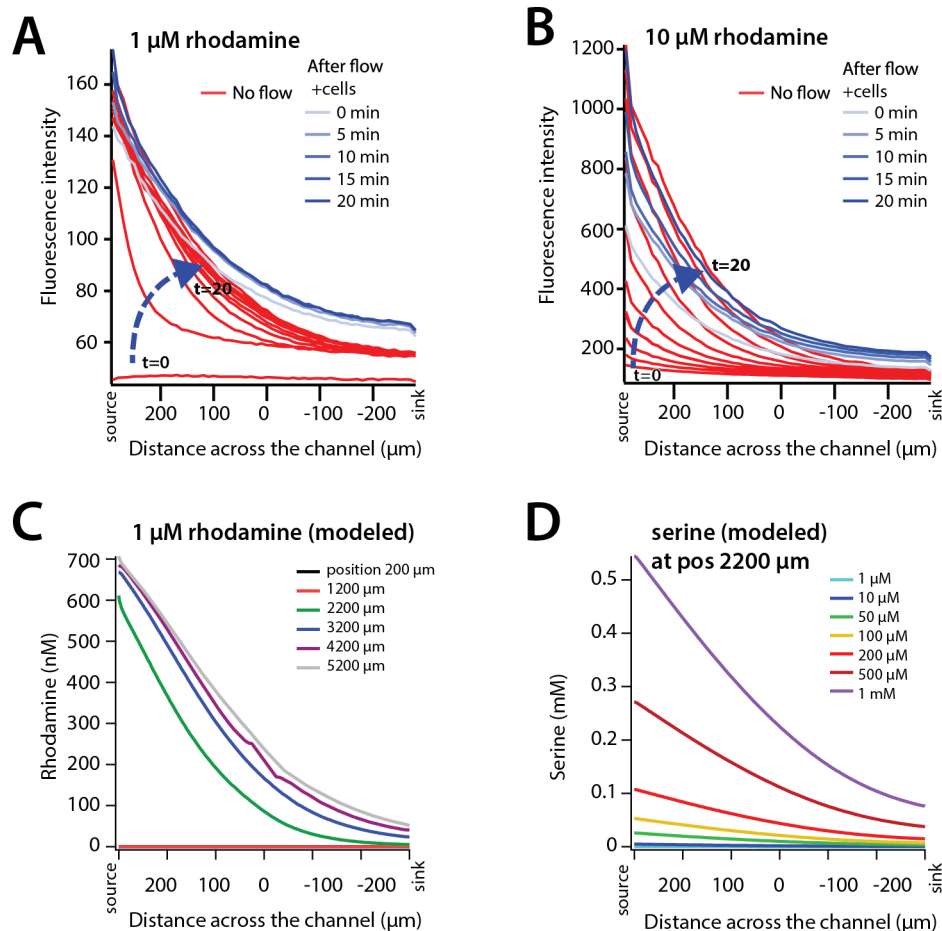


**Figure 2: Gradient formation across the observation (middle) channel of the chip.** Fluorescence profile formation across the channel without flow with **(A)** 1  $\mu\text{M}$  or **(B)** 10  $\mu\text{M}$  rhodamine in the source channel during 20 min (red lines, every 2 min), and after starting *E. coli* cell flow in the observation channel for another 20 min (blue lines, every 5 min). **(C)** Modeled rhodamine steady state gradient across observation channel at different positions along the channel, at the flow conditions computed as in Figure 1C. **(D)** Modeled serine steady-state gradients across the observation cell channel at position 2200  $\mu\text{m}$  for a range of source concentrations, as indicated, at the flow conditions computed as in Figure 1C. Note that for ease

of comparison to the chip design, the distance across the channel is represented from 300 to – 300  $\mu\text{m}$ .

### *Chemotaxis of E. coli MG1655 towards serine*

To calibrate chemotaxis quantitatively as a function of different source concentrations in the developed PDMS chip, we measured the distribution of *E. coli* MG1655 cells tagged with a constitutively expressed enhanced green fluorescent protein (MG1655-*gfp*) across the channel transect and in a 100  $\mu\text{m}$ -wide zone (around position 2200  $\mu\text{m}$  in the chip, see Fig. 1C) at different time points after establishing the serine gradient. A  $\Delta$ *fliC* non-motile mutant of *E. coli* tagged with mcherry ( $\Delta$ *fliC*-*mcherry*) was used as internal control for non-chemotactic cell distribution as a result of the flow inside the observation channel. MG1655-*gfp* and  $\Delta$ *fliC*-*mcherry* cells were added as a mixture to the reservoir of the observation channel of the chip and introduced at low flow (3  $\text{nl min}^{-1}$ ) after serine gradients had established (20 min after starting flow in the side channels). The cell distributions across the observation channel were then recorded during one hour (at 5 min intervals during the first 30 min and then at 10 min intervals until one hour) using epifluorescence microscopy.

As expected, MG1655-*gfp* but not  $\Delta$ *fliC*-*mcherry* cells accumulated near the source channel when serine was added, whereas in absence of serine, MG1655-*gfp* cells distributed homogeneously across the channel (Fig. 3). Both the relative accumulation and the time needed for accumulating MG1655-*gfp* cells depended on the serine concentration (Fig. 3C). The relative cell accumulation was quantified by calculating a *chemotaxis index* (CI), which represents the proportion of fluorescence from cells in the 100  $\mu\text{m}$  zone closest to the source compared to the total fluorescence of cells across a channel transect of 100  $\mu\text{m} \times 600 \mu\text{m}$ . The CI was slightly, but significantly higher for a source with 1  $\mu\text{M}$  serine compared to buffer alone ( $p=9.5 \times 10^{-17}$ , pairwise t-test, one tail, equal variance). In contrast, the CI increased already after 5 minutes at a source concentration of 10  $\mu\text{M}$  (Fig. 3C). Interestingly, the CI increased slower with a 0.1 mM

serine source but was higher after one hour compared to 10  $\mu\text{M}$ , at which point 50% of the MG1655-*gfp* cells had accumulated in the 100  $\mu\text{m}$  segment closest to the source channel. At 1 mM serine in the source, the final CI reached was the same as for 10  $\mu\text{M}$ , but the cells took even longer to accumulate (almost no response before 25 minutes, Fig. 3C).

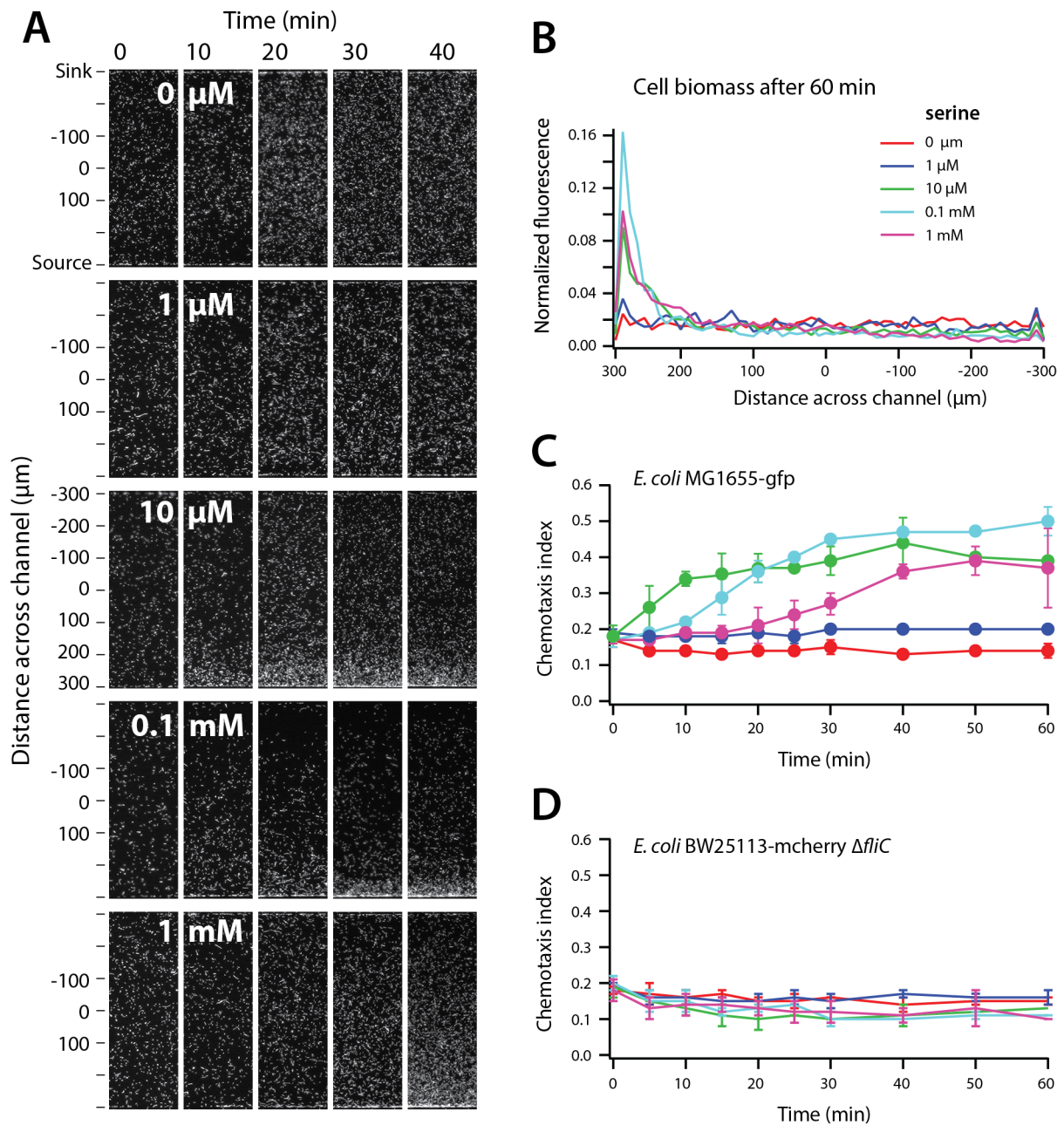


**Figure 3: Quantified chemotaxis of *E. coli* towards different serine concentrations. (A)** Fluorescence images of *E. coli* MG1655-*gfp* accumulating at a transect zone at 2200  $\mu\text{m}$  in the observation channel over time (0–40 min; image *top* corresponds to the sink, *bottom* to the

source channel). **(B)** Cell biomass distribution after 60 min across the channel transect without or at the different source serine concentrations, expressed as normalized fluorescence from *E. coli* MG1655-*gfp* cells. **(C)** Chemotaxis index of MG1655-*gfp*, representing the proportion of cells accumulating in the 100  $\mu\text{m}$  zone closest to the source over time, as a function of serine source concentration. **(D)** Chemotaxis index of  $\Delta\text{fliC}$ -*mcherry*. Error bars are calculated standard deviations from the average of independent triplicate experiments.

Simulation of steady state cell biomass distributions in the observation channel, using the chip geometry and flow conditions, and including both chemotaxis as well as serine metabolism, largely confirmed the observed results (Fig. 4B, C). Cells without modeled chemotactic ability in presence of 10  $\mu\text{M}$  serine in the source channel formed a band of slightly higher biomass concentration in the middle of the channel without any accumulation near the source, similar to the experimentally observed  $\Delta\text{fliC}$  mutant behavior (not shown). This centering in the observation channel is the result of the incoming flow from the side channels (Fig. 1C), pushing non-swimming cells away from the filter pores. In contrast, modeled cells given chemotactic ability accumulated near the source channel, which was dependent on the serine concentration (Fig. 4B, C). One can see that the serine concentration gradient is not the same at every position along the length of the observation channel as a result of the presence of the connecting pores and convective transport along the channel (Fig. 4A). As a consequence, the accumulation of cells also changes along the channel, but is most pronounced near the beginning (Fig. 4B, C). Measured and modeled biomass accumulation in the 100- $\mu\text{m}$  wide zone across a channel transect at 2200  $\mu\text{m}$  from the inlet (as indicated in Fig. 4A), were in close agreement. Cells indeed responded slightly at 1  $\mu\text{M}$  serine in the source channel, with a maximum chemotaxis response between 50 and 200  $\mu\text{M}$  (model) and 100  $\mu\text{M}$  (experiments).



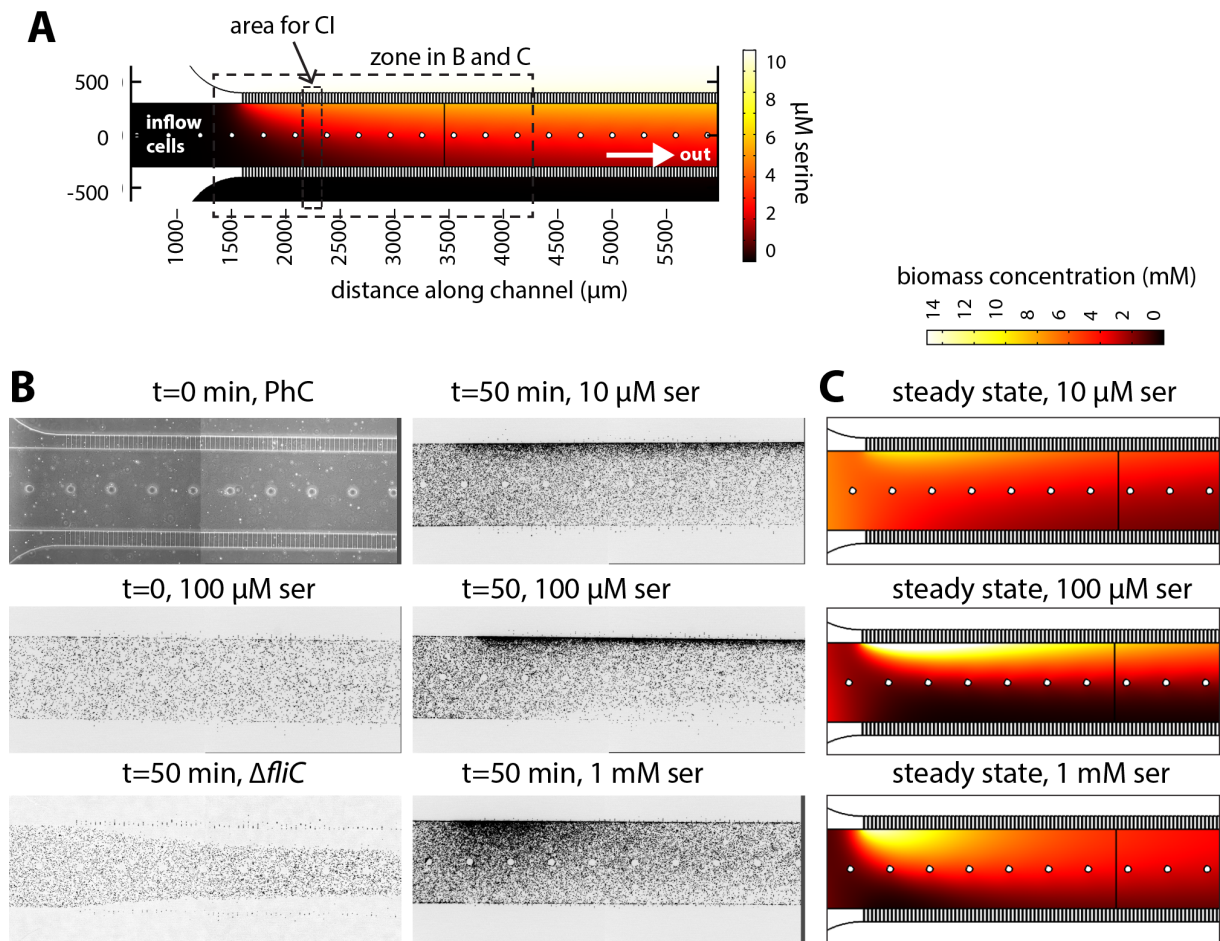


**Figure 4: Modeled *E. coli* chemotaxis towards serine in the microfluidic chip. (A).** Overview of observation channel with steady state serine gradient with a 10  $\mu\text{M}$  source. Note the area used for CI calculation and zone showed in (B) and (C). **(B)** Phase contrast composite image of the observation channel and experimental cell distributions for different conditions. **(C)** Modeled biomass distribution of chemotactic bacteria with increasing concentration of serine in the source. All model parameters listed in Table 1.

### *Comparison of chemotaxis of MG1655 towards aspartate and its non-metabolizable analogue methylaspartate*

Because serine is not only attractant for *E. coli* but can also be metabolized by the cells, its concentration gradient may change over time. In order to test experimentally whether attractant metabolism may have an effect on the chemotactic response time and accumulation of

cells near the source, we compared *E. coli* distributions in the PDMS chip to sources of aspartate (Asp) or its non-metabolizable analogue, N-methyl-D-aspartate (MeAsp) at 1  $\mu$ M, 10  $\mu$ M, 0.1 mM, 1 mM and 10 mM concentrations (Fig. 5).

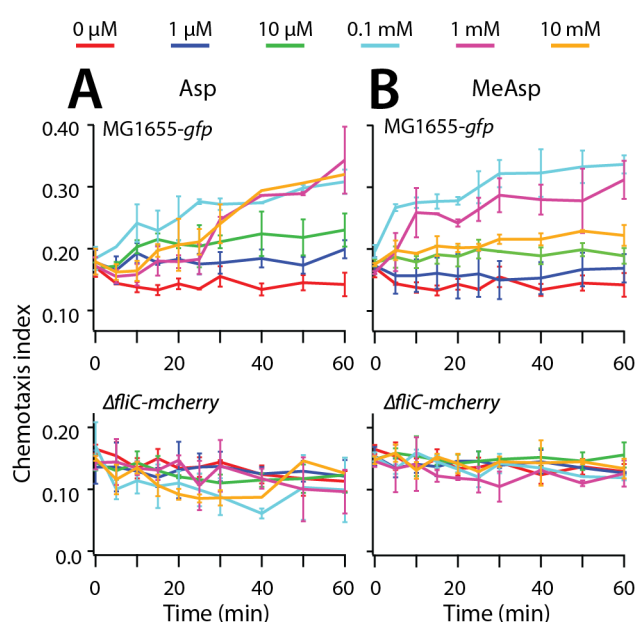


**Figure 5: Quantified chemotaxis of *E. coli* towards aspartate and N-methyl-D-aspartate.** (A) Observed chemotaxis index of MG1655-*gfp* and  $\Delta$ *fliC-mcherry* cells over time in response to aspartate (Asp). (B) As (A) but for the non-metabolizable analogue N-methyl-D-aspartate (MeAsp). Error bars are calculated standard deviations from the average of independent triplicate experiments.

Compared to serine, the CIs of *E. coli* to Asp and MeAsp in general were lower (i.e., less cells accumulating near the source, Fig. 5). *E. coli* MG1655-*gfp* responded slightly to 1  $\mu$ M Asp but more rapidly to 10  $\mu$ M and 0.1 mM, after which the reaction time increased again with 1 and 10 mM (Fig. 5A). The maximum CI increased from 0.19 (at 1  $\mu$ M) to 0.21 (at 10  $\mu$ M) and 0.32 (at 0.1 mM, 1 and 10 mM; Fig. 5A). In contrast, exposure of cells to 1  $\mu$ M MeAsp did not elicit a reaction, whereas the CI at 10  $\mu$ M MeAsp (0.18) was slightly lower ( $p=0.00078$ , pair-wise t-test, time points 30–60 min, one tail, equal variance) than at 10  $\mu$ M Asp (Fig. 5B). At source concentrations of 0.1 and 1 mM, however, the response of the cells to MeAsp was faster than at the equivalent Asp concentration, whereas at 10 mM MeAsp the response dropped to the level of 10  $\mu$ M MeAsp (Fig. 5B).

As expected the  $\Delta fliC$ -*mcherry* mutant of *E. coli* did not react to Asp or MeAsp at any of the tested concentrations (Fig. 5A, B).

This suggests that cells are slightly more sensitive to Asp than to MeAsp, and that attractant metabolism can play a role at higher concentrations (0.1 mM - 10 mM), leading to a delay of chemotaxis response.

### *Chemotaxis response of Cupriavidus pinatubonensis JMP134 towards 2,4-dichlorophenoxyacetic acid*

In order to determine whether chemotaxis can be used as a biosensor readout for pollutants, we tested *C. pinatubonensis* JMP134, which has been shown to be attracted by the herbicide 2,4-D [8]. Similar to *E. coli*, *C. pinatubonensis* JMP134-*gfp* cells accumulated over time near the source inlet in the PDMS chip and as a function of the 2,4-D concentration (Fig. 6A). However, the concentrations of 2,4-D needed to elicit observable JMP134-*gfp* cell accumulation were much higher than in case of *E. coli* for serine, Asp or MeAsp. We also observed that *C. pinatubonensis* JMP134-*gfp* cells became more responsive over time upon storage in the cell reservoir of the microfluidic chip (Fig. 6A, *no* versus *1h adaptation*). In the first exposure, the CI of *C. pinatubonensis* JMP134 increased linearly over time and with increasing concentrations of 1, 5 and 10 mM, being significantly higher after 20 min compared to 0 and 0.1 mM 2,4-D (Fig. 6A, *no adaptation*). In the second exposure, the cells reacted within 5-10 min and the CIs at 1, 5 and 10 mM reached more or less stable values of 0.175, 0.180 and 0.190, respectively (Fig. 6A, *1h adaptation*).

This suggested that chemotactic behavior for 2,4-D of *C. pinatubonensis* is different than that for serine, Asp or MeAsp in *E. coli*.

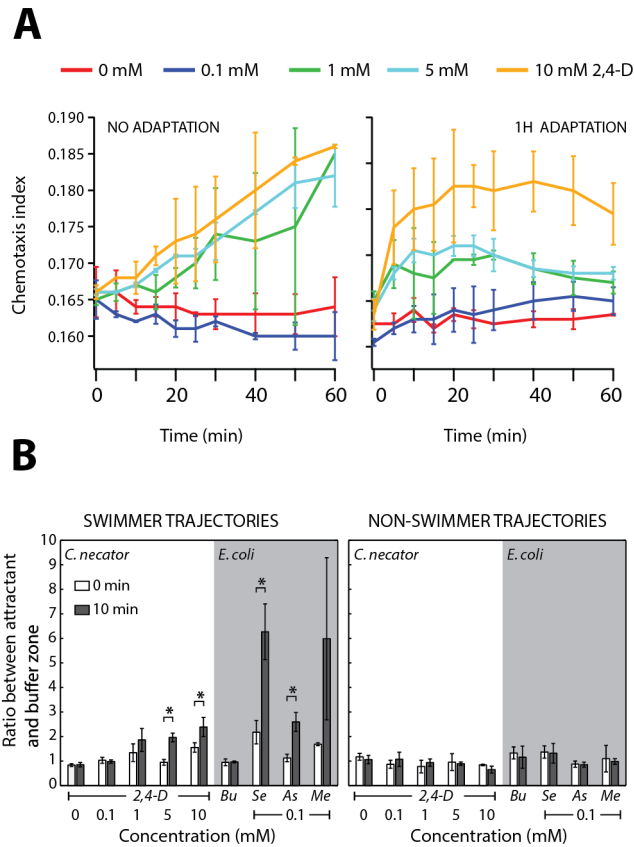


**Figure 6: Quantified chemotaxis of *C.***

***pinatubonensis* to 2,4-D. (A)** Observed chemotaxis index for *C. pinatubonensis* JMP134-*gfp* cells to different 2,4-D concentrations over time, immediately after introduction of cells into the observation channel (*left panel*), or after 1 h storage in the chip reservoir (*right panel*). **(B)**

Swimming behavior deduced from individual cell trajectories immediately after introducing the cells into the observation channel with a pre-established chemical gradient, or after 10 min. *Swimmer*

cells are those with at least a  $10^\circ$  different cell trajectory with the respect to the channel flow (else *non-swimmers*). Bars show the ratio between the numbers of swimmers near the attractant zone versus the sink zone. Bu, buffer only; Se, serine; As, aspartate; Me, Methylaspartate (all three at 0.1 mM). Error bars are calculated standard deviations from the average of three zones of measurement on the movies.

In order to better understand possible chemotactic differences, we analyzed and compared individual *C. pinatubonensis* and *E. coli* cell trajectories calculated from 13 sec movie series in zones near the source and the sink channels immediately after introducing the cells in the observation channels (Fig. 6B, *0 min*) and 10 min afterwards (Fig. 6B, *10 min*). Cells were categorized as "swimmers" if the angle of their average trajectory length deviated more than  $10^\circ$  from the flow direction and if the ratio of the effective travel distance divided by the total trajectory length was smaller than 0.9; else they were considered "non-swimmers". The

proportion of swimmers of *C. pinatubonensis* JMP134-*gfp* increased up to twofold within 10 min in zones close to the attractant compared to the sink, for 1, 5 and 10 mM 2,4-D but not for 0.1 and 0 mM (Fig. 6B, *left panel*). In contrast, the number of non-swimmers was similar in both zones over time (ratio  $\sim 1$ , Fig. 6B, *right panel*). Also *E. coli* showed a sharp increase within 10 min in the number of swimmers close to the source compared to the sink, up to a level of 7-fold for serine and MeAsp, and twofold for Asp (all at 0.1 mM source concentration), whereas the number of non-swimmers remained equal in both zones (Fig. 6B).

This thus suggested that even when *C. pinatubonensis* cells were proportionally swimming as much as those of *E. coli* (ratio = 2 at 10 mM 2,4-D and 0.1 mM Asp, Fig. 6B), they accumulated much less near the source (CI at 10 mM 2,4-D = 0.18, Fig. 6A; versus 0.30 at 0.1 mM Asp for *E. coli*, Fig. 5A).

### *Interpretation of attractant concentration using chemotaxis quantification*

One of the goals of this work was to determine whether chemotaxis quantification could be used to interpret attractant concentration. One could imagine calibrating the chemotaxis response as a function of attractant concentration, which could then be used to interpolate the response to unknown samples (which is similar to the regular practice for biosensor calibrations). One possibility would be to use the maximum CI attained by the cells (Fig. 7A), which increases between 1 and 100  $\mu\text{M}$  and then stabilizes. Calculations of CIs in the microfluidic model under steady state globally follow the same trend, but tend to overestimate the CIs at higher attractant concentrations (Fig. 7A). The modeled chemotaxis index response curves were slightly but not extremely sensitive to variations in two key model chemotaxis parameters, the serine dissociation constant ( $K_C$ , optimum 25-30  $\mu\text{M}$ ) and the chemotactic sensitivity coefficient ( $\text{Chi}_0$ : optimum value  $\sim 8 \times 10^{-4} \text{ cm}^2 \text{ s}^{-1}$ , Fig. 7A). In comparison to the *E. coli* response to serine, Asp or MeAsp, the *C. pinetubonensis* response to 2,4-D was much lower (Fig. 7B). Fitting *C. pinetubonensis* CIs in the microfluidic model required a two orders of magnitude less sensitive cellular chemotaxis coefficient ( $D = 2 \times 10^{-9}$  instead of  $2 \times 10^{-7}$  for *E. coli*,

Table 1). This suggests that the type of chemotaxis by *C. pinetubonensis* JMP134 to 2,4-D is different than that of *E. coli* to serine, Asp or MeAsp. Perhaps *C. pinetubonensis* movement towards 2,4-D is the result of energy taxis rather than chemotaxis with a genuine receptor for 2,4-D, or the result of an intermediate of 2,4-D metabolism being recognized intracellularly [28].

An alternative measure for chemotactic performance could be the cell accumulation rate (CAR), which can be calculated from the observed slopes of CI over time (Fig. 3D). *E. coli* CARs were higher to serine ( $12 \times 10^{-3} \text{ min}^{-1}$ , s.d. =  $4.2 \times 10^{-3}$ ) than to Asp or MeAsp ( $4.9 \times 10^{-3} \text{ min}^{-1}$  and  $6.8 \times 10^{-3} \text{ min}^{-1}$ , resp.), and were reached at lower attractant concentration (serine: 10  $\mu\text{M}$ ; Asp and MeAsp: 0.1 mM). CARs as a function of Asp and MeAsp concentrations were globally very similar (Fig. 7C). The advantage of using a CAR would be that the measurement is faster (e.g., 5 min at 10  $\mu\text{M}$  than the steady-state CI; 30 min or longer).

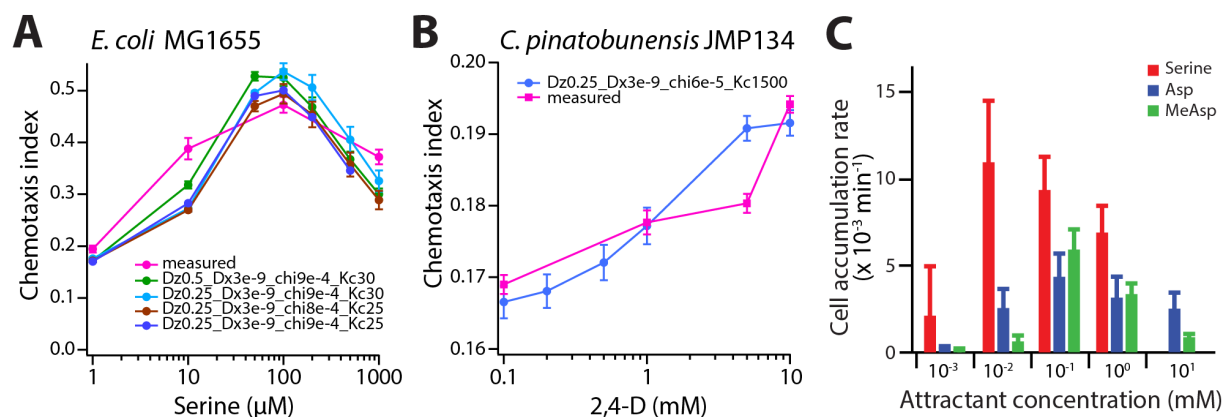


**Figure 7. Concentration dependent chemotaxis responses.** (A) Maximum chemotaxis index (CI) for *E. coli* observed at different serine concentrations in comparison to CIs calculated from the microfluidic model using different parameters coefficients (Chi<sub>0</sub> and K<sub>c</sub>). (B) As (A) but for *C. pinatubonensis* and 2,4-D using one set of chemotaxis parameters (C) Cell accumulation rates for *E. coli* and the three attractants in different concentrations, calculated from the slope of the chemotaxis kinetic profiles as in Fig. 3C.

## Discussion

In this chapter, we quantified bacterial chemotaxis in a microfluidic chip that enabled to produce stable chemical gradients under flow, in order to conceptually assess whether chemotaxis might be used for biosensing of chemical target compounds. The concept of the chip was based on previous demonstrations [18, 22], but altered by including a multitude of small and shallow channels, which allow chemical diffusion from the source to a sink channel, but separate the bacterial cells in an observation channel (Fig. 1). The use of shallow filters prevents passage of the cells into the source channel and abolishes the need for gels or membranes as physical barrier [18, 22], which facilitates the fabrication of the chips. Moreover, the bacterial cells enter the observation channel at low flows, which minimizes shear stress on cells. Although we demonstrate here the proof of concept for the functioning of the chip as a "stand-alone" measurement, one could imagine it operating in continuous mode, with constant fresh bacteria entering the observation zone and sample exchange in the source channel. However with the current experimental settings, sample exchange would be tricky due to the important dead volume upstream the PDMS chip and flow perturbations produced by an exchange of tubing. Implementation of valves inside or outside the PDMS chip could be an approach to achieve this (see chapter 3).

A slight drawback of the filter structures is that they allow a small part of the flow in the side channels to enter the observation channel, which pushes (non-swimming) cells away from the walls (Fig. 1C). Chemotactic and swimming bacteria, however, easily overcome the side-channel inflow and still accumulate near the source channel when attractant is present, although their distribution along the observation channel is not homogenous (Fig. 3).

We used the microfluidic chip to calibrate the kinetics of *E. coli* MG1655 chemotaxis towards serine, aspartate and methylaspartate at different attractant concentrations. The bacteria showed a significant accumulation for concentrations between 1  $\mu\text{M}$  and 1 mM, with the strongest response observed at 0.1 mM and the fastest response at 10  $\mu\text{M}$  serine in the source

channel. The response of the cells to Asp and MeAsp was slightly less sensitive than to serine with observed accumulation between 10  $\mu$ M and 10 mM source concentration (Fig. 3 and Fig. 5). Our results are in agreement with measurements performed by others with *E. coli* RP437 in a different type of microfluidic chip, but without kinetic observations [18]. Comparisons between different microfluidic chip types are rather difficult since most of the times all the channel structures and dimensions are different and the parameters describing the responses vary. Using flow-based microfluidic chips, chemotaxis measurements are usually based on the comparison of the distribution of a motile to a non-motile strain [19-21]. With the diffusion-based microfluidic chips, the quantification can be based on accumulation of bacteria in a specific zone close to the source of attractant (similar to the CI in our work) [23, 24, 29]. Also the abundance of individual cell trajectories extracted from long exposure images or movies of fluorescent bacteria have been used as a parameter to characterize chemotaxis response [18, 21].

Interestingly, both the magnitude and the kinetic response of the cells varied with attractant concentration in the source (Fig. 3C). We speculate that the delay in response at higher attractant concentrations (0.1, 1 and 10 mM) might be due to the cells not immediately detecting the chemical gradient. Attractant metabolism by the cells could change the steepness of the gradient, allowing them to eventually react by further chemotaxis towards the source. By comparing the responses of *E. coli* MG1655 cells towards Asp and its non-metabolizable analogue MeAsp, we showed that at high attractant concentrations, metabolism by the cells can indeed influence their chemotactic response (Fig. 5). The mathematical model was used to simulate the steady-state response of the cells, for which there is little difference in biomass distribution with or without attractant uptake (not shown). Further time-dependent chemotaxis simulations may capture the dynamic response and the kinetics observed in the experiments.

Collectively, our results showed that the microfluidic chip can be used to quantify chemotaxis. For environmental purposes it is not so exciting to use *E. coli* to measure serine concentrations, but we demonstrated with *C. pinetubonensis* that it should be possible to deploy



other strains that naturally swim towards toxic compounds (i.e., 2,4-D, although the response of *C. pinatubonensis* to 2,4-D was not very sensitive). In optimal cases, the chemotactic response in the microfluidic chip was relatively rapid (5-10 min, 10  $\mu$ M serine, Fig. 3C), which is faster than the readout of typical *de novo* gene induction bioreporters (30 min or longer). Instead of measuring the cellular accumulation, one could measure the increase of movement close to the attractant source as a faster readout of the chemotaxis response, but this requires more sophisticated image analysis (Fig. 6B).

We conclude that quantitative detection of chemotaxis response as a function of attractant concentration is feasible and that motility or chemotaxis are promising readouts for faster environmental bioreporters.

## Material and Methods

### *Bacterial strains and growth conditions*

A specific motile strain of *E. coli* MG1655, obtained from the *E. coli* Genetic stock center (Yale) (CGSC#8237), was transformed with plasmid pME6012- $P_{tac}$ -*gfp* (which enables constitutive *gfp* expression from the *tac* promoter). This strain, MG1655-*gfp*, was grown in M9 minimal medium at 37°C with 180 rpm shaking supplemented with 4 g l<sup>-1</sup> of glucose, 1 g l<sup>-1</sup> of Bacto™ casamino acids (BD difco), Hutner's trace metals [30] and 1 mM of MgSO<sub>4</sub> and 25 µg ml<sup>-1</sup> of tetracycline (medium hereafter called M9-Glc-Tc25) [31]. A non-flagellated *E. coli* MG1655  $\Delta$ *fliC* mutant (obtained from the Keio collection [32]) transformed with plasmid pME6012- $P_{tac}$ -*mcherry* was used as a control for the effect of flow in the channel. Strain  $\Delta$ *fliC*-*mcherry* was cultured in M9-Glc-Tc25 and additional kanamycin at 50 µg ml<sup>-1</sup>.

*C. pinatubonensis* JMP134 strains were grown at 30 °C in Nutrient broth no 2 (NB, Oxoid) or 21C minimal medium (MM) [30] supplemented with 3 mM 2,4-D or 10 mM succinate, and further supplemented with 50 µg ml<sup>-1</sup> kanamycin, in case of *gfp* constructs.

All strains used in this chapter are listed in Table 2.

### *C. pinatubonensis* JMP134 tagging with *gfp*

A derivative of *C. pinatubonensis* JMP134 was produced carrying a single chromosomal copy of a  $P_{tac}$ -*gfp* transcriptional fusion delivered by mini-Tn5 transposition. The mini-transposon was delivered into *C. pinatubonensis* JMP134 in a triparental mating [33]. *C. pinatubonensis* transconjugant colonies were checked for green fluorescence and motility and were regrown in MM with 3 mM 2,4-D as sole carbon and energy source. Three individual and independent colonies of *C. pinatubonensis* JMP134-*gfp* (with possible different insertion positions of the mini-Tn5) were then stored at -80 °C. Only one of the clones (strain 5198) was used for the chemotaxis assays but all the clones showed similar chemotaxis response in agarose plug assays.

### *Chip design and fabrication*

A microfluidic chip was designed using CleWin4 software and fabricated in PDMS (polydimethylsiloxane). The chip had three parallel channels linked by shallow pores of 5  $\mu\text{m}$  wide, 100  $\mu\text{m}$  long and 650 nm high (Fig. 1A, B). Buffer (sink) and attractant (source) are flowed in separate side channels, each 1 mm wide and 15  $\mu\text{m}$  high. Constant flow and attractant diffusion through the pores lead to the creation of a gradient perpendicular to the observation channel (600  $\mu\text{m}$  wide and 15  $\mu\text{m}$  high) where the cells are introduced (Fig. 1A, B).

A silicon mold of the designed chip was produced in the cleanroom by standard soft photolithography and etching processes [34]. A first step of photolithography and etching was performed to create an imprint for the pores, because these have a different height. In a second photolithography step, the imprints for the flow channels were created (Fig. 8). The chip was then fabricated as a negative imprint on the silicon mold using PDMS. Syglard 184 silicone elastomer base and curing agent (Dow Corning) were mixed in a 10:1 ratio, degassed under vacuum and poured onto the silicon mold. The polymerization was performed at 80°C overnight. The chips (a block of approximately 2×2 cm) were cut and peeled from the silicon mold, after which flow channel inlets were punched with a 1.5 mm diameter Harris Uni-Core puncher (TED PELLA, Inc). Finally, the PDMS chip was bonded to a standard glass microscopy slide (1 mm thickness, RS France, Milian) using oxygen plasma treatment for 0.1 min (FEMTO plasma cleaner from Diener Electronic, settings: 0.6 mbar, 100 W, Fig. 8)

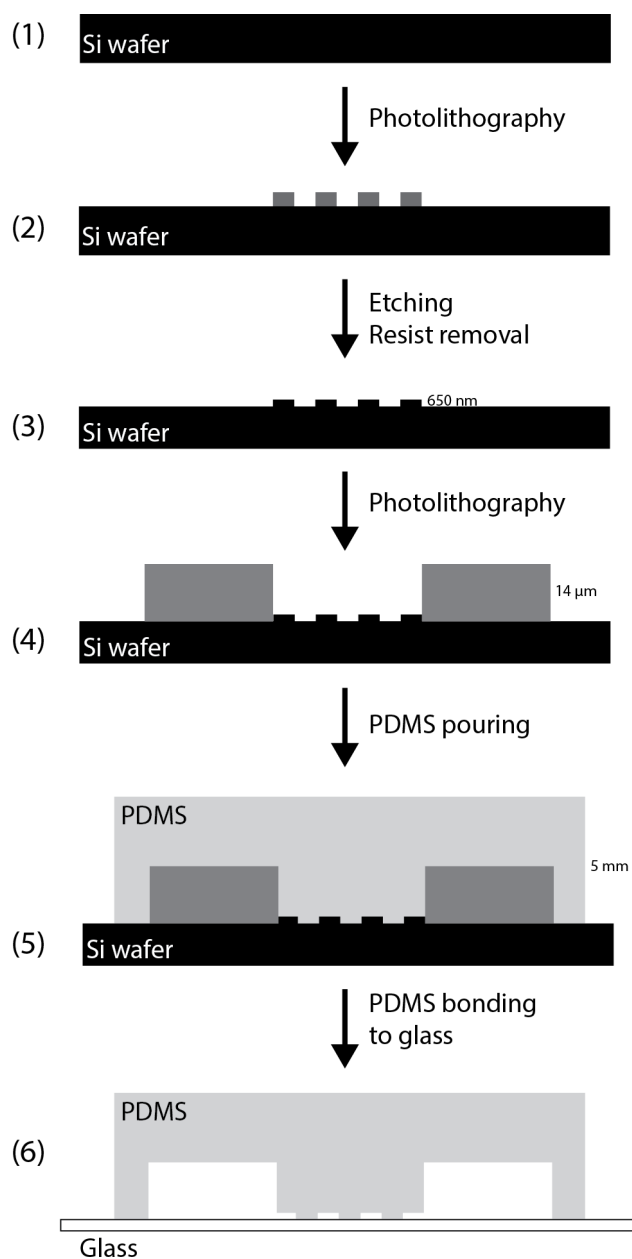


**Figure 8: Microfluidic chip fabrication procedure**

The fabrication procedure starts with a silicon wafer (1). A photolithography process produces a layer of resist at the filter imprint position that protects this zone during the etching step (2). The etching results in the formation of the negative of the 650 nm high channels of the filters (3). A second step of photolithography produces the mold of the channels with a resist layer of 14 microns high (4). This inverted mold is used multiple times to produce the PDMS chips, by pouring PDMS on it and let polymerize (5). Once polymerized, the PDMS is peeled off the inverted mold and, after punching holes for the inlets, is bonded to the glass slide by a plasma treatment (6).

### Gradient formation

Formation of the chemical gradient in the PDMS chip was tested by using 1 or 10 μM of Rhodamine B (Sigma-Aldrich) in water as source and water alone as sink fluid, introduced at a flow rate of 0.25 μl min<sup>-1</sup>. Fluorescence was recorded by epifluorescence microscopy in a 100 μm-wide zone around position 2200 μm of the observation channel (Fig. 4A) every 2 min during 20 min (exposure times 110 ms). After 20 min, an MG1655-*gfp* cell suspension (~10<sup>8</sup> cells ml<sup>-1</sup>) was connected at a flow rate of 3 nl min<sup>-1</sup>. Rhodamine fluorescence was again recorded

immediately, 5, 10, 15 and 20 min after connecting the cell suspension (exposure times 200 ms). Fluorescence was recorded using a DFC 350 FX R2 Leica camera mounted on an inverted DMI 4000 Leica microscope using a N PLAN 10X objective. Fluorescence profiles were calculated from digital images using the ImageJ open source software (<http://imagej.nih.gov/ij/>).

### *Preparation of cells for chemotaxis assays*

Overnight cultures of MG1655-*gfp* and  $\Delta$ *fliC-mcherry* in M9-Glc with appropriate antibiotics were diluted 100-fold in the same medium and grown 3 hours until reaching a culture turbidity at 600 nm ( $OD_{600}$ ) of 0.5. After checking the motility of the cells under phase-contrast microscopy, 1 ml of each culture was centrifuged at 2,400 *g* for 5 min, after which the supernatant was decanted and the cell pellet resuspended in 1 ml of motility buffer (motility buffer is 10 mM potassium phosphate, 0.1 mM EDTA, 10 mM lactate, 1  $\mu$ M methionine, pH 7.0) [35]. Centrifugation and resuspension were repeated twice, after which both MG1655-*gfp* and  $\Delta$ *fliC-mcherry* pellets were, respectively, resuspended in 250  $\mu$ l and 500  $\mu$ l of motility buffer. Both cell suspensions were mixed at a 1:1 ratio (250  $\mu$ l : 250  $\mu$ l) for introduction into the microfluidic chip. Cultures suspended in motility buffer were used for chemotaxis experiments within 1 h. For chemotaxis assays with *C. pinatubonensis* JMP134-*gfp*, an overnight culture grown on MM with 10 mM succinate plus 0.5 mM 2,4-D and 50  $\mu$ g ml<sup>-1</sup> kanamycin was diluted 16-fold in MM with 5 mM succinate and 0.1 mM 2,4-D. The culture was incubated at 30 °C until its turbidity reached an  $OD_{600}$  between 0.5-0.6. This cell suspension was then directly used for the chemotaxis assay in order to preserve maximal cellular motility (centrifugation or filtering caused too much loss of swimming cells).

### *On-chip chemotaxis assays*

Two Hamilton 2.5 ml glass syringes (model 1002 RN with an RN(22/51/3) large needle, Hamilton) were connected to ~40 cm long tygon tubings (internal  $\varnothing$  0.51 mm, wall 0.91 mm, Tygon ST, Ismatec) and a custom-made metal adapter (length ~5 cm, bend to 90°, made from

steel capillary internal  $\varnothing$  0.25 mm, external  $\varnothing$  1/16 inches, Metrohm, Switzerland). One syringe was filled with motility buffer containing attractant (e.g., 10  $\mu$ M serine), whereas the other was filled with motility buffer (for *E. coli*). In case of chemotaxis assays with *C. pinatubonensis* we used MM instead of motility buffer. A 100  $\mu$ l Hamilton glass syringe (model 1710 RN with a RN22/51/3 small needle, Hamilton) connected to 40 cm tygon tubing was filled with the cell suspension. The metal adapters with connected tubing and syringes were gently pushed into the inlets of the side channels on the PDMS chip, the syringes were mounted on a double syringe pump (NE-4000, NewEra, Pump System Inc.), and flow was started at 0.25  $\mu$ l min<sup>-1</sup>. After 20 min, 7  $\mu$ l of cell suspension was pipetted in the inlet of the middle (observation) channel and the metal adapter for the tubing and 100  $\mu$ l syringe with the further cell suspension was gently inserted to minimize flow disturbance. The flow in the side channels was maintained at 0.25  $\mu$ l min<sup>-1</sup>, whereas the observation channel was operated at 3 nl min<sup>-1</sup> using a separate syringe pump (NE-1000, NewEra, Pump System Inc.). The glass slide with PDMS chip was mounted on an inverted Leica DMI 4000 microscope, and focus was maintained on the first millimeter of the observation cell channel (between positions 1500-2500  $\mu$ m in Fig. 4A) using an N PLAN 10X objective. Phase-contrast (10 ms) and fluorescence (gfp, 110 ms and mcherry, 200 ms) was digitally imaged every 5–10 min during one hour using a black-and-white DFC 350 FX R2 camera (Leica). A select number of experiments was complemented by video series of images taken every 5–10 min during 13 sec in order to record cell trajectories. Images were exported as 16-bit TIF and analyzed for (fluorescence) intensity in both channels using ImageJ. A zone of 100 $\times$ 600 pixels ( $\sim$ 101 $\times$ 610  $\mu$ m) was drawn at a distance of 400 microns from the beginning of the filter (approximately the transect at 2200  $\mu$ m in Figure 4A). Fluorescence profiles were extracted using ImageJ by averaging the grey values across a 100-pixels-width segment spanning the complete channel transect (600  $\mu$ m,  $\sim$ 600 pixels). Grey values of ten 100 pixel-lines were then again averaged (obtaining 60 values, each of a 100 $\times$ 10-pixel zone). The fluorescence values were finally normalized by the total fluorescence in the zone. For the CI (chemotaxis index) the ratio of fluorescence was calculated between the 100 pixels ( $\sim$ 100

microns) segment closest to the source compared to the total transect fluorescence. The CAR (cell accumulation rate) was then quantified as the slope of CI over time (from at least three time points).

Individual cell trajectories were extracted from three zones of cropped 200×200 pixels near the sink and the source channels, by using the *mosaic 2D* tracking plugin in ImageJ [36]. Coordinates of the trajectories were exported to MATLAB (version R2015\_b, MathWorks, Inc.) for further analysis. Total trajectory lengths, effective travel distances (start to end coordinates) and average trajectory angles compared to flow ( $0^\circ$ ) were calculated for each individual cell. The distributions of those three parameters were then used to separate cells into “swimmer” and “non-swimmer” categories, with non-swimmers characterized by a ratio of trajectory length divided by effective travel distance of 1 ( $\pm 10\%$ ) and a trajectory angle of  $0^\circ \pm 10^\circ$ . Next, the ratios of swimmers to non-swimmers were calculated per attractant and buffer (sink) zone, averaged across three pixel areas per zone and statistically compared with a Welch two sample t-test.

### *Steady-state model description*

This model was developed by Jan Roelof van der Meer and Cristian Picioreanu (Delft University of Technology, The Netherlands) and the simulations were performed by Jan Roelof van der Meer.

**Geometry.** The microfluidic device had three parallel channels (domains  $\Omega_1$ , source;  $\Omega_2$ , sink and  $\Omega_3$ , cells), connected by two filter zones (domains  $\Omega_4$  and  $\Omega_5$ ) (Fig. 9A). For a reasonable balance between computational burden and model accuracy, we chose to represent the device in a two-dimensional space (i.e., *top-view*). However, a shallow-channel approximation was implemented to correct for the large friction forces induced by the parallel walls on the fluid flow. All the geometry dimensions and physical model parameters are listed in Table 1.

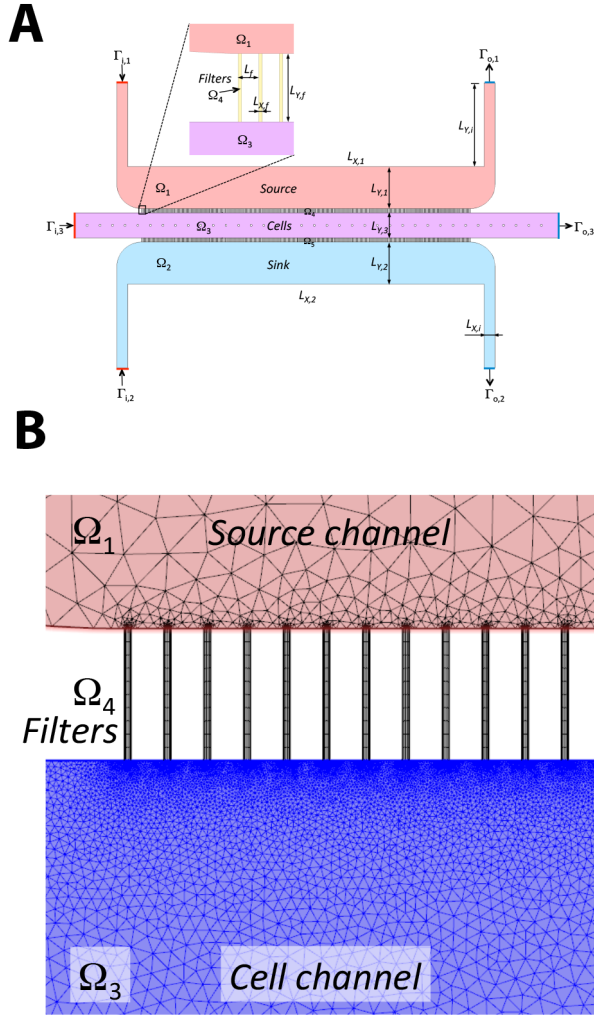


**Figure 9: Model description (A)** Model geometry, dimensions, domains and boundaries.  $\Omega_1$ : Source domain (fed with chemoattractant solution),  $\Omega_2$ : Sink domain (fed with water),  $\Omega_3$ : Cells domain (fed with a suspension of cells),  $\Omega_4$  and  $\Omega_5$ : Filter domains (separate the cells from source and sink channels).  $\Gamma_{i,1}$ ,  $\Gamma_{i,2}$ ,  $\Gamma_{i,3}$ : Inflows,  $\Gamma_{o,1}$ ,  $\Gamma_{o,2}$ ,  $\Gamma_{o,3}$ : Outflows. The geometry dimensions are listed in Table 1. **(B)** Finite element mesh detail in the neighborhood of the filter region.

**Fluid flow.** A correct representation of fluid flow (hydrodynamics) through the microfluidic device is essential for the further description of solute (attractant) transport and microbial chemotaxis. Due to the very low Reynolds number ( $Re < 0.02$ ), the inertial term in the momentum balance was neglected. The creeping flow is therefore described by the Stokes equations for stationary, laminar and incompressible flow [37]:

$$\nabla p = \mu \nabla^2 \mathbf{u} + \mathbf{F}_w \quad (0)$$

$$\nabla \cdot \mathbf{u} = 0 \quad (0)$$

where the variables are  $p$  (liquid pressure) and  $\mathbf{u}$  (velocity vector), with a constant dynamic viscosity  $\mu$  of water at 20 °C. In microfluidic devices, the hydraulic resistance induced by the top and bottom parallel walls of the flow channels is very important, leading to a large contribution



in the pressure drop. To correct the two-dimensional momentum balance for this shallow-channel effect, an additional body force was introduced in equation (0),

$$\mathbf{F}_w = -12\mu\mathbf{u}/h^2 \quad (3)$$

where  $h$  is the channel height: 14  $\mu\text{m}$  for the main flow channels ( $\Omega_1$ ,  $\Omega_2$  and  $\Omega_3$ ) and 0.25  $\mu\text{m}$  for the filters ( $\Omega_4$  and  $\Omega_5$ ).

The source and sink channel inlets  $\Gamma_{i,1}$  and  $\Gamma_{i,2}$  were defined as laminar flows with the same mass flow rate  $F_{in,l}$ . Another laminar flow with flow rate  $F_{in,m}$  was set at the observation channel inlet  $\Gamma_{i,3}$ . The outflows  $\Gamma_{o,1}$ ,  $\Gamma_{o,2}$  and  $\Gamma_{o,3}$  were all assigned a zero gauge pressure, being open to the air. All the other external boundaries were no-slip walls ( $\mathbf{u}=0$ ), while flow continuity existed between all flow domains.

**Solute transport.** The spatial distribution of chemoattractant (serine) or fluorescent tracer molecule (rhodamine B) concentrations  $c_S$  in all domains resulted from the material balances including convection and diffusion terms:

$$\nabla \cdot (-D_S \nabla c_S + \mathbf{u} c_S) = 0 \quad (4)$$

where  $D_S$  is a constant diffusion coefficient of the solute. If the chemoattractant substance was taken up by the microbial cells, an additional reaction term  $R_S$  entered the solute balance (4) only on the domain  $\Omega_3$  (in the other domains  $R_S = 0$ ):

$$\nabla \cdot (-D_S \nabla c_S + \mathbf{u} c_S) = R_S \quad (5)$$

The chemoattractant reaction kinetics was described by a saturation rate expression,

$$R_S = -v_{max} c_X c_S / (K_m + c_S) \quad (6)$$

with  $v_{max}$  the maximum specific uptake rate,  $K_m$  the Michelis-Menten coefficient and  $c_X$  the local concentration of cells.

In the source channel inflow  $\Gamma_{i,1}$  a constant concentration  $c_S = c_{S,i}$  was applied, while in the other two inflows  $\Gamma_{i,2}$  and  $\Gamma_{i,3}$  there was no solute ( $c_S = 0$ ). All outflows  $\Gamma_{o,1}$ ,  $\Gamma_{o,2}$  and  $\Gamma_{o,3}$  were purely convective (no-diffusion boundary type). All the other external boundaries were insulated (no-flux conditions), while solute flux continuity was assumed between all domains (e.g., Fig. 1C).

**Cell transport.** The spatial distribution of microbial cells in domain  $\Omega_3$  was represented by a concentration  $c_X$ . The concentration of cells results from a material balance with an additional chemotactic term besides the convection and isotropic motility, according to the Alt's cell balance modifications of the the Patlak-Keller-Segel model of chemotaxis [38, 39]:

$$\nabla \cdot (-D_X \nabla c_X + D_{ch} c_X \nabla c_S + \mathbf{u} c_X) = 0 \quad (7)$$

$D_X$  is a constant motility coefficient for the cells swimming against the gradient of cell concentration  $\nabla c_X$  (similar to isotropic molecular diffusion). The chemotactic sensitivity function models the oriented motility of cells along the gradient of substrate  $\nabla c_S$ , proportional with a chemotactic coefficient  $D_{ch}$  and the local concentration of cells  $c_X$ . The chemotactic coefficient is then dependent on [39]:

$$D_{ch} = \frac{\chi_0}{\nu} \frac{K_C}{(K_C + c_S)^2} \quad (8)$$

with  $\chi_0$  the chemotactic sensitivity coefficient (typical values for *E. coli*  $10^{-5}$ – $10^{-4}$   $\text{cm}^2 \text{s}^{-1}$ , [39]),  $\nu$  is a scaling factor (value = 3), and  $K_C$  is the receptor-ligand dissociation constant (typical value for Tsr and serine = 30  $\mu\text{M}$  [18]). We included an upper limit for the chemotactic coefficient, motivated by a maximum reachable density of cells  $c_{X,max}$  so that  $D_{ch} = D_{ch,0}(1 - c_X/c_{X,max})$ .

A constant concentration  $c_X = c_{X,i}$  was fed through inflow  $\Gamma_{i,3}$ . The outflow  $\Gamma_{o,3}$  was purely convective, thus the normal components of the diffusion and chemotaxis fluxes were both set to zero. All the other boundaries of domain  $\Omega_3$  (walls and filter/channel edges) were insulated so that the total flux of cells through these was zero.

**Model solution.** The steady state model equations were solved by a finite element method, implemented in COMSOL Multiphysics (v5.2, COMSOL Inc., Burlington, MA). To improve the numerical convergence, the equations were solved in a sequential approach, first fluid flow, then solute transport and finally the cell transport. In the case of chemoattractant uptake, the equations for solute and cell transport with chemotaxis and reaction were solved simultaneously. A triangular finite element mesh of max. size 50  $\mu\text{m}$  was created for domains  $\Omega_1$ ,

$\Omega_2$  and  $\Omega_3$ , while a rectangular mesh with elements of  $1 \mu\text{m}$  by  $10 \mu\text{m}$  was used for each filter region  $\Omega_4$  and  $\Omega_5$ . In the cell channel near first filters the mesh was refined to max.  $20 \mu\text{m}$  and min.  $1 \mu\text{m}$  sizes in order to capture the very strong cell concentration gradients (Fig. 9B).

**Table 1: Model parameters**

Description	Symbol	Value	Units	Source
<i>Geometry</i>				
Height (z-direction)				
- channel	$h$	14	$\mu\text{m}$	experimental
- filter		0.25	$\mu\text{m}$	
Cell channel				
- width	$L_{Y,3}$	0.6	mm	experimental
- length	$L_{X,3}$	11.5	mm	
Source and sink channels				experimental
- width	$L_{Y,1}, L_{Y,2}$	1	mm	
- length	$L_{X,1}, L_{X,2}$	9	mm	
Inlet/outlet channels				experimental
- width	$L_{X,i}$	0.26	mm	
- length	$L_{Y,i}$	2	mm	
Filters				experimental
- width	$L_{X,f}$	5	$\mu\text{m}$	
- length	$L_{Y,f}$	100	$\mu\text{m}$	
Filter spacing	$L_f$	30	$\mu\text{m}$	experimental
<i>Flow</i>				
Water viscosity (at $20^\circ\text{C}$ )	$\mu$	0.001	Pa s	-
Water density	$\rho$	1000	$\text{kg m}^{-3}$	-
Flow rate source/sink channels inlet	$F_{in,l}$	0.25	$\mu\text{L min}^{-1}$	experimental

Flow rate cell channel inlet	$F_{in,m}$	0.003	$\mu\text{L min}^{-1}$	experimental
------------------------------	------------	-------	------------------------	--------------

*Solutes*

Diffusion coefficient<sup>a</sup>

- rhodamine B	$D_S$	$3.6 \times 10^{-10}$	$\text{m}^2 \text{s}^{-1}$	[26, 40]
---------------	-------	-----------------------	----------------------------	----------

- serine		$8.9 \times 10^{-10}$		
----------	--	-----------------------	--	--

Serine concentration in inflow	$c_{S,i}$	1, 5, 10, 20	$\mu\text{mol L}^{-1}$	experimental
--------------------------------	-----------	--------------	------------------------	--------------

Maximum serine uptake rate	$v_{max}$	338	$\text{nmol mmol}^{-1} \text{min}^{-1}$	[41]
----------------------------	-----------	-----	---	------

Michaelis-Menten half-saturation coefficient	$K_m$	6	$\mu\text{mol L}^{-1}$	[41]
--	-------	---	------------------------	------

*Cells*

Motility coefficient	$D_X$	$1 \times 10^{-11}$	$\text{m}^2 \text{s}^{-1}$	estimated
----------------------	-------	---------------------	----------------------------	-----------

Maximum chemotaxis coefficient	$D_{ch,0}$	$2 \times 10^{-7}$	$\text{m}^5 \text{s}^{-1} \text{mol}^{-1}$	estimated
--------------------------------	------------	--------------------	--	-----------

Cell concentration in inflow	$c_X$	10	$\text{mmol L}^{-1}$	experimental
------------------------------	-------	----	----------------------	--------------

Maximum cell density	$c_{X,max}$	$10 \times c_X$	$\text{mmol L}^{-1}$	estimated
----------------------	-------------	-----------------	----------------------	-----------

---

a) corrected for 20 °C

**Table 2: Bacterial strains used in this study**

<b>Strain</b>	<b>Plasmid</b>	<b>Strain collection n°</b>	<b>Source or reference</b>
<i>Escherichia coli</i> MG1655 (motile)		4498	<i>E. coli</i> Genetic stock center (Yale) (CGSC#8237)
<i>Escherichia coli</i> MG1655	pME6012-P <sub>tac</sub> -gfp	4513	This study
<i>Escherichia coli</i> BW25113 $\Delta$ <i>flhC769::kan</i> (Keio collection)	pME6012-P <sub>tac</sub> -mcherry	4530	This study
<i>Escherichia coli</i> cc118 $\lambda$ pir	pCK218-P <sub>tac</sub> -gfp	2739	[42]
<i>Escherichia coli</i> HB101	pRK2013	2	[33]
<i>Cupriavidus pinatubonensis</i> JMP134	pJP4	28	[43]
<i>Cupriavidus pinatubonensis</i> JMP134 (mini-Tn5-P <sub>tac</sub> -gfp)	pJP4	5198	This study

## **Acknowledgements**

I want to thank Jan Roelof van der Meer who developed the model and made all the simulations, Cristian Picioreanu for his help in the modeling development and Harald van Lintel for his advices concerning the microfluidic chip design. I also want to thank the staff of the Center of MicroNanoTechnology (CMI) in Ecole Polytechnique Fédérale Lausanne (EPFL) who taught me how to produce the silicon molts and PDMS chips in the cleanroom.

## References

1. Hazelbauer GL (2012) Bacterial chemotaxis: the early years of molecular studies. *Annu Rev Microbiol* 66:285-303.
2. Baker MD, Wolanin PM, & Stock JB (2006) Signal transduction in bacterial chemotaxis. *Bioessays* 28(1):9-22.
3. Sourjik V & Wingreen NS (2012) Responding to chemical gradients: bacterial chemotaxis. *Curr Opin Cell Biol* 24(2):262-268.
4. Tindall MJ, Gaffney EA, Maini PK, & Armitage JP (2012) Theoretical insights into bacterial chemotaxis. *Wiley Interdiscip Rev Syst Biol Med* 4(3):247-259.
5. Porter SL, Wadhams GH, & Armitage JP (2011) Signal processing in complex chemotaxis pathways. *Nat Rev Microbiol* 9(3):153-165.
6. Parales RE & Harwood CS (2002) Bacterial chemotaxis to pollutants and plant-derived aromatic molecules. *Curr Opin Microbiol* 5(3):266-273.
7. Parales RE, Luu RA, Hughes JG, & Ditty JL (2015) Bacterial chemotaxis to xenobiotic chemicals and naturally-occurring analogs. *Curr Opin Biotechnol* 33:318-326.
8. Hawkins AC & Harwood CS (2002) Chemotaxis of *Ralstonia eutropha* JMP134(pJP4) to the herbicide 2,4-dichlorophenoxyacetate. *Appl Environ Microbiol* 68(2):968-972.
9. Don RH & Pemberton JM (1985) Genetic and physical map of the 2,4-dichlorophenoxyacetic acid-degradative plasmid pJP4. *J Bacteriol* 161(1):466-468.
10. Fisher PR, Appleton J, & Pemberton JM (1978) Isolation and characterization of the pesticide-degrading plasmid pJP1 from *Alcaligenes paradoxus*. *J Bacteriol* 135(3):798-804.
11. Adler J (1966) Chemotaxis in bacteria. *Science* 153(3737):708-716.
12. Mesibov R & Adler J (1972) Chemotaxis toward amino acids in *Escherichia coli*. *J Bacteriol* 112(1):315-326.

13. Armstrong JB, Adler J, & Dahl MM (1967) Nonchemotactic mutants of *Escherichia coli*. *J Bacteriol* 93(1):390-398.
14. Rothbauer M, Wartmann D, Charwat V, & Ertl P (2015) Recent advances and future applications of microfluidic live-cell microarrays. *Biotechnol Adv* 33(6):948-961.
15. Wessel AK, Hmelo L, Parsek MR, & Whiteley M (2013) Going local: technologies for exploring bacterial microenvironments. *Nat Rev Microbiol* 11(5):337-348.
16. Lim JW, Ha D, Lee J, Lee SK, & Kim T (2015) Review of micro/nanotechnologies for microbial biosensors. *Front Bioeng Biotechnol* 3:e61.
17. Ahmed T, Shimizu TS, & Stocker R (2010) Microfluidics for bacterial chemotaxis. *Integr Biol (Camb)* 2(11-12):604-629.
18. Kalinin YV, Jiang L, Tu Y, & Wu M (2009) Logarithmic sensing in *Escherichia coli* bacterial chemotaxis. *Biophys J* 96(6):2439-2448.
19. Mao H, Cremer PS, & Manson MD (2003) A sensitive, versatile microfluidic assay for bacterial chemotaxis. *Proc Natl Acad Sci U S A* 100(9):5449-5454.
20. Lanning LM, Ford RM, & Long T (2008) Bacterial chemotaxis transverse to axial flow in a microfluidic channel. *Biotechnol Bioeng* 100(4):653-663.
21. Englert DL, Manson MD, & Jayaraman A (2009) Flow-based microfluidic device for quantifying bacterial chemotaxis in stable, competing gradients. *Appl Environ Microbiol* 75(13):4557-4564.
22. Ahmed T, Shimizu TS, & Stocker R (2010) Bacterial chemotaxis in linear and nonlinear steady microfluidic gradients. *Nano Lett* 10(9):3379-3385.
23. Si G, Yang W, Bi S, Luo C, & Ouyang Q (2012) A parallel diffusion-based microfluidic device for bacterial chemotaxis analysis. *Lab Chip* 12(7):1389-1394.
24. Stocker R, Seymour JR, Samadani A, Hunt DE, & Polz MF (2008) Rapid chemotactic response enables marine bacteria to exploit ephemeral microscale nutrient patches. *Proc Natl Acad Sci U S A* 105(11):4209-4214.



25. Bi S, Pollard AM, Yang Y, Jin F, & Sourjik V (2016) Engineering hybrid chemotaxis receptors in bacteria. *ACS Synth Biol* 5(9):989-1001.
26. Culbertson CT, Jacobson SC, & Michael Ramsey J (2002) Diffusion coefficient measurements in microfluidic devices. *Talanta* 56(2):365-373.
27. Longworth L (1955) Diffusion in liquids and the Stokes-Einstein relation. *Electrochemistry in biology and medicine* ed Shedlovsky T (John Wiley & Sons, Inc., New York, N. Y.):pp 225-247.
28. Ni B, Huang Z, Fan Z, Jiang CY, & Liu SJ (2013) *Comamonas testosteroni* uses a chemoreceptor for tricarboxylic acid cycle intermediates to trigger chemotactic responses towards aromatic compounds. *Mol Microbiol* 90(4):813-823.
29. Crooks JA, Stilwell MD, Oliver PM, Zhong Z, & Weibel DB (2015) Decoding the chemical language of motile bacteria by using high-throughput microfluidic assays. *Chembiochem* 16(15):2151-2155.
30. Gerhardt P & American Society for Microbiology. (1981) *Manual of methods for general bacteriology / by Philipp Gerhardt, editor-in-chief ; R.G.E. Murray, editor, I. Morphology ... [et al.]* (American Society for Microbiology, Washington, D.C.) pp xii, 524 p.
31. Salman H & Libchaber A (2007) A concentration-dependent switch in the bacterial response to temperature. *Nat Cell Biol* 9(9):1098-1100.
32. Baba T, Ara T, Hasegawa M, Takai Y, Okumura Y, Baba M, Datsenko KA, Tomita M, Wanner BL, & Mori H (2006) Construction of *Escherichia coli* K-12 in-frame, single-gene knockout mutants: the Keio collection. *Mol Syst Biol* 2:e2006.0008.
33. Ditta G, Stanfield S, Corbin D, & Helinski DR (1980) Broad host range DNA cloning system for gram-negative bacteria: construction of a gene bank of *Rhizobium meliloti*. *Proc Natl Acad Sci U S A* 77(12):7347-7351.
34. Buffi N, Beggah S, Truffer F, Geiser M, van Lintel H, Renaud P, & van der Meer JR (2016) An automated microreactor for semi-continuous biosensor measurements. *Lab Chip* 16(8):1383-1392.

35. Berg HC & Brown DA (1974) Chemotaxis in *Escherichia coli* analyzed by three-dimensional tracking. *Antibiot Chemother* (1971) 19:55-78.
36. Sbalzarini IF & Koumoutsakos P (2005) Feature point tracking and trajectory analysis for video imaging in cell biology. *J Struct Biol* 151(2):182-195.
37. Bruus H (2008) *Theoretical microfluidics* (Oxford University Press, Oxford ; New York) p 346 p.
38. Keller EF & Segel LA (1971) Model for chemotaxis. *J Theor Biol* 30(2):225-234.
39. Chen KC, Ford RM, & Cummings PT (1998) Perturbation expansion of Alt's cell balance equations reduces to Segel's one-dimensional equations for shallow chemoattractant gradients. *Siam Journal on Applied Mathematics* 59(1):35-57.
40. Ma YG, Zhu CY, Ma PS, & Yu KT (2005) Studies on the diffusion coefficients of amino acids in aqueous solutions. *Journal of Chemical and Engineering Data* 50(4):1192-1196.
41. Kayahara T, Thelen P, Ogawa W, Inaba K, Tsuda M, Goldberg EB, & Tsuchiya T (1992) Properties of recombinant cells capable of growing on serine without NhaB Na<sup>+</sup>/H<sup>+</sup> antiporter in *Escherichia coli*. *J Bacteriol* 174(22):7482-7485.
42. Coronado E, Valtat A, & van der Meer JR (2015) *Sphingomonas wittichii* RW1 gene reporters interrogating the dibenzofuran metabolic network highlight conditions for early successful development in contaminated microcosms. *Environ Microbiol Rep* 7(3):480-488.
43. Don RH, Weightman AJ, Knackmuss HJ, & Timmis KN (1985) Transposon mutagenesis and cloning analysis of the pathways for degradation of 2,4-dichlorophenoxyacetic acid and 3-chlorobenzoate in *Alcaligenes eutrophus* JMP134(pJP4). *J Bacteriol* 161(1):85-90.



## CHAPTER 3

### CHARACTERIZATION OF SINGLE CELL CHEMOTAXIS RESPONSES USING A MICROFLUIDIC CHIP

Microfluidics is an interesting tool for the quantification of bacterial chemotaxis response. The small scale dimensions allow a potential faster detection of the cellular response compared to traditional population-based methods, such as swimming plates. We hypothesized that the trajectory analysis of single cells may be used for quantifying chemotaxis read-out. In this chapter, we developed a microfluidic chip that integrates pressure-driven valves, in which a gradient of attractant can be generated by alternating valve opening, and small groups of cells can be injected inside an established gradient. Serine gradients were established with 100  $\mu\text{M}$  or 10  $\mu\text{M}$  source concentration and the trajectory responses of individual *Escherichia coli* cells were recorded within the first minutes. Contrary to our expectations, trajectory properties (angle, total length, etc.) were not statistically significant different among cells injected into serine gradients or into buffer alone. Stochastic mathematical modeling of single-cell response suggested that an increase of incubation time might have resulted in clearer chemotaxis differences.

## Introduction

In Chapter 2, we developed a microfluidic chip that allows quantification of *Escherichia coli* and *Cupriavidus pinatubonensis* chemotaxis at population level towards a variety of individual attractants. Despite this, this type of chip required accurate and sensitive control of the flow of both attractant and cells, and did not allow easy sample exchange. Sample exchange is particularly difficult in microfluidics, since one needs to transfer liquid handling from a macro-scale (syringes, tubings,  $\mu\text{l}$ -ml volumes) into the micro-scale fluidics (chip channels, nL volumes). In our perspective, this liquid-downscaling aspect complicates testing of different consecutive samples since the dead volume of tubing and connections before entering into the flow reaction channels is enormous compared to the actual microfluidic channels, and thus will take a very long time.

In order to possibly alleviate this issue, one can integrate fluidic valves inside the chip structure, which allows better control of the flow inside the chip and facilitates the exchange of samples, too. Valves can be positioned inside fluidic channels by fabricating two layers of polydimethylsiloxane (PDMS) [1]; the upper of which contains the valves, and the lower the regular flow channels (Fig. 1A). The layer of PDMS between the valve and the channel is kept very thin; pressure application on the valves will deform into the flow channels below and effectively closing it (Fig. 1).

In a recent publication, it was shown that stable chemical gradients could be produced by alternating opening of two valves flanking a test channel [2]. In brief, a source and a sink were created on each side of the test channel, separated by valves. By opening alternately the valves on each side, a stable gradient is formed in the test channel, which can persist for a few minutes even when both valves are closed [2].

The goal of this work was to measure the chemotaxis response of individual *E. coli* cells to a stable chemical gradient in an observation channel, using the principle of alternating valve opening. Our idea was that, once the gradient is established, a group of *E. coli* cells can be

introduced in the middle of the gradient, using a different channel inlet. Since the cells will find themselves within the gradient with minimal disturbance, they should react with a biased swimming response to the gradient source. The direct bacterial response could then be measured for the first couple of minutes after introduction into the chemical gradient. Individual bacterial trajectories can be extracted from the real-time movies.

With this setting we expected to measure a difference in individual trajectories properties in the first minutes of exposure to a gradient, which would provide fast chemotaxis quantification at individual cell level. In a recent publication, Choi *et al.* showed the chemotaxis response of *Salmonella typhimurium* towards different changing attractant gradients in a microfluidic chip. They showed significant bias in trajectory directions only 120 s after cell insertion in the gradient [3]. Others used swimming direction asymmetry and chemotaxis velocity extracted from individual trajectory as chemotaxis descriptor [4], as well as run lengths and run durations [5]. Deeper analysis of bacterial trajectories allows precise identification of run and tumble events, which could provide a non-invasive method to study flagellar rotation instead of common tethering cell assay [6].

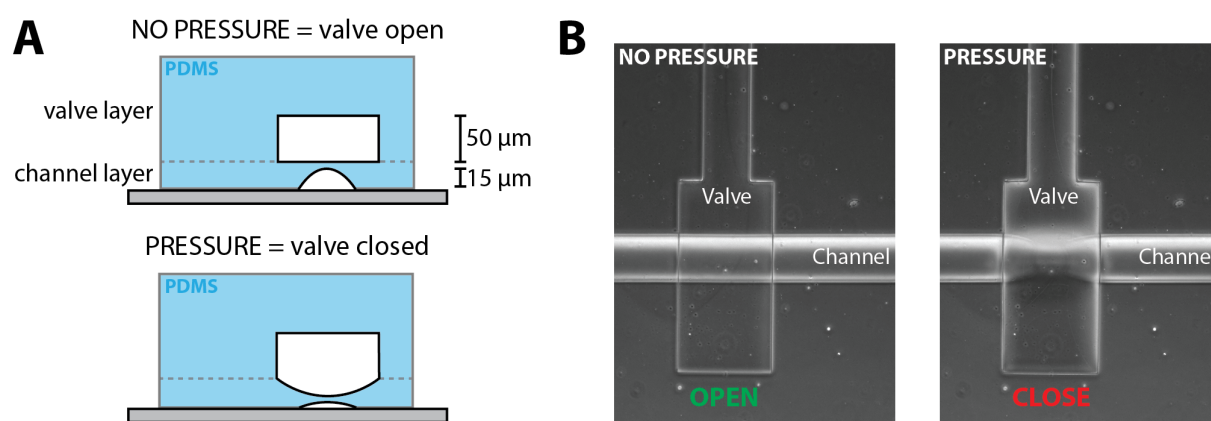


**Figure 1: Principle of PDMS integrated microfluidic valves. (A)** Vertical slice of a double layer PDMS chip with the valve in the upper layer and the channel in the lower layer. Without application of air-liquid pressure in the valve, the channel below is open (upper schematic). Increasing pressure in the valve deforms the PDMS and closes the channel below (lower schematic). **(B)** Images at 10x magnification of an open (left) and a closed valve (right).

## Results

### *Gradient generation in the double layer PDMS chip*

In order to characterize bacterial chemotaxis response at individual cell level, we developed a double-layer microfluidic chip that integrates pressure-driven valves inside the PDMS structure (Fig. 2A). The chip comprises three parallel observation channels, in which a gradient can be generated and bacterial cells can be introduced simultaneously (Fig. 2A, Inset). The gradient is generated by alternative valve opening, the principle of which was described previously [2]. In short, the attractant and the buffer are flowed in the side channels; alternating opening of valves to the middle channel during 120 ms with intermittent closing for 10 s, leads to diffusion of the attractant from the source to the sink (buffer) channel. Alternating opening of source and sink valves results in a stable, almost linear gradient in the observation channel (Fig. 2B). A group of bacteria ( $n \sim 100$  cells) can be inserted by a short pulse and opening of the valve in the middle of observation channel, and their chemotaxis response to the gradient can be monitored in real-time by microscopy. After completion of the experiment the cells can be washed away and another cycle of chemotaxis can be performed.

The formation and maintenance of the gradient was tested with fluorescein isothiocyanate-dextran (FITC-dextran). Fluorescence measurements over time along the observation channel showed that the gradient formed rapidly and was stable after 30 min of alternating valve opening (Fig. 2C).

After 30 min of gradient formation, we mimicked the effect of introducing bacteria by a 4-s opening of the middle valves (Fig. 2B), followed by 2 min of no further valve opening during which the chemotaxis response may be monitored. Quantification of the FITC-dextran fluorescence signal indicated that, immediately after inflow from the cell inlet, the gradient was perturbed at the position of the inflow (in green on Fig. 2D). The gradient re-established rapidly within 15 to 30 s and remained stable for the remaining 90 s (Fig. 1D). Measurements of the FITC-dextran gradient in the microfluidic chip thus suggest that it is possible to create an

attractant gradient, which is stable enough to introduce bacterial cells and should permit to follow their chemotaxis for a period of 2 min after inflow.

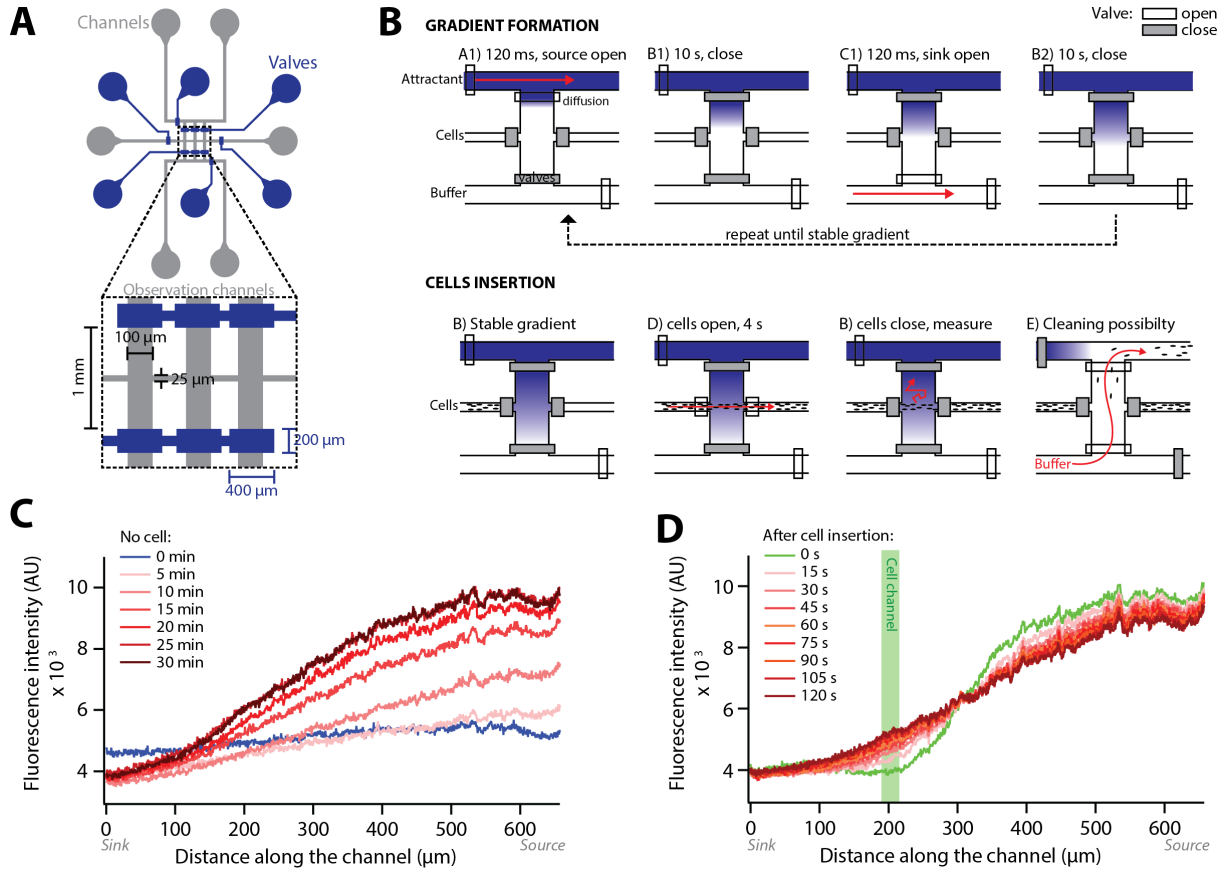


**Figure 2: Design of a gradient generator chip for chemotaxis measurements. (A)** Layout of the double-layered microfluidic chip with the flow channels on the bottom (grey) and the control valves as upper layer (blue). Inset shows a detail of the three parallel observation channels with dimensions. **(B)** Principle of attractant gradient formation through alternating valve opening, and inflow of cells after gradient establishment. **(C)** FITC-Dextran gradient formation over time in the first observation channel as a result of alternating valve opening. The distance 0 corresponds to the bottom of the observation channel (position of the sink) and the distance 600 corresponds to the other side (position of the source). **(D)** FITC-Dextran gradient perturbation after inflow of liquid mimicking cell insertion (green zone) and its subsequent persistence in the fully closed configuration.



### *Characterization of individual trajectories*

In order to characterize the direct chemotaxis response of individual bacteria introduced in the middle of a pre-established gradient, we tested the response of *E. coli* MG1655-gfp towards a gradient of serine. After 30 minutes of alternating valve opening, a group of cells was introduced into the observation channel by a 4-s opening of the middle valves. Valves remained closed in order to abolish all flow inside the observation channel during the cell response. Five consecutive 30-s movies were taken and individual bacterial trajectories were extracted. The trajectories were characterized by different properties to try to discriminate chemotaxis in presence of a gradient (with a 100  $\mu$ M or 10  $\mu$ M source of serine) to the random response in a uniform control environment (only buffer). This first trajectory descriptor was the length, since we expected longer trajectories in presence of attractant due to the decreased number of tumbles (change of direction). We calculated the total length of each trajectory as well as the final length – the straight distance between the starting point and the end point of the trajectory (Fig. 3F). The average lengths of the trajectories (total and final) were not longer in presence of a gradient although the variability between the experimental replicates was important (Fig. 3A-B). In addition, the ratio of the total length divided by the final length was calculated in order to characterize the straightness of the trajectories. The principle is that, when a trajectory is straight, the final length tends to be as long as the total length and the ratio tends to 1. We expected to obtain straighter trajectories in presence of the gradient. The average ratios of the trajectories in presence of gradient were systematically higher than the first buffer replicates, which suggests straighter trajectories (Fig. 3C). However the second replicate of the buffer showed a value similar to the gradient replicates (Fig. 3C).

We also measured the final vertical displacement of the cells (Fig. 3F). Since the source of the gradient is localized at the top, cells swimming towards the source will display a positive average vertical displacement. The results did not show any preference in vertical direction or more displacement towards the sink (Fig. 3D). Neither did the proportion of the cells that swam

towards the source show any preference for the direction of source, with about 50% or less of the cells swimming in the direction of the source (Fig. 3E).

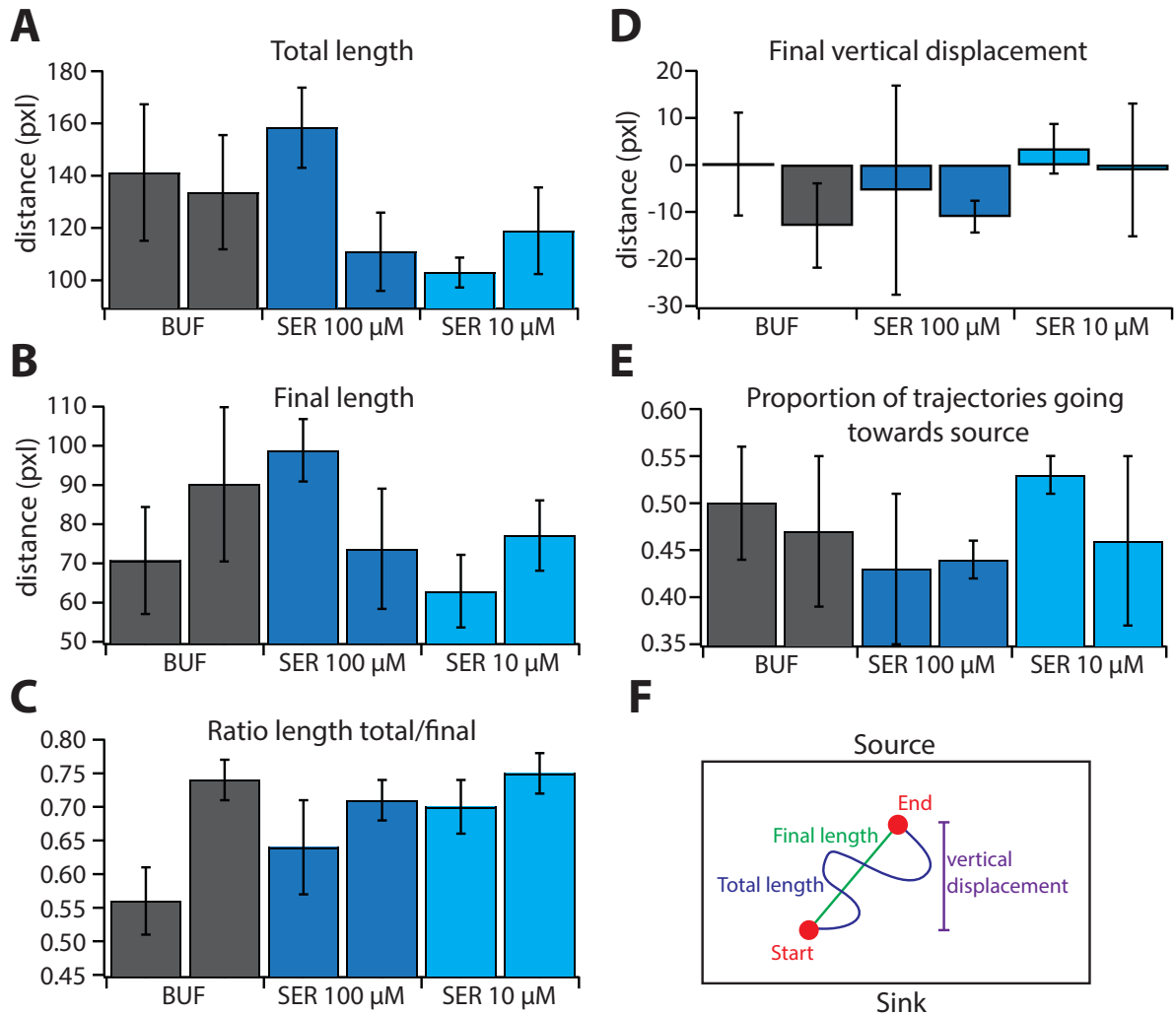


**Figure 3: Individual bacterial trajectory properties in presence or absence of gradient.**

Individual trajectories were extracted from five consecutive 30-s movies after direct exposure of the bacteria to an absence of gradient (BUF) or a gradient with a 100  $\mu\text{M}$  serine source (SER 100  $\mu\text{M}$ ) or a gradient with a 10  $\mu\text{M}$  serine source (SER 10  $\mu\text{M}$ ). The different graphs show the trajectory properties measured from two independent replicate experiments for each condition. **(A)** Average total length of trajectories. **(B)** Average final length of the trajectories, which corresponds to the direct distance between the starting and the end points. **(C)** Average of the ratios of the total length divided by the final length for each trajectory. A ratio tending to 1

characterizes straighter trajectories. **(D)** Average of final vertical displacements of trajectories, which corresponds to the vertical length between the starting and the end points of the trajectory. **(E)** Proportion of the trajectories, whose average direction pointed towards the source of serine (Upwards). **(F)** Scheme that describes the different trajectory properties measured.

In addition to the trajectory descriptors, we calculated the angle of average direction of the trajectories. The direction distribution for all replicates and conditions showed a preference in the vertical displacement, which can be explained by the smaller width of the channel. However, no significant preference for the source direction was observed when the cells were in presence of a gradient compared to the uniform environment (Fig. 4).

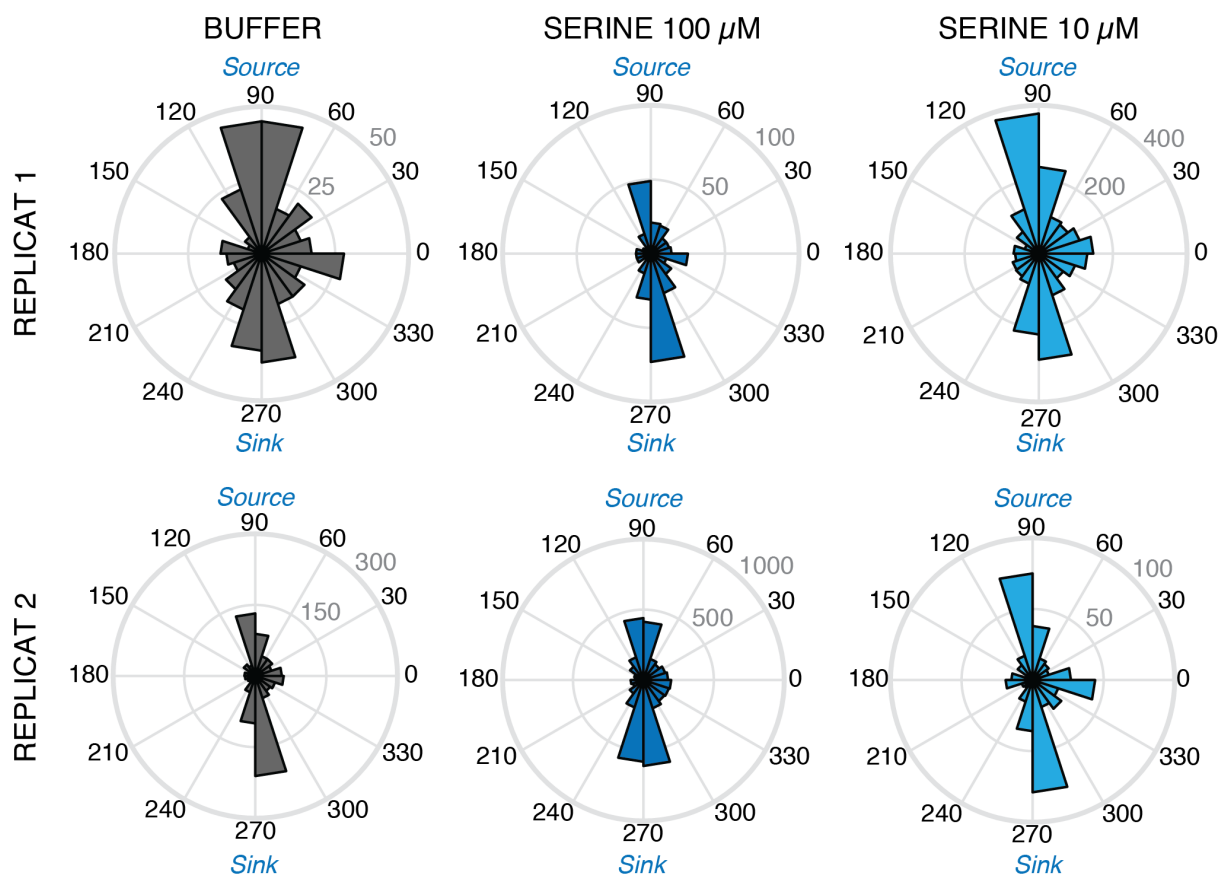


**Figure 4: Histograms of average angle of individual trajectories.** Individual trajectories were extracted from five consecutive 30-s movies after direct exposure of the bacteria to an absence of gradient or a gradient with a 100  $\mu\text{M}$  or 10  $\mu\text{M}$  serine. The graphs show the circular distribution of the average direction of each individual trajectory measured from two independent replicates of experiment. The source of serine is localized at the top and the sink at the bottom.

These results suggest that the trajectories of bacteria in absence or in presence of a gradient of serine were not significantly different in the 2 first minutes of chemotaxis response. Moreover, an important variability between the different experimental replicates was observed.

#### *Comparison of experimental data with mathematical modeling*

In addition to the previous trajectory parameters, we compared the bacterial distributions in the observation channel after 2.5 minutes of response. Bacterial distributions were very similar whether the cells were exposed to a gradient or not (Fig. 5A). No bias towards the source was observed in the experimental data. The bacteria were homogeneously distributed in the channel after 2.5 min of exposure (Fig. 5B).

In order to understand why we were not able to detect a response in the chip, we collaborated with Xavier Richard and Christian Mazza, mathematicians at the University of Fribourg, who developed a model that predicts the movement of individual mathematical cells in presence of a gradient of attractant. The response of 200 cells inserted in the middle of a channel of 100  $\mu\text{m}$  width and 1000  $\mu\text{m}$  long during 2.5 min was simulated, which is comparable to our experimental data. Simulations suggested slight accumulation of cells close to the source with a gradient of 10  $\mu\text{M}$ , but hardly any for a gradient of 100  $\mu\text{M}$  serine, which was similar to the distribution in absence of gradient (Fig. 5C).

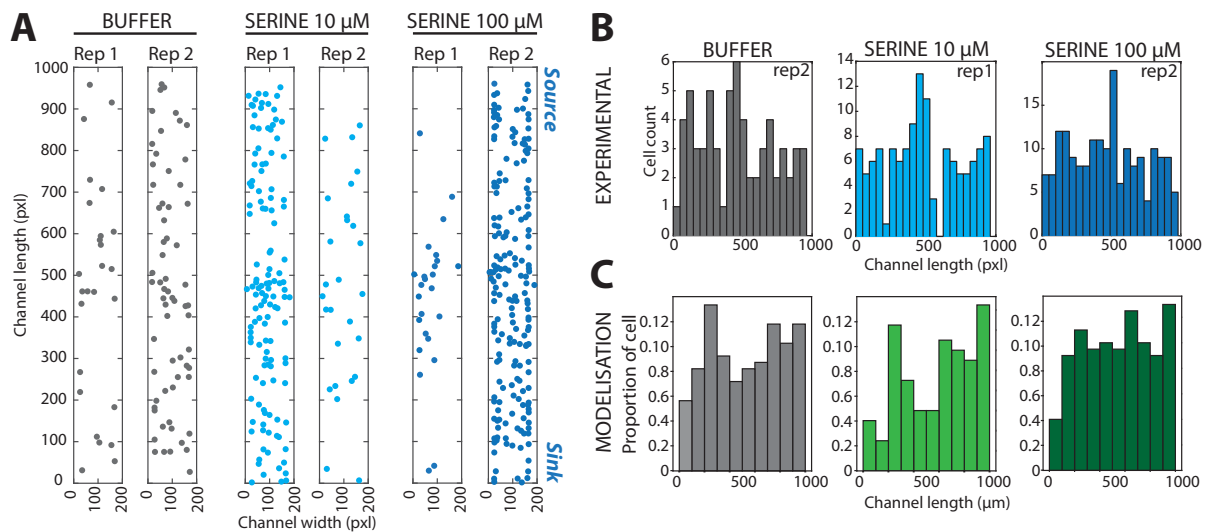


**Figure 5: Position of the cells in the channel. (A)** Experimental positions of *E. coli* cells in the channel after 2.5 minutes of exposure to either an absence of gradient or a gradient with a 100  $\mu\text{M}$  or 10  $\mu\text{M}$  serine source with two independent experimental replicates. Source of serine is located at 1000  $\mu\text{m}$  and the sink at 0  $\mu\text{m}$ . **(B)** Histograms of the observed distribution of the cells across the length of the channel. **(C)** Distributions obtained from mathematical simulations of cells across the length of the channel. Note that the source of serine is located at 1000  $\mu\text{m}$  and the sink at 0  $\mu\text{m}$ .

In order to identify which aspect to improve in our setup, we changed different parameters in the model to see whether and how we might obtain a better chemotaxis response. First, we simulated bacterial chemotaxis response during longer incubation time. Incubations of 20 min simulation time indicated cell distributions largely biased towards the source in presence of gradients of 10  $\mu\text{M}$  and 100  $\mu\text{M}$  of serine, which were significantly different from the simulation in absence of gradient (Fig. 5A). Secondly, insertion of cells closer to the source of attractant (position: 750  $\mu\text{m}$ ) yielded accumulation after 2.5 min. This also occurred with cells inside buffer only but to a lesser extent than cells in serine gradients (Fig. 5B). Finally, simulations with 100 times more cells in the channel ( $n=20,000$ ), also yielded cell accumulation

within 2.5 min, which was higher for 10  $\mu\text{M}$  serine gradient than with buffer alone or 100  $\mu\text{M}$  gradient (Fig. 6C). Simulations thus suggest one could either increase incubation time, place the cell inlet closer to the source, or introduce more cells, in order to detect cell accumulation near the source within short times.

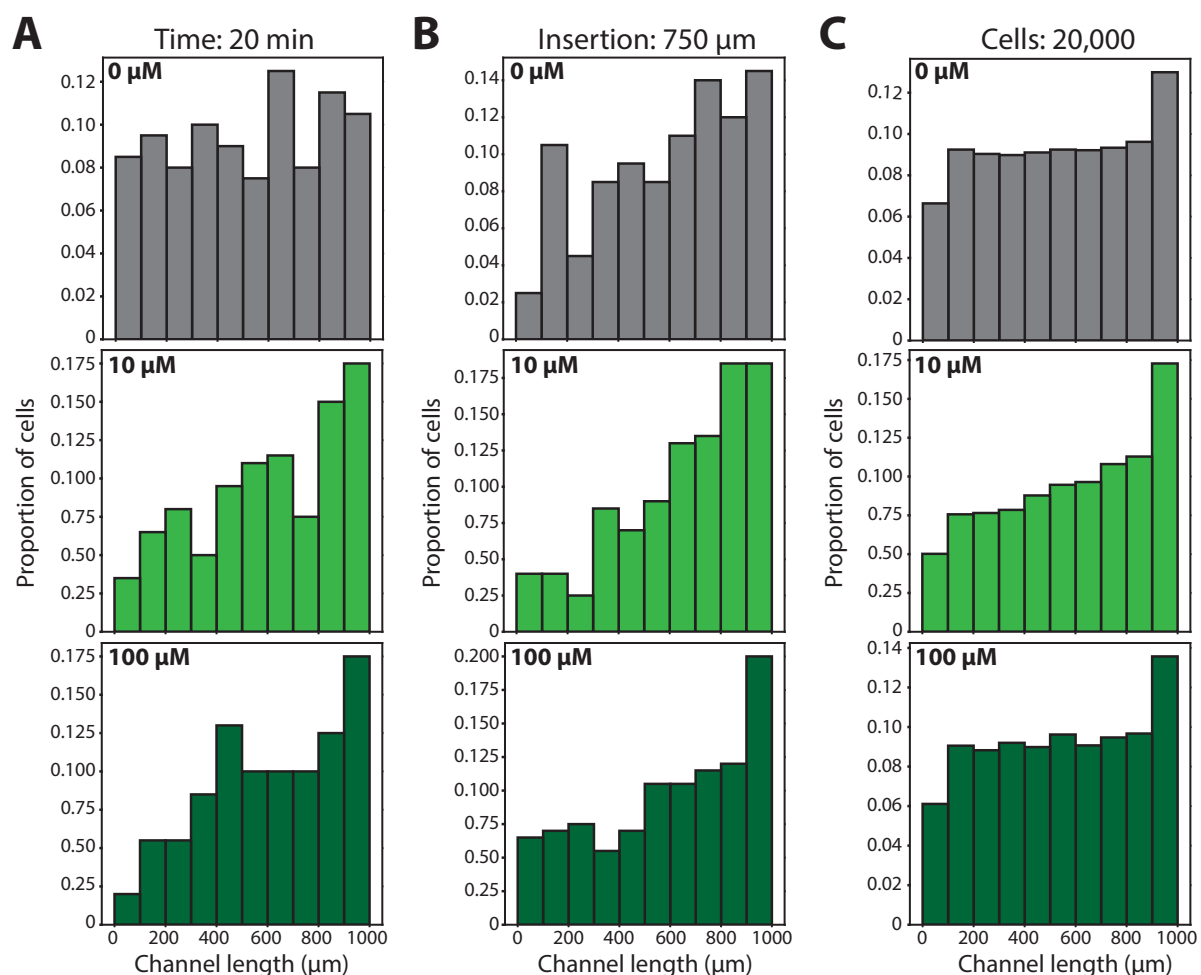


**Figure 6: Mathematical modeling of bacterial position in the observation channel.**

Bacterial distribution along the observation channel in absence of gradient (0 mM) or in presence of a gradient of serine (source: 0.01 mM or 0.1 mM). Source of serine is located at 1000  $\mu\text{m}$  and the sink at 0  $\mu\text{m}$ . **(A)** Modeling of the position of 200 cells inserted in the middle (500  $\mu\text{m}$ ) after 20 min. **(B)** Modeling of the position of 200 cells inserted close to the source (750  $\mu\text{m}$ ) after 2.5 min. **(C)** Modeling of the position of 20,000 cells inserted in the middle (500  $\mu\text{m}$ ) after 2.5 min. Note that the scales are different between the graphs.

## Discussion

In this chapter, we designed a double-layer microfluidic chip that integrated pressure-driven valves inside the PDMS structure. It allowed a fine control of the flow in the chip and exchange of sample was facilitated because the valves can be closed during the change of tubing, which prevents the disturbance of the liquid flow inside the chip. A disadvantage of this chip is the effort needed for fabrication. Two PDMS layers have to be produced in parallel and aligned accurately. It also requires more important additional periphery material, such as air bottles for pressure, a valve controlling device and computer.

We aimed to create a gradient by alternating valve opening, then insert a group of motile *E. coli* bacteria in the middle of the pre-established gradient and follow their immediate response by video microscopy. Stable gradients could be generated after 30 min of alternating valve opening, which persisted without further valve opening for few minutes (Fig. 2). This, we expected, would permit to follow chemotaxis response of individual cells after insertion. On-chip measurements can be performed multiple times by washing the cells away, however, every consecutive measurement requires some time to re-establish the gradient.

The trajectory behavior of individual cells was accurately extracted from video microscopy over 2.5 min in presence or absence of a gradient. We could determine a variety of responses, such as total and final trajectory length, trajectory angle and final cell distributions. Unfortunately, we could only perform two independent measurements on the chips, and cell trajectories in these cases were not different between cells introduced inside serine gradients (10 or 100  $\mu\text{M}$ ) and buffer alone (Fig. 3-5). Of note that the variability of the chip was still very important, resulting in batches of very different cell numbers (e.g., Fig. 5A).

In order to understand better how single cells respond in the gradients generated by the chip, we simulated their movement using a stochastic mathematical model, which is based on the probability of biased movement inside gradients as a function of generalized chemotaxis parameters (see Chapter 2), calculated using a metropolis chain [7, 8]. The simulated

distribution of 200 cells, only 2.5 min after insertion in the middle of a gradient of 10  $\mu\text{M}$  serine, showed a slight bias towards the source region, whereas the distribution in presence of 100  $\mu\text{M}$  source was similar to the simulation in absence of gradient (Fig. 5). This shows that we should be able to see a bias distribution of the cells with 10  $\mu\text{M}$  source, which is in agreement with the results obtained in chapter 2 where we measured fastest response with 10  $\mu\text{M}$  serine. Further simulations with varied parameters suggested that an increase in incubation time, a higher number of introduced cells, and a changed position of cell inlet could improve the measurements. Increasing incubation time may not be very practical as the gradient would slowly dissipate without further opening-and-closing of source and sink channels. Unfortunately, the time was too short to refabricate new chips or experimentally test the simulation predictions.

Which changes can further be implemented in the microfluidic chip design to improve single cell chemotaxis movements? It would likely be favorable to increase the width of the observation channels. We observed that several cells have the tendency to follow the border of the channels, probably because they are trapped in the border-liquid interface, which introduces a bias in the trajectory data. Larger observation channels would decrease the probability to encounter a wall and would allow better swimming. The three parallel observation channels, which we designed in order to have replicates on the same chip, also caused problems, in particular perturbing flow between the observation channels when opening-and-closing for gradient continuation. Only one observation channel or multiple independent channels might solve this issue. Finally, we noted that several cells showed circular trajectories, which was shown to an artifact due to bacteria being trapped near the solid surface ceiling and floor [9]. Procedures need to be developed to exclude such trajectories from the data analysis.

To conclude, we developed a double-layer microfluidic integrated valves, which can generate a gradient and allow the characterization of chemotaxis response at single-cell level. We were not able to measure significant differences between bacterial trajectories in presence



or in absence of serine gradients. Modification of the chip design or introduction of larger cell groups would increase the chance to measure a chemotaxis response.

## Material and methods

### *Chip design and fabrication*

The microfluidic chip was designed using CleWin4 software and fabricated with an alignment of two polydimethylsiloxane (PDMS) layers. The channels measured 100  $\mu\text{m}$  wide and the valves were 200 x 400  $\mu\text{m}$  square aligned over the channels to be closed (Figure 2A).

Inverted silicon molds were fabricated in the cleanroom by standard soft photolithography and etching processes, as described previously [10]. The valve imprints on silicon mold were produced by a photolithography step and etching to obtain structures of 50  $\mu\text{m}$  high. The channel imprints were produced by photolithography followed by a baking process to make rounded channels of 15  $\mu\text{m}$  high. Both PDMS layers were then fabricated as a negative imprint of the silicon molds. Hereto a mixture of Syglard 184 silicone elastomer base and curing agent (Dow Corning) with a 5:1 ratio was poured on the valve mold (height: ca. 5 mm). The channel layer was made with a mix of 20:1 of PDMS and with a height of only about 30  $\mu\text{m}$  produced using a spin coater. After the deposition of the PDMS, both coated silicon mold were incubated for 13 min at 80°C. The valve layers were cut and peeled off from the mold, inlets were punched and the PDMS pieces were aligned above the channel layer. The chips were then incubated for 16 hours more at 80°C. To finish the whole chips were cut and peeled off from the mold and inlets were punched.

### *Microfluidic chip operation*

Just before use, the PDMS chip was bonded to a standard glass microscopy slide using oxygen plasma treatment for 0.1 min (FEMTO plasma cleaner from Diener Electronic, settings: 0.6 mbar, 100 W). The valves were filled with water. Valve closing and opening were driven by air pressure and controlled by homemade devices and a custom LabVIEW program (National Instruments) developed by Oliver Gubler of the HES-SO, Sion. Liquid flows were driven either by a syringe pump (attractant and buffer) or by gravity force (cell suspension in an open inlet).

### *Preparation of cells for chemotaxis assays*

*E. coli* MG1655-gfp was grown overnight in M9-Glc-Tc25 at 37°C with 180 rpm shaking (see chapter 2). The culture was diluted 100 fold in fresh M9-Glc-Tc25 medium and incubated for 3 hours at 37°C, until reaching an OD<sub>600</sub> of about 0.5. The culture was centrifuged at 2,400 × g for 5 min and washed three times with motility buffer (see chapter 2). The cells were finally resuspended in 1 ml of motility buffer supplemented with 0.1% of Triton X-100 to prevent sticking of the cells on the walls of the chip (this had no measurable effect on cellular movement).

### *Gradient characterization*

The gradient was created in the observation channels by alternating valve opening. In order to characterize the gradient, we replaced the attractant by fluorescein isothiocyanate-dextran (FITC-dextran) solution (Sigma-Aldrich). Thus buffer and FITC-dextran were flowed in the side channels using a syringe pump with a flow rate of 0.2 μl min<sup>-1</sup>. To create the gradient, the valve near the source (FITC-dextran) opened for 120 ms followed by closing for 10 s of all valves; then the valve near the sink (buffer) opened for 120 ms followed by closing for 10 sec of all valves (Fig. 2B). This cycle was repeated multiple times during 30 min. Fluorescence images of the observation channel were taken every minute during 30 min of repeating operating cycle. After 30 min of gradient establishment, bacterial cell insertion in the middle channel was mimicked by 4-s valve opening (Fig. 2B). Fluorescence images were taken every 15 s during 3 minutes after 'cell' insertion in order to characterize the perturbation of the gradient by the cell flow and its persistence over time. Fluorescence profiles were extracted using ImageJ software.

### *Chemotaxis assays*

Solutions of 100 μM serine and motility buffer, supplemented with 0.1% of Triton X-100, were flowed in each of the side channels at a flow rate of 0.2 μl min<sup>-1</sup> using a double syringe

pump (NE-4000, NewEra, Pump System Inc.). Freshly prepared cells were inserted in the cell inlet using a pipette and were pushed to the valve by gravity pressure by inserting a 200  $\mu\text{l}$  pipette tip into the inlet. The observation channels were washed in order to remove all the bacteria that reached it (Fig. 2B washing).

The gradient was established by alternation valve opening (120 ms open, 10 s close) during 30 min. Cells were inserted into the observation channel by 4-s valves opening. Fluorescence images series (every 300 ms) were taken during 30 s using a DFC 350 FX R2 Leica camera mounted on an inverted DMI 4000 Leica microscope using a N PLAN 10X objective. Five consecutive sequences were taken (total 2.5 min). After exposure, the cells were washed away and the gradient was re-established for a consecutive exposure. Three exposures were performed at most because of the decrease of chemotaxis performance with time spent in the motility buffer in the chip. Only the first exposure data were used for trajectory analysis. Individual cell trajectories were extracted using the *mosaic 2D tracking* plugin in ImageJ [11]. Coordinates of the trajectories were exported to MATLAB (version R2015\_b, MathWorks, Inc.) for further analysis using homemade custom scripts.

### *Kinetic model description*

This mathematical model was developed by Xavier Richard and Christian Mazza (University of Fribourg, Switzerland).

**Metropolis algorithm.** In order to describe the dynamics of bacterial chemotaxis and its time development in the microfluidic chip, we constructed an individual cell-based model based on the so-called *metropolis* algorithm [7, 8].

**Simulation in absence of chemoattractant.** In absence of chemoattractant the cells have no preferred direction of motion, and their path can be described by a random walk. At the start of simulation, 200 or 20,000 cells were chosen at a defined position (pos. = 500  $\mu\text{m}$  or 750  $\mu\text{m}$ ) on a  $z_1 \times z_2$  grid that represents the dimensions of the microfluidic observation channel

(100 x 1000  $\mu\text{m}$ ). Then, at each time step, for every point  $p_i = (x_i, y_i)$  a new position  $p_i^{next} = (x_i^{next}, y_i^{next})$  is computed with

$$p_i^{next} = (x_i^{next}, y_i^{next}) = (x_i + v\cos(\theta), y_i + v\sin(\theta)) \quad (9)$$

with  $v$  corresponding to the distance between  $p_i$  and  $p_i^{next}$ , and  $\theta$  a random angle uniformly chosen between 0 and 360°.

**Simulation in presence of chemoattractant.** In presence of chemoattractant the cells will bias their direction of motility according to a probability  $\mu_\beta$  to reach position  $p = (x, y)$  on the grid, given by Gibbs' probability measure [8]:

$$\mu_\beta(p) = \frac{\exp(-\beta H(p))}{Z(\beta)} \quad (10)$$

where  $H$  is a general function (see below),  $\beta$  a free parameter, and  $Z(\beta)$  the partition function of the system, defined by:

$$Z(\beta) = \sum_{p \in \Lambda} \exp(-\beta H(p)) \quad (11)$$

and with  $\Lambda$  being the set of all possible states for  $p$ . Since  $\Lambda$  is not finite nor countable,  $Z(\beta)$  cannot be computed. Instead, one can compute the probability  $q_\beta(p, p')$  to go from position  $p$  to position  $p'$  by using the metropolis chain, which is defined by:

$$q_\beta(p, p') = q_0(p, p') \exp(-\beta(\Delta H)^{pos}) \quad (12)$$

where  $\Delta H = H(p') - H(p)$ ,  $(x)^{pos} = \max\{0, x\}$ , and  $q_0(p, p')$  is the probability to go to position  $p'$  from  $p$  in absence of attractant.

For each step of the simulation, the next position  $p_i^{next}$  for every cell is computed using the following sequence:

1. A random  $p_i^{target}$  is chosen according to equation (9),
2. If  $H(p_i^{target}) - H(p_i) < 0$ ,  $p_i^{next} = p_i^{target}$ ,
3. Else,  $p_i^{next} = p_i^{target}$  with probability  $\exp(-\beta(H(p_i^{target}) - H(p_i)))$  and  $p_i^{next} = p_i$  with probability  $1 - \exp(-\beta(H(p_i^{target}) - H(p_i)))$ .

**The function H.** The function H represents the bacterial sensing of the chemical gradient. According to [8] bacteria sense the relative change of attractant, with  $c_S$  again representing the ligand concentration, as follows:

$$\Delta H = \frac{\Delta c_S}{c_S} \quad (13)$$

When taken the chemotactic sensitivity and receptor saturation into account, the following term is included, with  $K_C$  being the receptor-ligand dissociation constant (see Chapter 2), producing:

$$\Delta H = \frac{\Delta c_S}{c_S} \frac{K_C c_S}{(K_C + c_S)^2} \quad (14)$$

Equation 14 is further developed by using a mean ligand concentration  $c_{S,0}$  along the microfluidic channel segment length, and by applying a factor  $\alpha$  that corrects for the difference in measured and true chemotactic sensitivity, according to the Stewen's power law. Finally, we add a factor  $a$  that describes the adaptation of the cells to the chemoattractant, and which takes the form of a logistic function

$$a = \frac{b}{(1 + \exp(-k(t - t_0)))}$$

Putting all those terms together leads to the equation for  $H$

$$\Delta H = a \left( \frac{K_C c_{S,0}}{(K_C + c_{S,0})^2} \right)^\alpha \frac{\Delta c_S}{c_S} \quad (15)$$

which is the term we substitute for  $\Delta H$  in equation (10).

## Acknowledgements

I want to thank Xavier Richard who developed the mathematical model and ran the computer simulations.

## References

1. Unger MA, Chou HP, Thorsen T, Scherer A, & Quake SR (2000) Monolithic microfabricated valves and pumps by multilayer soft lithography. *Science* 288(5463):113-116.
2. Frank T & Tay S (2013) Flow-switching allows independently programmable, extremely stable, high-throughput diffusion-based gradients. *Lab Chip* 13(7):1273-1281.
3. Choi E, Chang HK, Lim CY, Kim T, & Park J (2012) Concentration gradient generation of multiple chemicals using spatially controlled self-assembly of particles in microchannels. *Lab Chip* 12(20):3968-3975.
4. Ahmed T & Stocker R (2008) Experimental verification of the behavioral foundation of bacterial transport parameters using microfluidics. *Biophys J* 95(9):4481-4493.
5. Kovarik ML, Brown PJ, Kysela DT, Berne C, Kinsella AC, Brun YV, & Jacobson SC (2010) Microchannel-nanopore device for bacterial chemotaxis assays. *Anal Chem* 82(22):9357-9364.
6. Masson JB, Voisinne G, Wong-Ng J, Celani A, & Vergassola M (2012) Noninvasive inference of the molecular chemotactic response using bacterial trajectories. *Proc Natl Acad Sci U S A* 109(5):1802-1807.
7. Beichl I & Sullivan F (2000) The metropolis algorithm. *Computing in Science & Engineering* 2(1):65-69.
8. Mazza C & Benaïm M (2014) *Stochastic dynamics for systems biology* (CRC Press, Taylor & Francis Group, Boca Raton, FL) pp xii, 260 p.
9. Son K, Brumley DR, & Stocker R (2015) Live from under the lens: exploring microbial motility with dynamic imaging and microfluidics. *Nat Rev Microbiol* 13(12):761-775.
10. Buffi N, Beggah S, Truffer F, Geiser M, van Lintel H, Renaud P, & van der Meer JR (2016) An automated microreactor for semi-continuous biosensor measurements. *Lab Chip* 16(8):1383-1392.

11. Sbalzarini IF & Koumoutsakos P (2005) Feature point tracking and trajectory analysis for video imaging in cell biology. *J Struct Biol* 151(2):182-195.





# CHAPTER 4

## ENGINEERING A SPLIT-GFP FUSION TO MEASURE CHEY AND CHEZ INTERACTION

Chemotaxis signal transduction is based on protein-protein interactions and phosphorylations, which provide a fast response to the binding of an attractant or a repellent to the chemoreceptors. In particular, the ratios between bare and phosphorylated CheY (CheY~P) and the frequency of interactions with CheZ change upon addition of an attractant or a repellent to an *Escherichia coli* cell. In this chapter, we attempted to measure CheY~P-CheZ interactions by fusing them individually with non-fluorescent parts of a 'split'-Gfp that will reconstitute a fluorescent protein upon interaction. Specific fluorescent foci were present in cells when both fusion proteins were expressed, but not in *E. coli* lacking CheA, the kinase phosphorylating CheY. This demonstrates productive interaction between CheY~P and CheZ. Fluorescent foci were very stable in cells, although some changes were observed in cells induced by addition of nickel as repellent.

## Introduction

In both previous Chapters (2 and 3), we demonstrated how direct measurement of cellular motility may be used as readout for chemotaxis sensing, potentially enabling biosensor applications of chemotaxis pathways. The chemotaxis response by cells is rapid (ms–s scale) and does not require *de novo* gene induction, since it is based on a variety of protein-protein interactions and phosphorylations. The measurement of such interactions may be an alternative potential readout for rapid whole cell bioreporters, the concept of which has been demonstrated by fluorescence resonance energy transfer (FRET) sensors (see below).

The chemotaxis response at the molecular level consists of alternating patterns of phosphorylation, depending on the presence of attractants or repellants, which are transmitted to the flagellar motor. In absence of attractant, the methyl-accepting chemotaxis receptors (MCP) cause autophosphorylation of the associated kinase protein CheA, which is transmitted to phosphorylation of the response regulator protein CheY. The phosphorylated form of CheY (CheY~P) interacts with the FliM proteins of the flagellar motor and induces clockwise (CW) rotation, leading to tumbling of the cell. In absence of CheY~P interaction with the motor, the flagella rotate counter-clockwise (CCW), enabling the cell to swim more straight ("runs"). Steady dephosphorylation of CheY~P by the phosphatase CheZ maintains a constant ratio of CheY~P/CheY, keeping a basal ratio of alternating "run" and "tumble" events. Attractant binding to the receptor inhibits CheA kinase activity, which decreases the level of CheY~P. A lower CheY~P/CheY ratio on average leads to a decrease of tumbling and more straight runs [1, 2]. On the contrary, binding of a repellent activates CheA, leading to an increase of CheY~P/CheY ratio and an increase of tumble events. This increases the chance of the bacteria to change the swimming direction and escape the repellent source. On top of the phosphorylation cascade, the chemotaxis system has a "memory", which allows the cell to temporally compare the level of attractant through chemoreceptor methylation. Methylation of the chemoreceptor at specific amino acids is thought to increase its activity. The methylation state is a result of competition

between a methyltransferase named CheR and the methylesterase CheB. This feedback loop allows the cells to swim in direction of the highest concentration of the attractant by the re-establishment of the basal activity level of the receptor through time [3]. Thus, when cells are exposed to a sudden change of concentration of attractant or repellent, it leads to a rapid change in CheY~P level followed by a return to the initial state due to the methylation of the receptors [4].

It has been shown that the interaction between CheY~P and its phosphatase CheZ can be measured by fluorescence resonance energy transfer (FRET), from CFP (coupled to CheZ) to YFP (fused to CheY) [4]. The CheY-CheZ FRET signal is dynamic and dependent on the attractant concentration and flux, and is therefore an interesting candidate readout for development of biosensors. However, since FRET measurements are difficult to set up, we decided to explore a bimolecular fluorescence complementation (BiFC) approach using split-Gfp proteins [5, 6]. BiFC is a simple method to study protein-protein interaction. The principle is based on the fusion of non-fluorescent parts of a fluorescent protein to both proteins of interest that will reconstitute a functional fluorophore upon interaction [7, 8]. This technique is frequently used for *in vivo* subcellular protein interaction localization in eukaryotes [9-11] but has also been deployed in bacteria [5, 6, 12]. Although the generated split-Gfp is stable, a few studies have shown a dynamic signal in the cell, for example, fast generation of fluorescence upon protein interaction in neurons [10, 13] and also signal decay [11, 13].

To demonstrate the principle of BiFC on the chemotaxis pathway in *E. coli*, the N- and C-terminal parts of the Gfp protein, respectively, were fused to CheZ and CheY (Fig. 1A). The individual parts of split-Gfp are not fluorescent but when both parts are brought in close contact, they reform an intact Gfp and fluorescence can be measured. We expect that split-Gfp would yield specific foci where CheY~P and CheZ interact, which might increase or decrease in fluorescence upon ligand-stimulation of cells. Addition of attractant would reduce cellular levels of CheY~P, yielding fewer interactions with CheZ, and potentially lower fluorescence (Fig. 1B). Upon addition of repellent, the level of interaction between the proteins increases. Ligand-stimulation

would transiently change split-Gfp fluorescence until re-establishment of the basal level, similar to FRET measurements [4]. Finally, because we expected that the reconstituted split-Gfp would be relatively stable, we constructed a split-Gfp based on a Gfp-variant with a protease-tag. *E. coli* split-Gfp variants in combination with specific chemotaxis mutants were observed by epifluorescence microscopy to quantify fluorescence levels and localize split-Gfp foci in the cell. Fluorescence changes upon ligand stimulation were measured on cells incubated in microscope culture chambers.

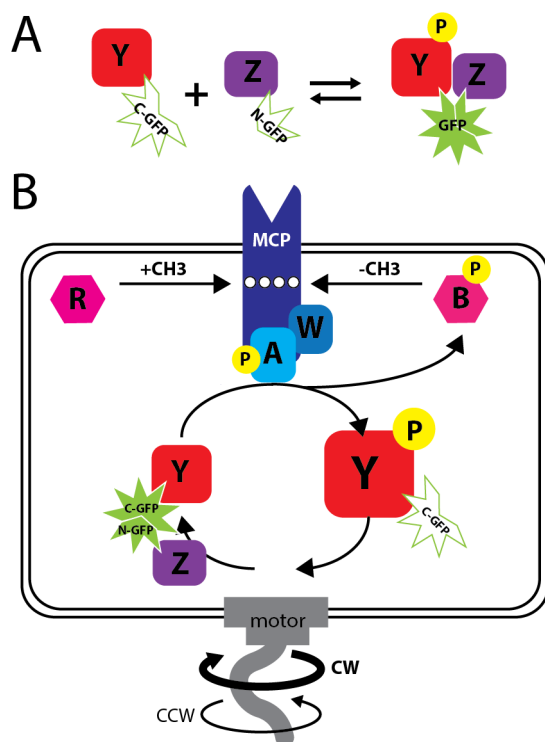


**Figure 1: Bimolecular fluorescence complementation in chemotaxis.** (A) Non-fluorescent C- and N-terminal parts of Gfp are, respectively, fused to CheY and CheZ. Functional fluorescent Gfp is reconstituted upon interaction between both proteins. (B) In absence of attractant the amount of CheY~P is higher, yielding more frequent interactions of CheY~P and CheZ, potentially leading to higher fluorescence emission. Attractant binding would lower the level of CheY~P, yielding less fluorescence.

## Results

### *Expression of split-GFP fused with CheY and CheZ chemotaxis proteins*

The chemotaxis protein CheY was fused with the C-terminal part of Gfp (amino acid: 158-238), and its phosphatase CheZ was fused with the complementary N-terminal part of Gfp (amino acid: 2-157). We hypothesized that the interaction between phosphorylated CheY (CheY~P) and CheZ would favor binding of N- and C-Gfp, inducing proper folding and Gfp fluorescence emission. Both fusion proteins were expressed in a single operon in *E. coli* under control of a constitutive synthetic promoter. Several promoters were tested, with an approximate difference in "strength":  $P_{AA} > P_{JJ} > P_{II} > P_{OO}$  (strains 4610, 4703, 4701 and 4702, respectively) [14]. Epifluorescence microscopy observations of individual *E. coli* cells expressing both fusion proteins from the four different promoters and incubated in absence of any attractant or repellent showed the presence of clear fluorescent foci (Fig. 2A-D). *E. coli* strains containing the empty plasmid vector (strain 4717) did not show any foci (Fig. 2E). Strains carrying plasmids in which frameshift mutations were introduced into either *cheY* (strain 4728) or *cheZ* (strain 4729), or both (strain 4743), causing premature stop codons, did not show any fluorescent foci either (Fig. 2F-H). We thus concluded that the foci were the genuine result of CheY<sub>-c</sub>Gfp/CheZ<sub>-N</sub>Gfp interactions and not the result of spontaneous split-Gfp interactions and subsequent multimerization.

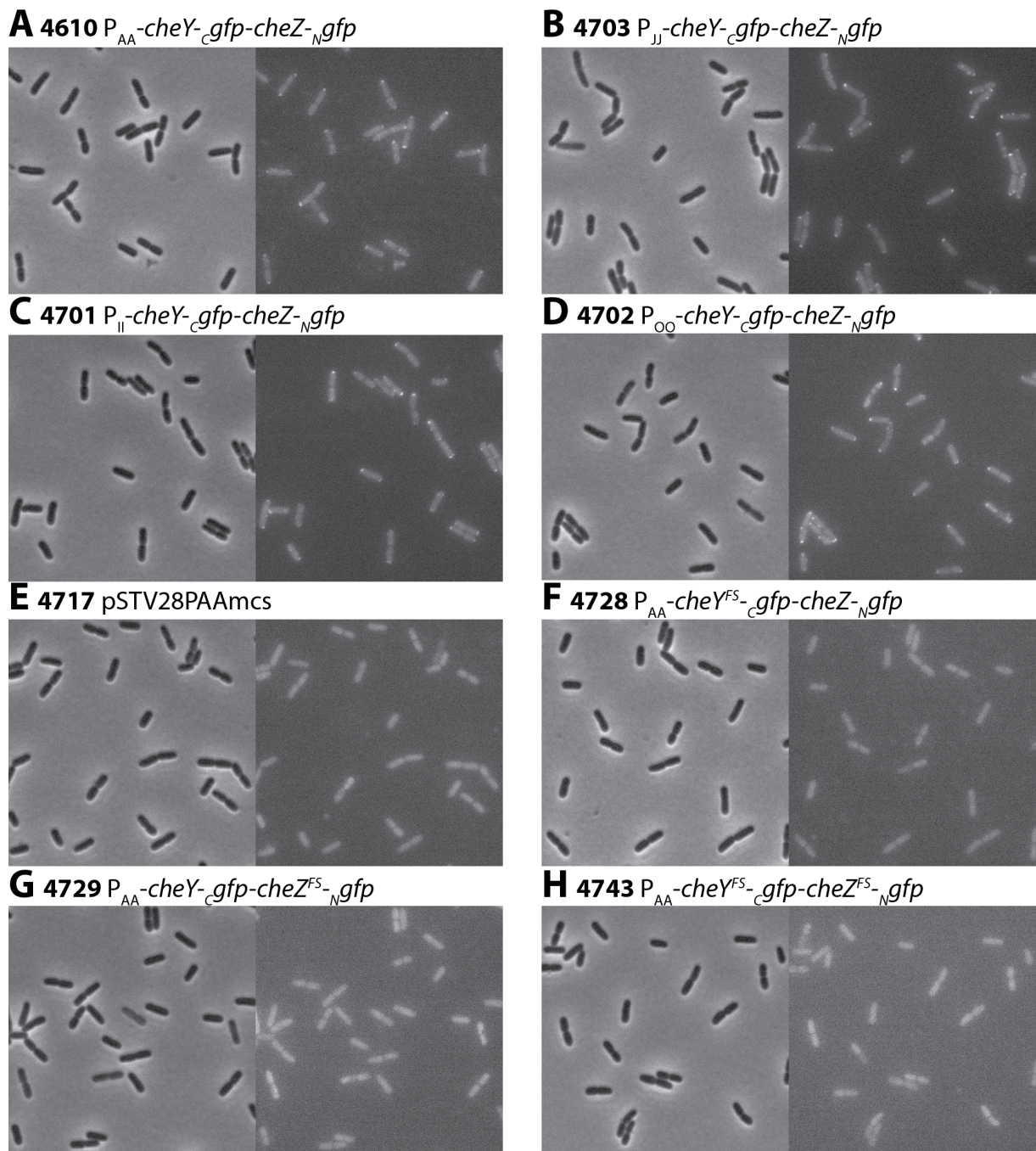


**Figure 2: Microscopy images of split-Gfp strains.** Phase contrast and GFP fluorescence images at 1000-fold magnification of *E. coli* expressing CheY or CheZ protein fusion with split-Gfp. **(A)–(D)** Strains carrying plasmids expressing *cheY*-*gfp*-*cheZ*-*gfp* under different promoter strengths ( $P_{AA}$ ,  $P_{JJ}$ ,  $P_{II}$ ,  $P_{OO}$ ). **(E)** *E. coli* transformed with the empty vector pSTV28PAAmcs. **(F)–(H)** *E. coli* with frameshift mutations in the plasmid-located genes *cheY* (4728), *cheZ* (4729) or in both *cheY* and *cheZ* (4743)

Global fluorescence intensities (i.e., averaged across the whole cell) of *E. coli* expressing *cheY-cgfp-cheZ-ngfp* were not significantly higher than in the control strains (e.g., 4717, 4728, 4729, 4743), except for *E. coli* strain 4610 expressing *cheY-cgfp-cheZ-ngfp* from the strongest promoter P<sub>AA</sub> (Fig. 3A). This strain also showed the highest level of fluorescence of foci only in comparison to *E. coli* expressing *cheY-cgfp-cheZ-ngfp* from P<sub>00</sub>, P<sub>JJ</sub> or P<sub>II</sub> (Fig. 3A). The number of foci varied between 0–5 per cell, depending on the expression strain (Fig. 3B). In particular *E. coli* strain 4610 (P<sub>AA</sub>) showed fewer foci than strains 4701–4703 (P<sub>II</sub>, P<sub>00</sub> and P<sub>JJ</sub>, respectively) and in most cells only a single (polar) focus was observed (Fig. 3B, C). The numbers of foci per cell were very similar for the strains 4703 (P<sub>JJ</sub>), 4701 (P<sub>II</sub>) and 4702 (P<sub>00</sub>, Fig. 3B). In all strains expressing both fusion proteins simultaneously, the majority of foci localized at the cell poles, and less so at various positions along the cell (Fig. 3C). The intensity of the foci was variable with a maximum of 3.5 times higher than the cell background, suggesting different accumulation or turnover of the fusion proteins at those sites. Strains that did not express the fusion proteins or truncated versions showed no foci, confirming that the foci were the result of specific CheY-CheZ interactions (Fig. 3A, B).

Because of the higher foci and cellular fluorescence intensity, and lower number of foci per cell in *E. coli* strain 4610 expressing both fusion proteins under the strongest promoter P<sub>AA</sub>, we decided to select the P<sub>JJ</sub> promoter construct for further investigations. This strain has a stronger promoter than P<sub>II</sub> and P<sub>00</sub> without showing significant phenotypic differences in foci or their fluorescence (Fig. 3B, C).



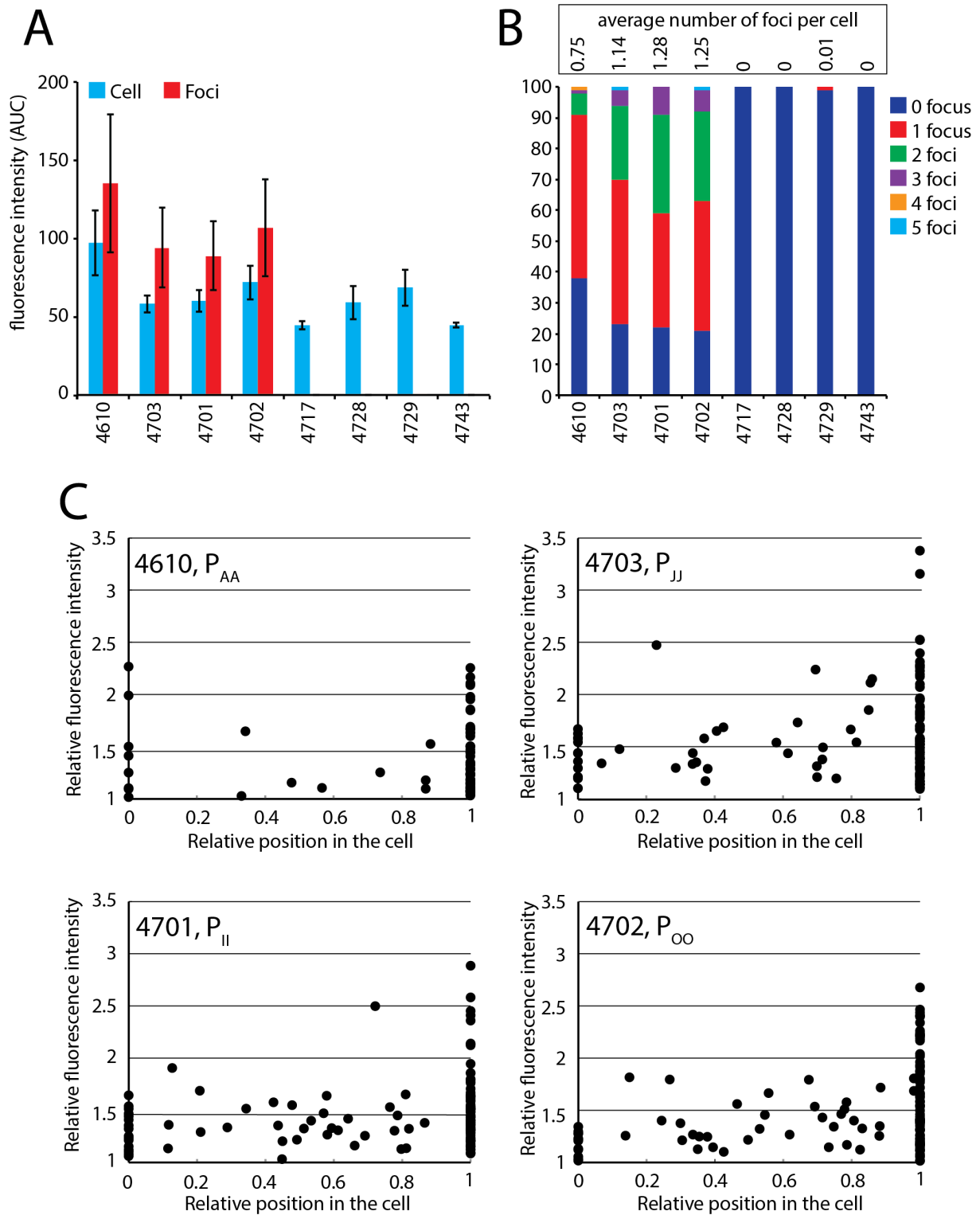


**Figure 3: Fluorescent foci quantification. (A)** Average of fluorescence intensity across the whole cell and in individual foci. **(B)** Distribution and average number of foci per cell for all strains. **(C)** Foci localization and their relative fluorescence intensity along individual cells. The relative fluorescence intensity was calculated by dividing the fluorescence intensity of an

individual focus by the average fluorescence of its cell. Localization was normalized by the length of the individual cell (0 and 1 correspond to cell poles). Strain numbers correspond to Table 2.

### *Functionality of the split-GFP fusion proteins*

In order to test whether the split-GFP chemotaxis fusion proteins were functional, we cloned pCR09 ( $P_{J1}-cheY-cgfp-CheZ-ngfp$ ) into a  $\Delta cheYcheZ$  deletion mutant. In this *E. coli* background, the chemotaxis regulators will only be expressed as split-GFP fusion protein. Chemotaxis of *E. coli* 5395 (pCR09 in  $\Delta cheYcheZ$ ) in agarose plug assays with 100  $\mu$ M serine as source was detectable and similar to MG1655 containing pCR09, but less strong in comparison to *E. coli* 4498 (MG1655 wild-type, Fig. 4A). As expected, no chemotaxis to serine was detected in *E. coli* 5391 ( $\Delta cheYcheZ$ , Fig. 4A). This suggests that the fusion proteins are at least partially functional to control chemotaxis. The average number of foci in *E. coli* 5393 (pCR09 in  $\Delta cheYcheZ$ ) in absence of chemotactic stimulation was statistically significantly higher than in strain 4703 (pCR09 in MG1655;  $p=0.00059$ , pair-wise t-test; Fig. 4B, C). The higher foci number is consistent with the idea that in the  $\Delta cheYcheZ$  mutant split-GFP fusion proteins exclusively react among each other (creating foci), whereas in the wild-type *E. coli* interactions of split-GFP-versions with native CheY and CheZ protein result in non-fluorescent complexes.

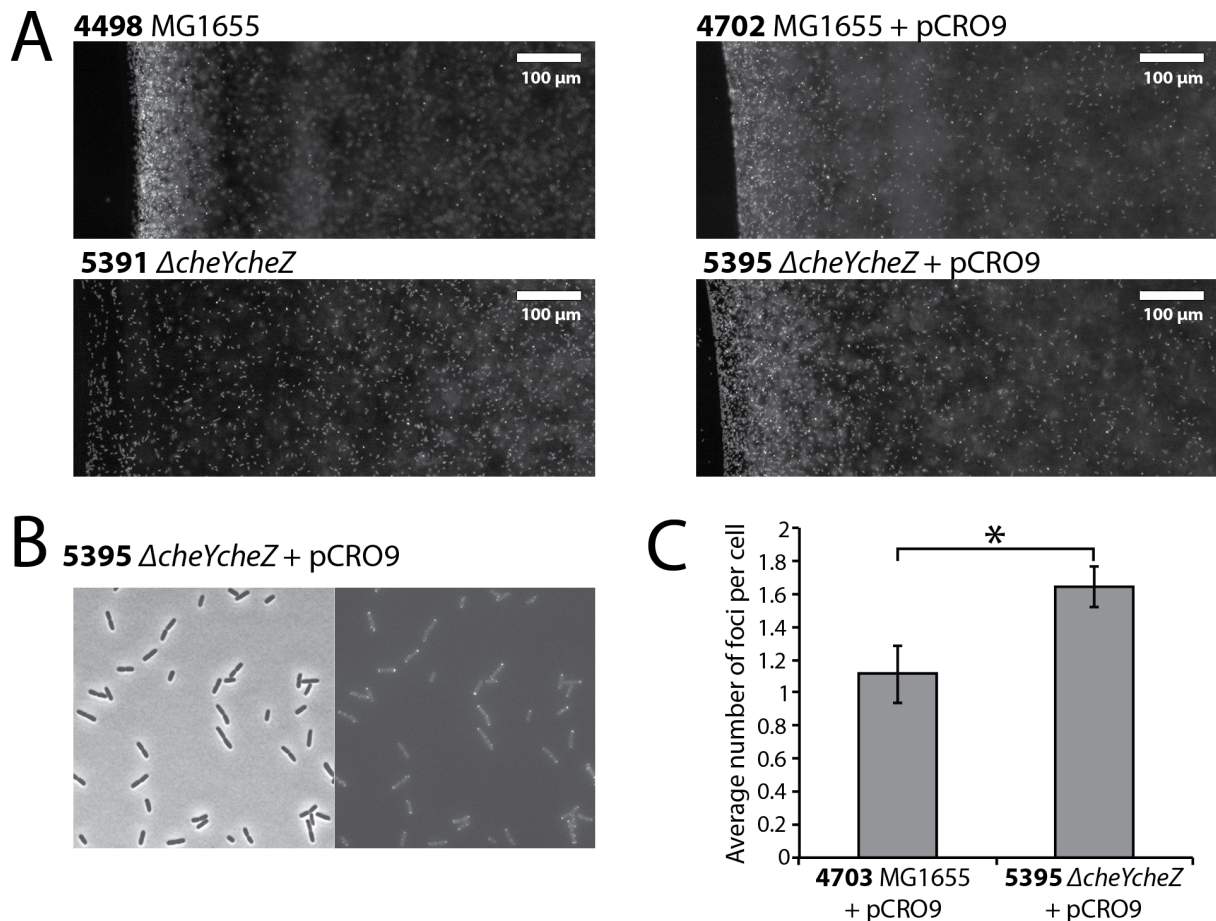


**Figure 4: Functionality of CheY-cGfp CheZ-NGfp fusion proteins. (A)** Agarose plug chemotaxis test towards 100  $\mu$ M serine of *E. coli* MG1655, *E. coli*  $\Delta cheYcheZ$  or *E. coli*  $\Delta cheYcheZ$  complemented with plasmid pCRO9 expressing *cheY-cgfp-cheZ-ngfp* from  $P_{J1}$ . Note the dark source edge at the left of the images. Cells imaged at 100-fold magnification in phase-contrast. **(B)** Phase-contrast and Gfp fluorescence images at 1000-fold magnification of *E. coli* strain 5395 ( $\Delta cheYcheZ$  + pCRO9). Note the cellular foci in the Gfp-channel. **(C)** Average number of foci per cell in *E. coli* MG1655 (pCRO9) and in strain 5395 ( $\Delta cheYcheZ$  + pCRO9). \*,  $p=0.00059$ ; pair-wise, two-tailed t-test.

#### *Split-GFP expression in chemotaxis deletion mutants*

In order to confirm that the foci detected were a consequence of interaction between CheY~P and CheZ, we introduced the  $P_{J1}$ -*cheY-cgfp-CheZ-ngfp* construct into an *E. coli* mutant

lacking the gene encoding the CheA kinase. Deletion of CheA abolishes phosphorylation of CheY and of the CheY-cGfp fusion protein, which should cancel interactions with the CheZ phosphatase. *E. coli*  $\Delta cheA$  (pCRO9) cells did not show any foci, which is in agreement with our hypothesis and strongly suggests that the observed foci in e.g., *E. coli* strain 4703 or 5395 are the result of physical interaction between phosphorylated CheY-cGfp and CheZ-NGfp (Fig. 5A).

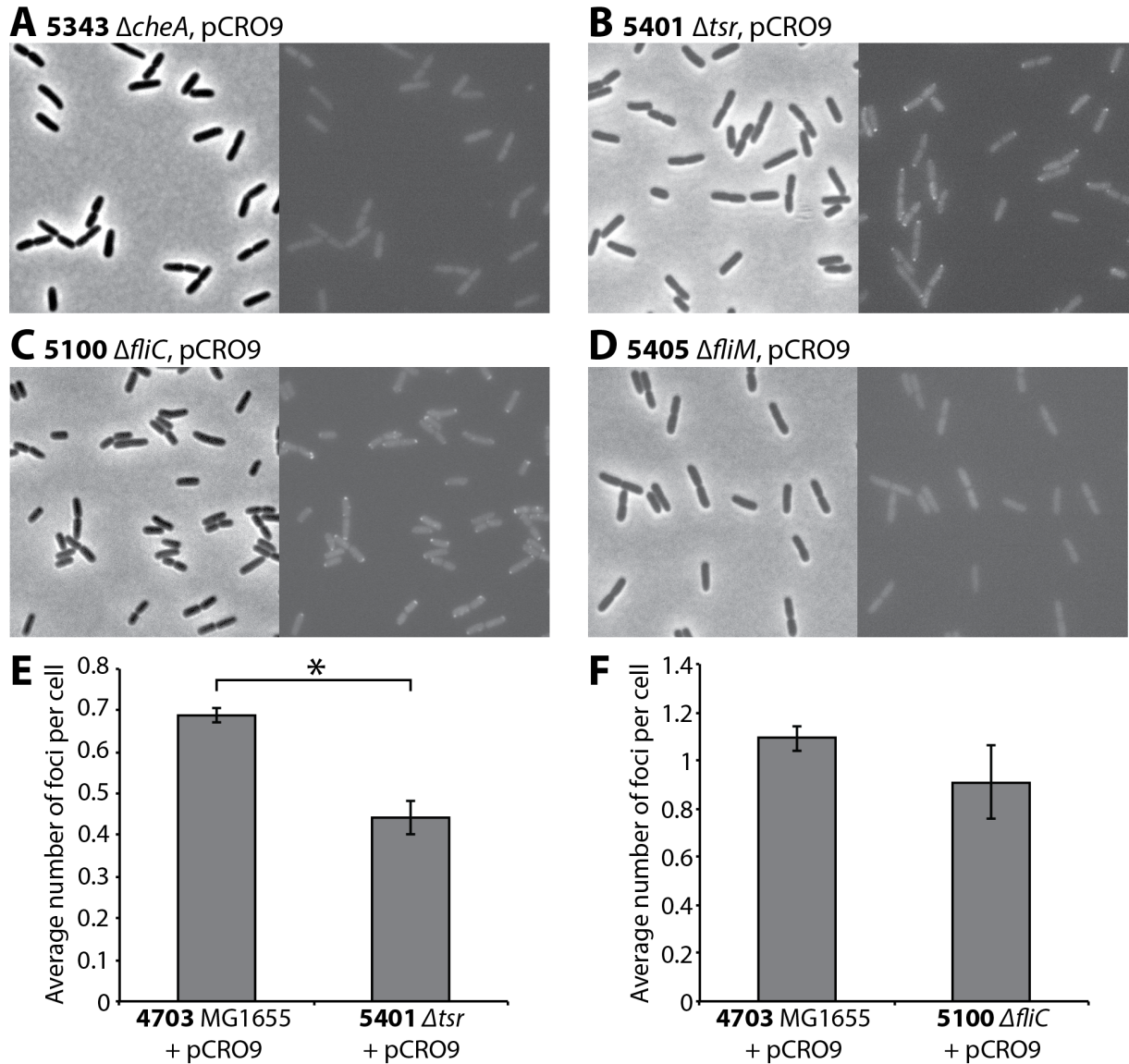


**Figure 5: Effect of chemotaxis protein deletions on foci formation from CheY-cGfp CheZ-NGfp fusion proteins. (A)–(D)** Phase contrast and Gfp fluorescence images at 1000-fold magnification of *E. coli* with plasmid pCRO9 expressing *cheY-cgfp-cheZ-ngfp* from P<sub>JI</sub> in  $\Delta cheA$ ,  $\Delta tsr$ ,  $\Delta fliC$  or  $\Delta fliM$  background, respectively. Note the total absence of foci in  $\Delta cheA$  and  $\Delta fliM$

backgrounds. **(E)–(F)** Average number of foci per cell in *E. coli* 4703 (MG1655 + pCRO9) in comparison to strain 5401 ( $\Delta tsr$  + pCRO9), or to 5100 ( $\Delta fliC$  + pCRO9), respectively (independent experiments of pairs conducted simultaneously). \*,  $p=0.023$ , pair-wise two-tailed t-test.

Since CheY~P–CheZ-split-Gfp fluorescence mostly appeared in clearly localized foci in the cell (Fig. 2), this suggested they were the result of an additional interaction of either CheY~P or CheZ with either chemoreceptors or motors, which have precise localization. CheY/CheY~P is known to interact both with the chemoreceptors and the flagellar motors. In an *E. coli*  $\Delta tsr$  mutant carrying pCRO9, which lacks the chemoreceptor for serine, fluorescent foci were still visible (Fig. 5B), but the average number of foci per cell was statistically significantly reduced compared to wild-type *E. coli* strain 4703 with pCRO9 ( $p=0.023$ , pair-wise t-test; Fig. 5E). This result showed that the lack of the major *E. coli* chemoreceptor interferes with the formation of the foci, which suggest that at least partially, they are formed at the chemoreceptor position. In contrast, the deletion of *fliC* coding for the flagellin did not impact the average number of foci per cell compared to the wild-type control (Fig. 5C, F). Flagellin is the major constituent of the flagellar filament, which does not interact with the intracellular chemotaxis regulator proteins. However, when we deleted the *fliM* gene encoding the motor protein with which CheY~P interacts to invert flagellar rotation, cellular foci could no longer be detected (Fig. 5D). This suggests that FliM motor proteins stabilize the formation of the foci and that CheY-cGfp and CheZ-NGfp interact at the position of the flagellar motors.

Given that the  $\Delta fliM$  mutant still expresses CheY-cGfp and CheZ-NGfp, one can wonder whether both proteins still interact in the cytoplasm but without proper localization. We compared hereto the cellular fluorescence of the  $\Delta fliM$  with that of the  $\Delta cheA$  mutant. The *E. coli*  $\Delta cheA$  mutant cannot phosphorylate CheY, therefore, CheY-cGfp and CheZ-NGfp do not interact except by chance, and no fluorescence is produced. Cellular fluorescence of  $\Delta fliM$  and  $\Delta cheA$

mutants that express both fusion proteins is slightly lower than in *E. coli* MG1655, which may be explained by the lack of fluorescent foci (Fig. 6, dark bars). No difference between both mutants was detectable, although the fluorescence background of *E. coli*  $\Delta cheA$  without pCRO9 was higher than the background level of *E. coli* MG1655 and *E. coli*  $\Delta fliM$  without pCRO9 (Fig. 6, white bars). The absence of foci and the equal fluorescence intensity with *E. coli*  $\Delta cheA$  suggest that CheY-cGfp and CheZ-NGfp do not interact in the  $\Delta fliM$  mutant.

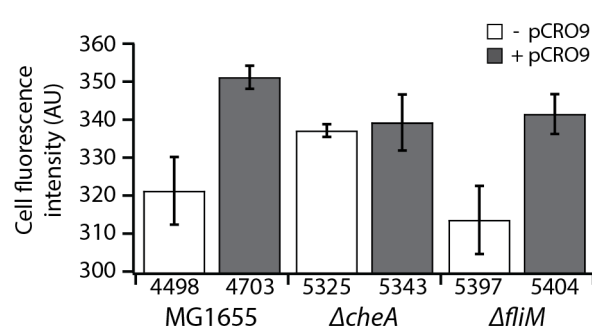


**Figure 6: Comparison between  $\Delta fliM$  and  $\Delta cheA$  strain expressing CheY-cGfp CheZ-NGfp.** Cellular fluorescence intensity of *E. coli* MG1655,  $\Delta cheA$  and  $\Delta fliM$  strains expressing or not the fusion proteins from pCRO9 plasmid (+/- pCRO9).

### Induction of the system by addition of repellent

Finally, we were interested to test whether the split-GFP system could show a dynamic response in cells stimulated by chemotaxis ligands. We hypothesized that addition of a repellent, such as nickel, might cause an increase of split-Gfp fluorescence, and addition of attractant a decrease, compared to the buffer only control.

In order to create conditions of stimulating chemotaxis response but keep the possibility to measure foci fluorescence at individual cell level, we immobilized *E. coli*  $\Delta cheYcheZ$  cells expressing both fusion proteins on the bottom of poly-L-lysine coated wells on top of a microscopy slide and immersed in buffer. Fluorescence of foci was recorded by microscopy imaging every minute, while focusing on cells attached to the slide, before and after addition of ligand. Fluorescence response curves of individual foci were rather dissimilar but mostly decreased over time, as a consequence of photobleaching (Fig. 7A and C). Individual response

curves from foci in *E. coli* cells exposed to buffer were fitted with a decay function  $f(x) = 1 / (kx + (1/A0))$  from which the average  $k$ -parameter (slope) value was calculated, which we assume to represent the effect of photobleaching (Fig. 7B). Individual foci response curves from *E. coli* cells exposed to 100  $\mu\text{M}$  nickel were similarly fitted (Fig. 7D), and the number of response curves with slopes statistically significantly smaller than the average from the no-exposure controls (i.e.,  $k + SD_k < AVE_{k,buffer} - SD_{k,buffer}$ ) was scored. These would correspond to a curve with a slower decrease than caused by photobleaching, possibly as a result of faster renewed CheY-phosphorylation and formation of split-Gfp.

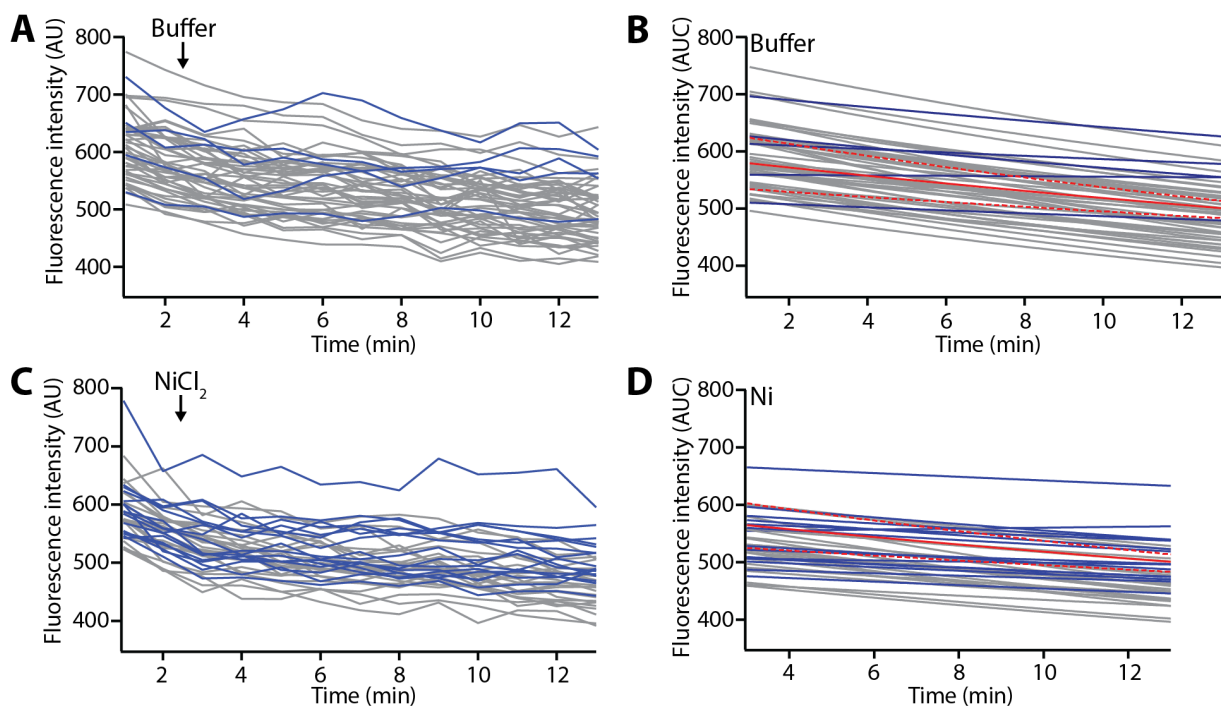


**Figure 7: Foci fluorescence changes after ligand exposure.** (A) Foci fluorescence of *E. coli*  $\Delta cheYZ$  (pCR09) in motility buffer and (C) exposed to 100  $\mu\text{M}$   $\text{NiCl}_2$  after time 2 min. Fitting curves for foci fluorescence decays after addition of (B) motility buffer or (D)  $\text{NiCl}_2$ . In blue are the response curves with a  $k$  parameter statistically significantly smaller than the averaged  $k$  parameter of all decay curves under buffer inductions. Red lines display the average fitting curves  $\pm$  calculated standard deviation (red dashed lines). Cells were imaged every 1 min at

200 ms exposure, twice in motility buffer, and ten times after ligand or buffer addition (small vertical arrow).

The proportion of foci decay curves with a slower decay and significantly different from the average under motility buffer conditions, was higher when cells were exposed to nickel than to buffer ( $p=0.0072$  using a Kruskal-Wallis test, ANOVA, Fig. 8A). In contrast, no significant effect was observed when adding 100  $\mu\text{M}$  serine (Fig. 8A). For the serine exposure, we expected to observe faster fluorescence decay than after exposure to motility buffer. However, the proportion of curves with a faster decay from the average under motility buffer conditions was not significantly different, neither with 100  $\mu\text{M}$  nickel nor serine (Fig. 8B).

These results suggest that it is possible to use the split-GFP system as a dynamic readout for repulsion response, although the response of individual cells is highly heterogeneous and the difference between conditions is small.

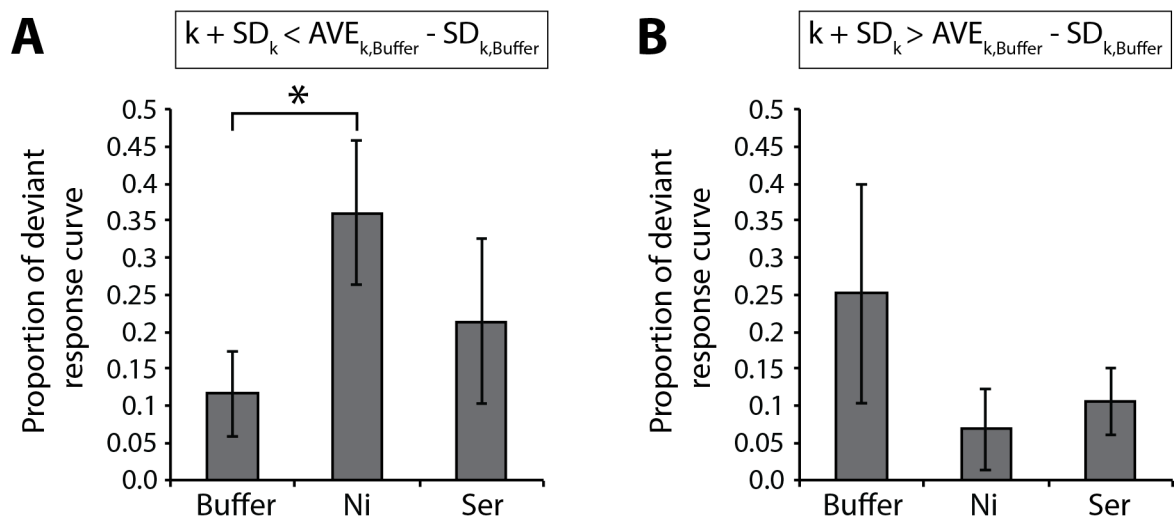


**Figure 8: Split-GFP system is inducible with nickel. (A)** Proportion of deviant response curves of foci fluorescence with a lower slope decay ( $k$  parameter) in *E. coli* cells exposed to 100  $\mu\text{M}$   $\text{NiCl}_2$  (Ni) or to 100  $\mu\text{M}$  serine (Ser) compared to buffer alone **(B)** Proportion of deviant



response curves of foci fluorescence with a higher k parameter in *E. coli* cells exposed to 100  $\mu\text{M}$   $\text{NiCl}_2$  (Ni) or to 100  $\mu\text{M}$  serine (Ser) compared to buffer alone.

## Discussion

In this chapter we envisioned to measure changes in interactions between CheY~P and CheZ as a proxy of ligand binding to the chemoreceptors in *E. coli*. CheZ is the phosphatase that dephosphorylates CheY and their interaction frequency is dependent on the intracellular concentration of phosphorylated CheY. The level of CheY~P is modified by the binding of attractant or repellent to the receptors: attractants induce a decrease of the concentration of CheY~P and repellents induce an increase. A measurement of this interaction would thus characterize temporal chemotaxis pathway activation. In contrast to previous studies using FRET, we used the approach of bimolecular fluorescence complementation by fusing split parts of the Gfp to CheY and CheZ.

We demonstrated that the fusion proteins were functionally complementing chemotaxis in an *E. coli*  $\Delta cheYZ$  deletion mutant background (Fig. 4). Comparison of chemo-attraction of *E. coli* expressing CheY<sub>-c</sub>Gfp and CheZ<sub>-N</sub>Gfp showed weaker chemotaxis than *E. coli* MG1655 WT, both in presence or absence of native CheY/CheZ. This suggests that the fusion proteins slightly interfere with the native proteins and impair a bit chemotaxis (Fig. 4). Nevertheless, we judged the functionality and complementation sufficient for studying CheY~P–CheZ interactions.

The expression of split-Gfp fused to CheY and CheZ under the control of weak constitutive promoters showed the presence of fluorescent foci mostly localized at the cell pole (Fig. 2 and 3). Do these foci reveal the genuine direct interaction between CheY~P and CheZ? To answer this question we deleted the CheA kinase that phosphorylates CheY and this deletion abolished the presence of foci (Fig. 5). This demonstrated that the foci are the result of specific interactions between CheY~P and CheZ, since without phosphorylation of CheY, CheY and CheZ do not interact and foci do not appear.

Since it would be conceivable that CheY~P and CheZ interact in the cytoplasm without formation of specific foci, we studied the dependence of foci formation and localization on the major chemoreceptor Tsr and the motor protein FliM, which interacts with CheY~P. No foci

were detected in *E. coli*  $\Delta fliM$ , which suggests that motor proteins stabilize the interaction and that CheY-cGfp and CheZ-NGfp accumulate at the position of flagellar motors (Fig. 5). This result is in contrast to current literature that poses that both CheY and CheZ proteins localize at the receptor at the cell pole [15]. Mathematical modeling demonstrated that the polar localization of CheZ is crucial to obtain a uniform concentration of CheY~P in the cell to interact similarly with the peritrichous flagella [16]. Due to CheZ localization, both proteins are supposed to interact at the receptor near the cell pole [17, 18]. Expression of CheY-cGfp and CheZ-NGfp in a  $\Delta tsr$  *E. coli* mutant background also showed a decrease in the average number of foci per cell, but did not abolish foci formation altogether, like in *E. coli*  $\Delta fliM$ . This suggests that Tsr can also partially stabilize CheY~P-CheZ interaction (Fig. 5). Hence, we conclude that the interaction can take place at the motor but also at the receptor. The latter is consistent with theory because CheY and CheZ are localized at the receptor, as shown by Sourjik and Berg [15], but CheY~P, once phosphorylated by CheA, has to diffuse to the motor to induce inversion of flagellar rotation and may therefore further interact with CheZ at the motor. Another hypothesis could be that the deletion of *fliM* induces an inhibition of the expression of other chemotaxis proteins, such as CheA or the receptors.

Not unexpectedly, the formed CheY~P-CheZ-split-GFP foci were stable in the cell. By photobleaching cells in motility buffer in comparison to motility buffer with addition of nickel ions (a strong repellent), we could see some trends that Gfp photodecay was counteracted by renewed foci formation (Fig. 7, 8). However, this response was quite variable among individual cells and was absent in cells exposed to serine. This might be the result of the split-Gfp stability, as foci would not dissociate faster upon addition of attractant. Indeed, although most reports indicate split-fluorescent proteins to be stable and irreversible [9], some publications have shown a decay of signal using BiFC in eukaryote cells [11, 13]. We tried to destabilize Gfp by adding different protease tags with a range of half-life times (LVA:  $t_{1/2}$  =40 min, AAV:  $t_{1/2}$  =60 min, ASV:  $t_{1/2}$  =110 min) [19], but, unfortunately, in such *E. coli* cells no or only sporadic foci were detected (data not shown).

We do acknowledge that the measurements of split-Gfp may be further improved by changing the experimental setup. In order to detect fluorescent foci, the cells have to be immobilized to allow proper focusing and imaging. On the other hand, we expect that it might be more physiologically appropriate if the flagella can turn freely, which we do not know for cells placed on agarose-coated slides. A further problem is the addition of ligand to stimulate changing chemotactic behavior. Adding a ligand into a solution with bacteria attached to the bottom of the wells would cause (i) some unknown delay as a result of mixing and (ii) a transient reaction of cells until they adapt to the new concentration due to methylation of the chemoreceptors. This setup permitted to detect changes in the foci fluorescence upon addition of the nickel repellent ions. In contrast, if one could create a ligand gradient as in the agarose source assays, individual cells will react during a longer time because they face a continuous concentration increase towards the source. We also tried to image fluorescence changes in foci in individual *E. coli* cells spotted on agarose exposed to a gradient of inducer, but this was poorly reproducible (data not shown).

Split-Gfp approaches have enabled the detection of specific protein-protein interactions in cells, and, as we demonstrated here, of CheY~P-CheZ in *E. coli*. The stability of the split-Gfp makes it not very suitable for dynamic measurements, although several research groups have attempted to engineer less stable variants. For example, a tripartite GFP was described recently which shows faster association and minimized non-specific protein aggregation [20]. However, also the tripartite GFP shows irreversible association. The use of dimerization-dependent fluorescent proteins (ddFP) could be an interesting alternative. It consists of two weakly or non-fluorescent monomers of fluorescent protein that become fluorescent upon interactions [21, 22]. The advantage is the reversibility of the system, which can react in a timescale of seconds [22]. But the monomers are bigger peptides that could affect the functionality of the proteins of interest. Finally another alternative might be the use of bioluminescence resonance energy transfer (BRET), which may be achieved by fusing a luciferase and the Yfp to CheY and CheZ, respectively (or vice-versa) [23, 24]. Similar to FRET, the light emitted by the luciferase can

excite the Yfp protein if they are in close range. BRET may have the advantage of not requiring external light to excite the Yfp, which would be convenient from a biosensing perspective.

To conclude, we established a bimolecular fluorescence complementation assay with CheY and CheZ. Interaction between the two proteins was revealed through the presence of fluorescent foci in *E. coli* cells. This system can be used to study the response to the addition of a repellent but it was highly heterogeneous and the interaction was not very dynamic, probably because the split Gfp is very stable once it is formed.

## Material and methods

### *Bacterial strains and culture conditions*

A specific motile strain of *Escherichia coli* MG1655, obtained from the *E. coli* Genetic stock center, Yale (CGSC#8237) was used as host strain for the plasmids constructed in this study. The strains were grown at 37°C with 180 rpm shaking in M9-Glc (see chapter 2). The medium was supplemented with chloramphenicol 20 µg ml<sup>-1</sup> for strains containing pSTV-based plasmids (Table 2).

### *Cloning of the split-GFP*

The chemotaxis regulator protein CheY was fused (at its C-terminal end) with the C-terminal part of Gfp and its phosphatase CheZ was fused (at its C-terminal end) with the complementary N-terminal part of Gfp. First, the gene coding for *cheY* (without its stop codon) was amplified by PCR from *E. coli* MG1655 genomic DNA using primers 130719 and 130720, respectively elongated with BamHI and AatI restriction sites (Table 1). The 3'-end of *gfp* corresponding to amino acids 158–238 was amplified by PCR from plasmid pPROBE [25] using primer 130724 containing an AatI restriction site and a sequence for a seven-amino-acid linker (GTSGGSG), and primer 130724, elongated with SpeI and HindIII restriction sites (Table 1). The inserts *cheY* and *cgfp* were, respectively, digested with BamHI and AatI or with AatI and SpeI and were cloned under the control of the synthetic promoter P<sub>AA</sub> in the linearized pSTV28P<sub>AA</sub>mcs backbone [26].

In a second cloning step *cheZ* (without stop codon) was amplified by PCR from *E. coli* MG1655 genomic DNA using primer 130721 elongated with an SpeI restriction site and primer 130722 containing an XhoI restriction site and a sequence encoding an eight-amino-acid linker (GGSGGSR). The 5'-end of *gfp* corresponding to amino acids 2–157 was amplified from plasmid pPROBE using primers 130726 and 130723, elongated with XhoI and HindIII restriction sites, respectively. Both PCR fragments were then inserted downstream of the *cheY-Cgfp* hybrid gene

within the same operon (i.e, under  $P_{AA}$  control). A variety of derivative plasmids was created, in which  $P_{AA}$  was replaced by different weaker synthetic promoters named  $P_{JJ}$ ,  $P_{II}$ , and  $P_{OO}$  in order to tune the level of expression of the fusion proteins [14]. Synthesized promoter sequences were flanked by EcoRI and BamHI restriction sites, which allows easy exchange [27].

As negative controls we introduced frameshift mutations in *cheY* and *cheZ*, by digestion with the restriction enzymes Sall and MutI, respectively, filling in and religating.

*E. coli* deletion mutants were constructed by double recombination methods [28]. Gene flanking regions were amplified by PCR and cloned into the pEMG suicide vector [28] and transformed into *E. coli* MG1655. Single recombinants were recovered by selection on Km-resistance and were examined by PCR. If correct, they were transformed with the plasmid pSW-I that contains a 3-methylbenzoate inducible SclI restriction enzyme [28]. Induction of this restriction enzyme forces the second recombination. Kanamycin-sensitive colonies were examined by PCR for proper deletion. Finally, pSW-I was cured by consecutive passage in culture without antibiotic selection pressure.

### *Epifluorescence microscopy*

Overnight cultures of *E. coli* strains in M9-Glc supplemented with 20  $\mu\text{g ml}^{-1}$  of chloramphenicol were 100-times diluted in fresh medium and incubated at 37°C with shaking until they reached an optical density at 600 nm ( $OD_{600}$ ) of 0.5–0.7. From these exponential cultures, 600  $\mu\text{l}$  were centrifuged at  $2,400 \times g$  for 5 min, washed twice with 1 ml of motility buffer (see chapter 2) and finally concentrated in 50  $\mu\text{l}$  of motility buffer. A drop of 7  $\mu\text{l}$  of cell suspension was spotted on 1% agarose (in motility buffer) coated microscopy slides and then covered with a regular 0.17-mm thick glass coverslip. Cells were imaged at an exposure time of 10 ms (phase-contrast) or 1 s (Gfp) with a DFC 350 FX R2 Leica camera mounted on an inverted DMI 4000 Leica microscope using a 100 $\times$  Plan Apochromat oil objective. The images were analyzed using the open-access software *MicrobeJ*, which allows automatic cell segmentation and foci detection ([www.microbeJ.com](http://www.microbeJ.com)) [29].

### *Time-lapse microscopy*

Overnight cultures of *E. coli* strain 5395 ( $\Delta cheYcheZ$  + pCR09) in M9-Glc supplemented with 20  $\mu\text{g ml}^{-1}$  of chloramphenicol were 100 times diluted in fresh medium and incubated at 37°C with shaking until they reached an  $\text{OD}_{600}$  of 0.5–0.7. From these exponential cultures, 1 ml was centrifuged at  $2,400 \times g$  for 5 min, washed twice with 1 ml of motility buffer and resuspended in 600  $\mu\text{l}$  of motility buffer. Cells were adhered to the bottom of the wells of a CELLview™ Slide with 10 wells (Greiner Bio-One GmbH, Germany) coated with poly-L-lysine. For well coating, 100  $\mu\text{l}$  of 0.01 % poly-L-lysine solution (Sigma) was incubated for 5 min at room temperature in the wells, decanted and wells were dried overnight. Wells were filled with 100  $\mu\text{l}$  of cell suspension and incubated at room temperature for 30 min. Liquid was discarded and wells were washed 5 times with 400  $\mu\text{l}$  of motility buffer to remove any non-adhering cells. Finally, the wells were loaded with 200  $\mu\text{l}$  of motility buffer. Bacteria were imaged with a Nikon Eclipse Ti-E inverted microscope, equipped with an ORCA-flash4.0 camera (Hamamatsu) and a Plan Apo  $\lambda$  100 $\times$ 1.45 oil objective (Nikon). Seven regions of the wells were imaged automatically with one minute intervals in Gfp (200 ms exposure) and phase contrast (10 ms exposure) with lamp power at 100 %. Baseline Gfp fluorescence was imaged at time=0 and 1 min, after which 10  $\mu\text{l}$  of inducer (2 mM of  $\text{NiCl}_2$  or Serine for a final concentration of 100  $\mu\text{M}$  or motility buffer as control) was pipetted in the wells and cells were imaged for a further 10 min (at 1 min intervals). Images were recorded using Micro-Manager 1.4 (<http://www.micro-manager.org/>). Ellipses of  $8 \times 8$  pixels were placed on the foci using MetaMorph (Series 7.5, MDS, Analytical Technologies) and mean fluorescence intensities in the ellipses were extracted at all time points using an in-house written Matlab (R2015b) script (developed by Serge Pelet, University of Lausanne).



*Time-lapse data analysis*

Baseline fluorescence decay of foci in individual cells incubated with motility buffer only was fitted with a general second-order decay function using Igor Pro (WaveMetrics, Inc. Oregon 97035, USA)

$$f(x) = \frac{1}{(kx + (\frac{1}{A_0}))}$$

with  $k$  being the rate constant and  $A_0$  the initial fluorescence. The average ( $AVE_{k,buffer}$ ) and standard deviation ( $SD_{k,buffer}$ ) was calculated from all individual cell traces in motility buffer.

Individual fluorescence responses of the foci of experiments with induction of nickel or serine were fitted with the same decay function (between time points 2 – 12 min), obtaining  $k_{Ni\ or\ Ser}$  and its fitting deviation  $SD_{k,Ni\ or\ Ser}$ .

The number of deviant individual response curves was then counted for each condition, motility buffer only nickel or serine, if  $k_{Ni\ or\ Ser} + SD_{k,Ni\ or\ Ser} < AVE_{k,buffer} - SD_{k,buffer}$ , which corresponds to a fitting curve that decreases less than the expected baseline second-order decay or if  $k_{Ni\ or\ Ser} + SD_{k,Ni\ or\ Ser} > AVE_{k,buffer} - SD_{k,buffer}$ , which corresponds to a fitting curve that decreases more than the expected baseline second-order decay. The proportions of individual deviant curves in a simultaneous sampling series between buffer incubation and nickel or serine induction were then compared using a Kruskal-Wallis test (ANOVA).

*Agarose plug chemotaxis assay*

Overnight cultures of the strains in M9-Glc supplemented with 20  $\mu\text{g ml}^{-1}$  of chloramphenicol were 100 times diluted in fresh medium and incubated at 37°C with shaking until they reached an  $OD_{600}$  of 0.5–0.7. From these exponential cultures, 1 ml was centrifuged at  $2,400 \times g$  for 5 min, washed twice with 1 ml of motility buffer and finally resuspended in 1 ml of motility buffer.

On a microscopy glass slide (1 mm thickness, RS France, Milian), two squared coverslips ( $24 \times 24$  mm, 0.13-0.17 mm thickness, MGF) were deposited on the edge of the slide. A 5  $\mu\text{l}$  drop

of 2% agarose supplemented with 100  $\mu$ M of serine (kept at 55°C) was pipetted on the slide between the coverslips. A large coverslip (25  $\times$  50 mm, Menzel-Glaser) was quickly deposited on top of the agarose plug. After drying during 5 min, 150  $\mu$ l of cell suspension were pipetted at the edge between the large coverslip and the glass slide. Bacterial chemotaxis was recorded after 30 min by light microscopy closed to the source.

**Table 1: Primer list**

Primer collection n°	Sequence (5' - 3')
130719	ccggacaggggatccgtatttaaatacaggagtgtgaaatggc
130720	tagtcgcatgacgtcccatgccagtttctcaaag
130721	gacttcactagtgaggatgcgactatgatgcaaccatc
130722	cttactcctcgagccagagccagagccaccaaatccaagactatccaacaaatcg
130723	actgtaagcttattgtttgtctgcatgatgtatacattg
130724	ctggcatggggacgtcgggtggaagcggtaaagaatggaatcaaagttaacttc
130725	ggtacgggaagcttatcgactagttattgtatagttcatccatgcatgt
130726	ggctctggctcgaggagtaaaggagaagaacttttactgg

Note: restriction sites and linker sequences are respectively highlighted in italic and in bold

**Table 2: Strain list**

Strain n°	Host	Plasmid	Relevant characteristics	Source of reference
4498	<i>E. coli</i> MG1655		Verified for motility	<i>E. coli</i> Genetic Center, Yale (CGSC#8237)
4717	<i>E. coli</i> MG1655	pSTV28P <sub>AA</sub> mcs	Plasmid backbone containing P <sub>AA</sub> promoter	[26]
1421	<i>E. coli</i> DH5 $\alpha$	pPROBE	<i>gfp</i> gene source	[25]
4610	<i>E. coli</i> MG1655	pCRO2	Plasmid containing P <sub>AA</sub> - <i>cheY-Cgfp-cheZ-Ngfp</i>	This study
4701	<i>E. coli</i> MG1655	pCRO7	Plasmid containing P <sub>II</sub> - <i>cheY-Cgfp-cheZ-Ngfp</i>	This study
4702	<i>E. coli</i> MG1655	pCRO8	Plasmid containing P <sub>00</sub> - <i>cheY-Cgfp-cheZ-Ngfp</i>	This study
4703	<i>E. coli</i> MG1655	pCRO9	Plasmid containing P <sub>II</sub> - <i>cheY-Cgfp-cheZ-Ngfp</i>	This study
4728	<i>E. coli</i> MG1655	pCRO10	Same as 4610, but with a frameshift mutation in <i>cheY</i>	This study
4729	<i>E. coli</i> MG1655	pCRO11	Same as 4610 but with a frameshift mutation in <i>cheZ</i>	This study
4743	<i>E. coli</i> MG1655	pCRO12	Same as 4610 but with a frameshift mutation in <i>cheY</i> and <i>cheZ</i>	This study

5325	<i>E. coli</i> MG1655 $\Delta$ <i>cheA</i>		Deletion of <i>cheA</i> gene	This study
5343	<i>E. coli</i> MG1655 $\Delta$ <i>cheA</i>	pCRO9	Same as 4610 in host 5325	This study
5086	<i>E. coli</i> MG1655 $\Delta$ <i>fliC</i>		Deletion of <i>fliC</i> gene	This study
5100	<i>E. coli</i> MG1655 $\Delta$ <i>fliC</i>	pCRO9	Same as 4610 in host 5086	This study
5397	<i>E. coli</i> MG1655 $\Delta$ <i>fliM</i>		Deletion of <i>fliM</i> gene	This study
5405	<i>E. coli</i> MG1655 $\Delta$ <i>fliM</i>	pCRO9	Same as 4610 in host 5397	This study
5391	<i>E. coli</i> MG1655 $\Delta$ <i>cheYcheZ</i>		Deletion of <i>cheYcheZ</i> operon	This study
5395	<i>E. coli</i> MG1655 $\Delta$ <i>cheYcheZ</i>	pCRO9	Same as 4610 in host 5391	This study
5396	<i>E. coli</i> MG1655 $\Delta$ <i>tsr</i>		Deletion of <i>tsr</i> gene	This study
5401	<i>E. coli</i> MG1655 $\Delta$ <i>tsr</i>	pCRO9	Same as 4610 in host 5396	This study

---

## **Acknowledgements**

I thank to Lavinia Bottinelli who initiated the cloning of the split-Gfp fusion during a summer internship and to Serge Pelet who developed Matlab scripts for image analysis.

**References:**

1. Baker MD, Wolanin PM, & Stock JB (2006) Signal transduction in bacterial chemotaxis. *Bioessays* 28(1):9-22.
2. Sourjik V & Wingreen NS (2012) Responding to chemical gradients: bacterial chemotaxis. *Curr Opin Cell Biol* 24(2):262-268.
3. Vladimirov N & Sourjik V (2009) Chemotaxis: how bacteria use memory. *Biol Chem* 390(11):1097-1104.
4. Sourjik V & Berg HC (2002) Receptor sensitivity in bacterial chemotaxis. *Proc Natl Acad Sci USA* 99(1):123-127.
5. Ghosh I, Hamilton AD, & Regan L (2000) Antiparallel leucine zipper-directed protein reassembly: Application to the green fluorescent protein. *Journal of the American Chemical Society* 122(23):5658-5659.
6. Jeong J, Kim SK, Ahn J, Park K, Jeong EJ, Kim M, & Chung BH (2006) Monitoring of conformational change in maltose binding protein using split green fluorescent protein. *Biochem Biophys Res Commun* 339(2):647-651.
7. Kerppola TK (2006) Visualization of molecular interactions by fluorescence complementation. *Nat Rev Mol Cell Biol* 7(6):449-456.
8. Kerppola TK (2008) Bimolecular fluorescence complementation (BiFC) analysis as a probe of protein interactions in living cells. *Annu Rev Biophys* 37:465-487.
9. Hu CD, Chinenov Y, & Kerppola TK (2002) Visualization of interactions among bZIP and Rel family proteins in living cells using bimolecular fluorescence complementation. *Mol Cell* 9(4):789-798.
10. Unoki T, Matsuda S, Kakegawa W, Van NT, Kohda K, Suzuki A, Funakoshi Y, Hasegawa H, Yuzaki M, & Kanaho Y (2012) NMDA receptor-mediated PIP5K activation to produce PI(4,5)P<sub>2</sub> is essential for AMPA receptor endocytosis during LTD. *Neuron* 73(1):135-148.

11. Guo Y, Rebecchi M, & Scarlata S (2005) Phospholipase C  $\beta$  2 binds to and inhibits phospholipase C  $\delta$  1. *J Biol Chem* 280(2):1438-1447.
12. Morell M, Espargaro A, Aviles FX, & Ventura S (2007) Detection of transient protein-protein interactions by bimolecular fluorescence complementation: the Abl-SH3 case. *Proteomics* 7(7):1023-1036.
13. Schmidt C, Peng B, Li Z, Sclabas GM, Fujioka S, Niu J, Schmidt-Supprian M, Evans DB, Abbruzzese JL, & Chiao PJ (2003) Mechanisms of proinflammatory cytokine-induced biphasic NF- $\kappa$ B activation. *Mol Cell* 12(5):1287-1300.
14. Alper H, Fischer C, Nevoigt E, & Stephanopoulos G (2005) Tuning genetic control through promoter engineering. *Proc Natl Acad Sci U S A* 102(36):12678-12683.
15. Sourjik V & Berg HC (2000) Localization of components of the chemotaxis machinery of *Escherichia coli* using fluorescent protein fusions. *Mol Microbiol* 37(4):740-751.
16. Rao CV, Kirby JR, & Arkin AP (2005) Phosphatase localization in bacterial chemotaxis: divergent mechanisms, convergent principles. *Phys Biol* 2(3):148-158.
17. Lipkow K (2006) Changing cellular location of CheZ predicted by molecular simulations. *PLoS Comput Biol* 2(4):e39.
18. Vaknin A & Berg HC (2004) Single-cell FRET imaging of phosphatase activity in the *Escherichia coli* chemotaxis system. *Proc Natl Acad Sci U S A* 101(49):17072-17077.
19. Andersen JB, Sternberg C, Poulsen LK, Bjorn SP, Givskov M, & Molin S (1998) New unstable variants of green fluorescent protein for studies of transient gene expression in bacteria. *Appl Environ Microbiol* 64(6):2240-2246.
20. Cabantous S, Nguyen HB, Pedelacq JD, Koraichi F, Chaudhary A, Ganguly K, Lockard MA, Favre G, Terwilliger TC, & Waldo GS (2013) A new protein-protein interaction sensor based on tripartite split-GFP association. *Sci Rep* 3:e2854.
21. Alford SC, Ding Y, Simmen T, & Campbell RE (2012) Dimerization-dependent green and yellow fluorescent proteins. *ACS Synth Biol* 1(12):569-575.

22. Alford SC, Abdelfattah AS, Ding Y, & Campbell RE (2012) A fluorogenic red fluorescent protein heterodimer. *Chem Biol* 19(3):353-360.
23. Cui B, Wang Y, Song Y, Wang T, Li C, Wei Y, Luo ZQ, & Shen X (2014) Bioluminescence resonance energy transfer system for measuring dynamic protein-protein interactions in bacteria. *MBio* 5(3):e01050-01014.
24. Shimizu TS, Delalez N, Pichler K, & Berg HC (2006) Monitoring bacterial chemotaxis by using bioluminescence resonance energy transfer: absence of feedback from the flagellar motors. *Proc Natl Acad Sci U S A* 103(7):2093-2097.
25. Miller WG, Leveau JHJ, & Lindow SE (2000) Improved *gfp* and *inaZ* broad-host-range promoter-probe vectors. *Molecular Plant-Microbe Interactions* 13(11):1243-1250.
26. Reimer A, Yagur-Kroll S, Belkin S, Roy S, & van der Meer JR (2014) *Escherichia* [corrected] *coli* ribose binding protein based bioreporters revisited. *Sci Rep* 4:e5626.
27. Merulla D, Hatzimanikatis V, & van der Meer JR (2013) Tunable reporter signal production in feedback-uncoupled arsenic bioreporters. *Microbial Biotechnology* 6(5):503-514.
28. Martinez-Garcia E & de Lorenzo V (2011) Engineering multiple genomic deletions in Gram-negative bacteria: analysis of the multi-resistant antibiotic profile of *Pseudomonas putida* KT2440. *Environmental Microbiology* 13(10):2702-2716.
29. Ducret A, Quardokus EM, & Brun YV (2016) MicrobeJ, a tool for high throughput bacterial cell detection and quantitative analysis. *Nature Microbiology* 1(7):e16077.





## CHAPTER 5

### MEASURING PROTON FLOW FROM CHEMOTAXIS THROUGH THE CYTOPLASMIC MEMBRANE USING PH-SENSITIVE FLUORESCENT PROTEIN

Instead of by ATP, bacterial flagellar rotation is energized by a flux of ions through the cytoplasmic membrane, which can be  $\text{Na}^+$  for marine bacteria or  $\text{H}^+$  for *Escherichia coli* and most other bacterial species. Multiple experiments have been performed to understand the effect of changes of intracellular pH or pH gradient on the rotation properties of the flagella. It was shown that a decrease of the pH inside the cell leads to a reduction or even complete arrest of the rotation speed of the flagellum. The goal of the work in this chapter was to test whether pH changes occurring in chemotaxis-active cells would be measurable, which would be the consequence of a modification of the flagellar rotation due to the chemotaxis response. To test this hypothesis, we measured cytoplasmic and periplasmic pH through a compartment-specific expression of a pH-sensitive fluorescent protein (pHluorin). We demonstrated proper expression of pHluorin in the cytoplasm and in the periplasm, and showed that a linear correlation exists between fluorescence emission ratio and extracellular-calibrated pH. An increase of the cytoplasmic pH and decrease of the periplasmic pH were measured in *E. coli* WT accumulating close to a source of serine in the agarose plug assay, suggesting that cellular pH could be used as proxy for chemotaxis activity.

## Introduction

Bacterial flagella are composed of more than 30 proteins that assemble in a complex rotating structure that can propel the cell at a speed of up to hundred micrometers per second for the fastest species [1-3]. For its rotation, the flagellar motor uses a flux of ions through the cytoplasmic membrane as source of energy. Some marine bacteria, such as *Vibrio* sp., use sodium motive force and Na<sup>+</sup>-influx, but the majority of motile bacteria like *Escherichia coli*, uses the proton gradient and H<sup>+</sup>-influx for flagellar rotation [1, 4]. It has been estimated that for one turn of the flagellum, about 1200 protons enter into the cytoplasm and that a flagellum can rotate at a speed of 300 rps, suggesting superfast proton influx [1, 5]. The protons cross the membrane through up to eight protein complexes called the 'stators', composed of MotA and MotB subunits that transmit the energy to the motor [1, 3].

Previous studies have shown that experimental manipulation of the intracellular and extracellular pH can modify flagellar rotation. Notably, it was demonstrated that a low intracellular and extracellular pH induces a decrease of flagellar rotation speed [6]. It has further been proposed that the rotational speed of the flagella is influenced by the absolute amount of free protons in the cytoplasm [6]. In the 1980's, it was shown that a decrease or an increase of cytoplasmic pH provoked by weak acids or weak bases induced respectively a repellent or an attractant response in *E. coli* and in *Salmonella* [7, 8]. More recently, Morimoto *et al.* showed that chemotaxis in *Salmonella* is affected by the intracellular pH by inducing a proton leakage through the membrane due to overexpression of the MotA/B stator. These bacteria showed an increase in the tumble frequency and smaller colonies on swarming plates, which is indicative for repellent response [9].

The link between the proton gradient and flagella rotation has always been studied from the perspective of rotation speed. Instead, we wondered whether there would be a (measurably) transient change of proton concentration near the flagellum when the cell detects an attractant, which could perhaps be exploited as a proxy for chemical signaling. Such proton concentration

change could result from the decrease in the frequency of change of rotation direction of the flagella, or from an increase in the speed of rotation. On the other hand, it is supposed that proton inflow occurs irrespective of *E. coli* flagellar motor rotation direction, and therefore, a local pH change may not be completely accurately reflecting attraction of a cell to a chemical compound.

Expression of the pHluorin, a pH-sensitive variant of the green fluorescent protein, is a non-invasive method to measure intracellular pH. It has initially been used to study release and recycling of neurotransmitters in neuronal cells [10]. pHluorin shows a bimodal excitation at 390 nm and at 470 nm, and a single emission at 508 nm (Fig 1A) [10]. Fluorescence emission intensity increases with increasing pH at 390 nm excitation and in return decreases with increasing pH when excited at 470 nm (Fig. 1B). This allows the calculation of an emission ratio at 508 nm (as the ratio of emission<sub>508</sub> at excitation<sub>390</sub> and the emission<sub>508</sub> at excitation<sub>470</sub>), which was reported to be linearly proportional to the pH (Fig 1C) [10]. Measurement of the pHluorin fluorescence is non-invasive and rapid, and it is reversible upon changing pH. The sensitivity for pH change is approximately 0.2 pH units, measured on the cytoplasm of *Salmonella* [9].

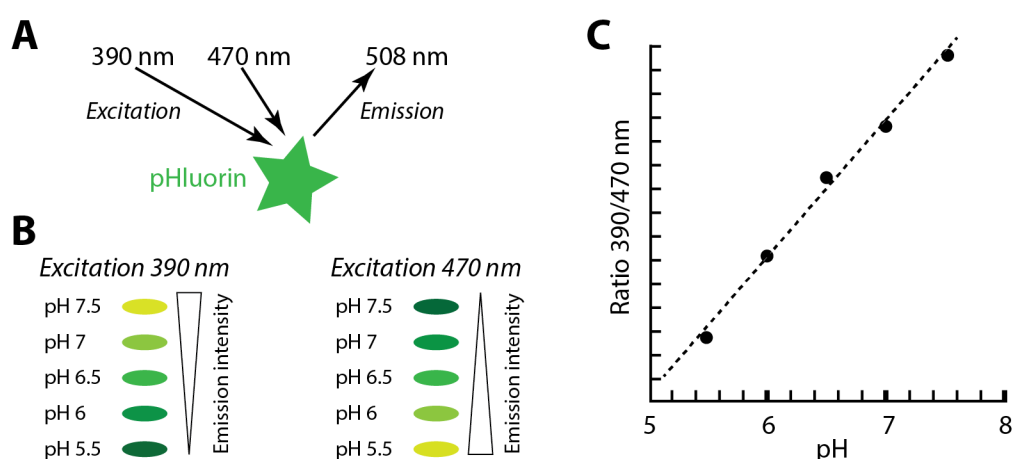


**Figure 1: pHluorin emission properties.** (A) pHluorin shows a bimodal excitation at 390 nm and 470 nm with a single emission wavelength at 508 nm. (B) The emission intensity increases with increasing pH at 390 nm of excitation and decreases with increasing pH at 470 nm. (C) The calculation of an emission intensity ratio (as the ratio of emission<sub>508</sub> at excitation<sub>390</sub> and the

emission<sub>508</sub> at excitation<sub>470</sub>) is linearly correlated with external induced pH (graph redrawn from Miesenbock *et al.* (1998) [10]).

To test our hypothesis, we decided to see whether we could measure the cytoplasmic and periplasmic pH of swimming bacteria, and whether we could monitor cellular pH changes in presence of chemical attractant gradient. For this purpose, we expressed the pHluorin either in the cytoplasm or in the periplasm of motile *E. coli* MG1655. After verifying proper expression and export, both strains were exposed to a gradient of attractant (serine) by agarose plug assay. We expected that this would produce an important accumulation of chemotaxis-reactive cells, which increases the sensitivity of the ratiometric measurement in epifluorescence microscopy.

## Results

### *pHluorin expression in the cytoplasm and in the periplasm*

In order to measure the pH in cytoplasm, we expressed pHluorin under the control of the L-arabinose inducible *araC* promoter in wild-type motile *E. coli* MG1655 (Fig. 2A). Increasing arabinose concentration (between 0 and 10 g l<sup>-1</sup>) resulted in an increase of expression of the fluorescent protein (Fig. 2C), with optimal expression obtained at a concentration of 0.1% (1 g l<sup>-1</sup>) arabinose. pHluorin fluorescence localized homogeneously in the cytoplasm without any subcellular localization (Fig. 2E). As expected, expression between individual cells was variable, which may be the result of differences in arabinose uptake and thus pHluorin expression.

In order to express pHluorin in the periplasm, we linked a *torA* signal sequence [11] to its N-terminal end (torA-pHluorin). This would enable recognition by the twin-arginine translocation (Tat) pathway, which exports folded proteins from the cytoplasm into the periplasm (Fig. 2B) [11]. Translocation was favored by first inducing torA-pHluorin expression in *E. coli* in presence of arabinose, followed by incubation in medium without arabinose. Similar to expression of pHluorin in the cytoplasm, torA-pHluorin fluorescence intensity was increasing at increasing arabinose concentrations, but with highest visible expression at 1% arabinose (Fig. 2D). Epifluorescence microscopy images of torA-pHluorin expressing cells showed a "ring-like" appearance, indicating that the protein was efficiently exported into the periplasm (Fig. 2F).

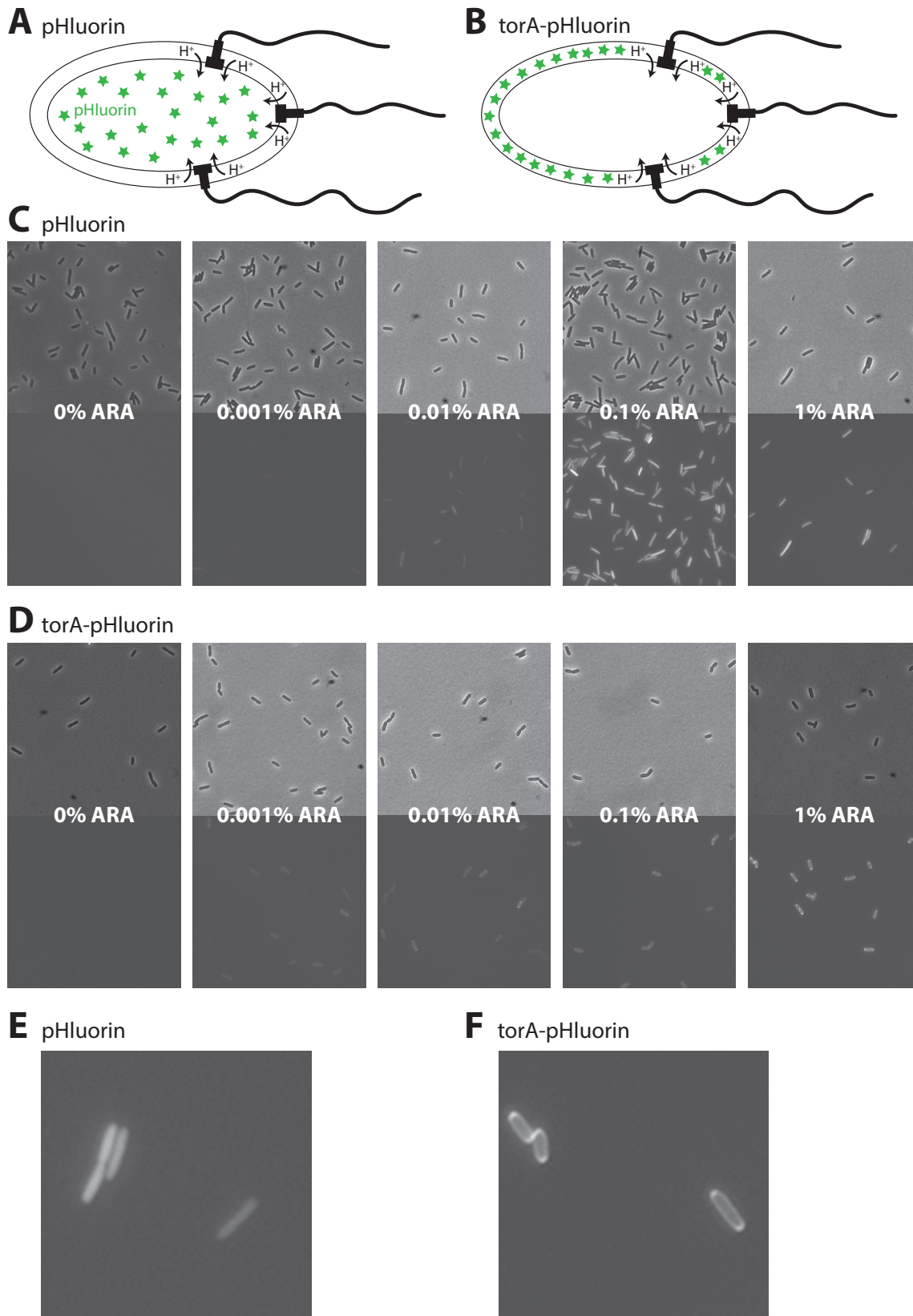


**Figure 2: Induction of pHluorin expression in the *E. coli* cytoplasm and periplasm.** Schematics of expected localization of pHluorin without any tags in the cytoplasm (A) and in the periplasm in case of attachment of the torA-signal sequence. (B) Phase contrast and

epifluorescence images of cells incubated with tenfold increasing arabinose concentrations, for the case of cytoplasmic pHluorin (B) or periplasmic torA-pHluorin (C). Enlarged images of individual cells expressing pHluorin (E) or exporting the torA-pHluorin into the periplasm (F), after induction with 1% arabinose.

### *pHluorin response to different pHs*

In order to test the pH-sensitive properties of pHluorin, its fluorescence was calibrated as a function of external pH by spotting *E. coli* cells on agarose patches containing 20 mM sodium benzoate at pHs ranging between 6 and 8. Benzoate is a weak acid that can equilibrate cytoplasmic and extracellular pH [12]. Cells were imaged by microscopy with excitations at 386 nm or 470 nm and emissions recorded both at 525 nm.

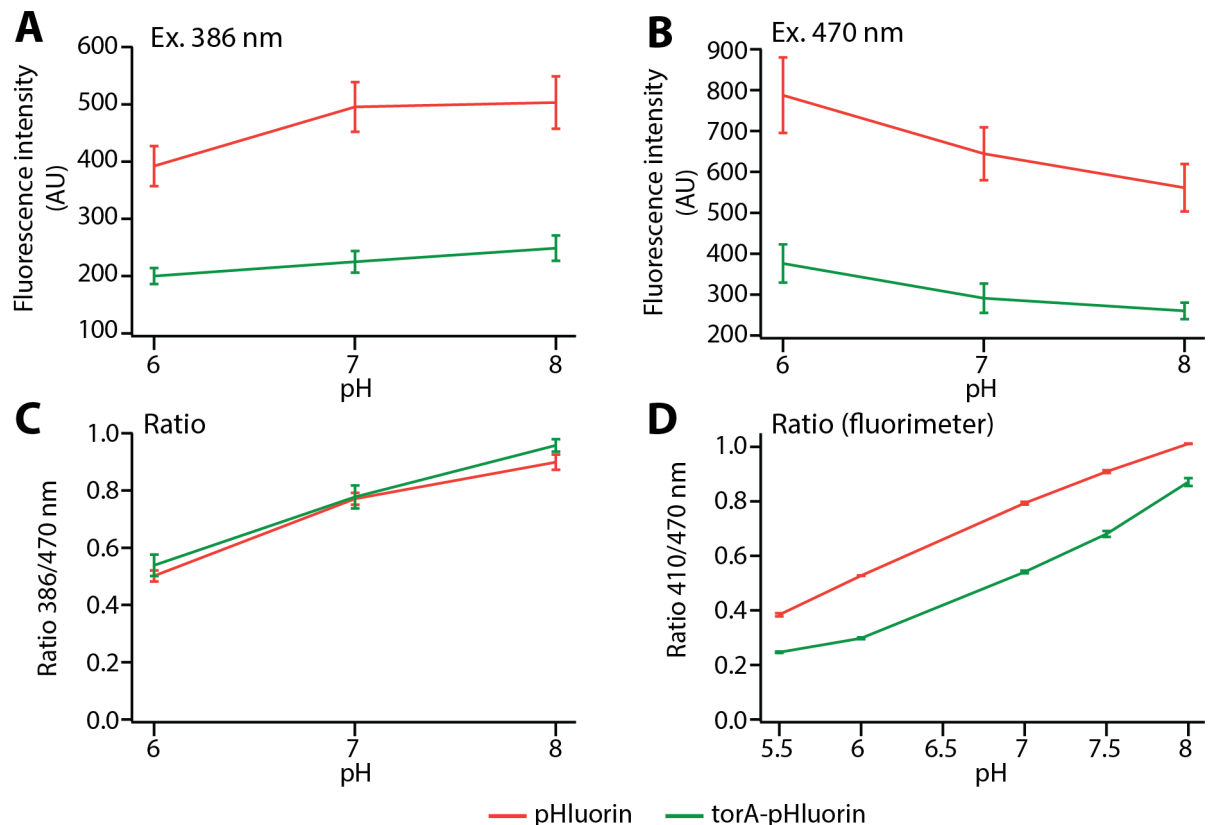


**Figure 3: pHluorin or torA-pHluorin fluorescence as a function of external pH. (A)** 525-nm emission intensity of cytoplasmic pHluorin (red) or periplasmic torA-pHluorin (green) at an excitation wavelength of 386 nm at three different pHs measured by microscopy. **(B)** Same as



(A) but at an excitation wavelength of 470 nm. (C) 525-nm fluorescence emission ratio between excitation at 386 nm and at 470 nm. Error bars correspond to one standard deviation with the mean of at least 500 individual cells, imaged by epifluorescence microscopy on 20 mM sodium-benzoate containing agarose surfaces. (D) 535-nm fluorescence emission ratio between excitation at 410 nm and at 470nm. Errors bars correspond to one standard deviation with the mean of 3 replicate cultures measured with a fluorimeter in medium containing 20 mM sodium benzoate.

Image analysis of individual cells showed an increase of the fluorescence emission between pH 6 and 8 when cells were excited with a wavelength of 386 nm both with cytoplasmic and periplasmic pHluorin (Fig. 3A). At the excitation wavelength of 470 nm, cells expressing pHluorin or torA-pHluorin both showed a decrease of the 525-nm fluorescence emission at increasing pH between 6 and 8 (Fig. 3B). The ratio of fluorescence at 386/470 nm increased linearly at increasing external pH, confirming previous literature values [10] (Fig. 3C). Of note that the variation of the emission ratio among individual cells, expressing either pHluorin or torA-pHluorin, was relatively small, even though the variation of the absolute fluorescence emission intensities was more important between individual cells and strains (Fig. 3A, B).

We also verified the pH-sensitive response of the pHluorin on a larger range of pHs using a fluorimeter (pH from 5.5 to 8). Bacterial liquid cultures supplemented with 20 mM sodium benzoate were excited at 410 nm and 470 nm and fluorescence emission was measured at 535 nm. The ratio of fluorescence at 410/470 nm increased linearly with increasing external pH with pHluorin expressed in the cytoplasm and in the periplasm (Fig. 3D). The differences with the ratios calculated from microscopy images probably arose from the use of different excitation and emission filters but these results emphasize the robustness of the pH sensitivity of pHluorin.

These results suggest that external pH changes are followed by pH changes both in the cytoplasm and in the periplasm caused by addition of sodium benzoate to the growth medium.

The resulting calibration curve can thus be used to deduce intracellular and periplasmic pH of *E. coli* cells during chemotaxis experiments from the observed fluorescence emission ratios.

### *Chemotaxis causes a net temporary change in pH*

In order to facilitate measuring the pHluorin signals produced from individual cells as a result of pH changes from chemotaxis effects, we created conditions to maximize the number of chemotactically reactive cells in microscopy settings. We chose to adapt the agarose plug assay for this purpose, since it will result in cells accumulating nearby an attractant source within 10-15 min (see, e.g., Chapter 6). In short, the respective *E. coli* cell suspension was inserted in a very shallow (130-170  $\mu\text{m}$ ) microscope chamber filled with a round and flat solidified agarose source containing 0.1 mM serine. As soon as cell suspension is inserted, serine diffuses from the source, creating a chemical gradient perceived by the cells, which over the course of minutes accumulate close to the border of the agarose plug (see, Fig. 1 in Chapter 6). Fluorescence from the cells is then measured at the two excitation wavelengths as a function of distance to the source.

*E. coli* expressing pHluorin or torA-pHluorin had clearly accumulated close to the 0.1 mM serine source 20–30 min after the start of the incubation (Fig. 4A-B, pink lines). No significant cell accumulation was observed with an agarose source that did not contain any attractant (Fig. 4A-B, blue lines – control). These results suggested that the expression of the fluorescence protein did not impair chemotaxis response of both strains.

Fluorescence quantification of *E. coli* cells expressing pHluorin (in the cytoplasm) showed an increase of the pHluorin emission ratio close to the serine source followed by a general decrease, compared to a constant signal decrease in absence of any attractant (Fig. 4C). In contrast, fluorescence quantification of *E. coli* expressing torA-pHluorin showed a steep decrease of the emission ratio close to the source followed by a slow increase, compared to a constant signal decrease in the control (Fig. 4D). In both instances, cells furthest away from the source showed equal emission ratios for attractant or no attractant (Fig. 4C-D).

Contrary to our initial expectations, these measurements would imply an increase of the pH in the cytoplasm and decrease in the periplasm in chemotaxis-active cells.

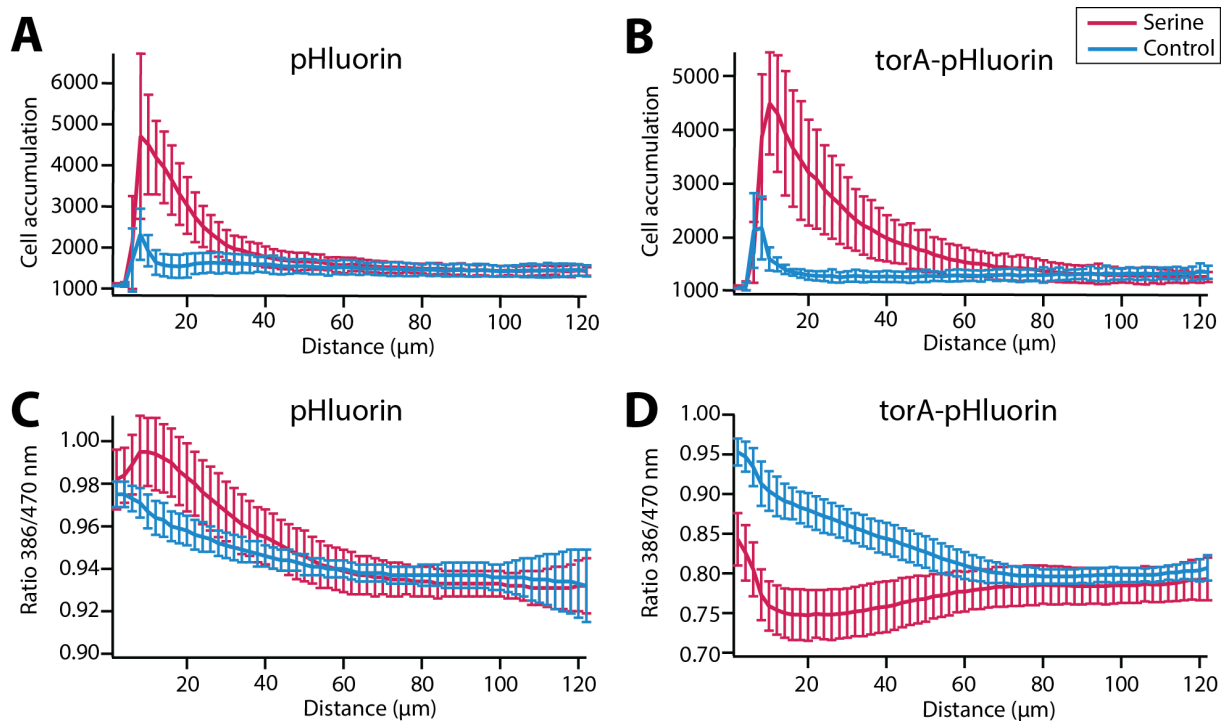


**Figure 4: pHluorin measurement during agarose plug assay. (A)** Average cell accumulation of *E. coli* MG1655 expressing pHluorin as a function of distance from the source extracted from images taken after 20-30 min of incubation for four biological replicates on both sides of the agarose plug with 100 μM serine (pink, serine) or no attractant (blue, control) **(B)** As (A) but with *E. coli* MG1655 expressing torA-pHluorin (periplasm). **(C)** Ratio of fluorescence emission at 525 nm of *E. coli* MG1655 cells expressing pHluorin as a function of distance from the source with or without 100 μM serine. **(D)** As (C) but with *E. coli* MG1655 expressing torA-pHluorin. Note that the scales of the graphs are different.

## Discussion

Flagellar rotation in *E. coli* is powered by an influx of proton through the cytoplasmic membrane. The addition of attractant induces a change in the rotation phenotype of the flagella, which turn longer in counterclockwise direction, decreasing the frequency of rotation direction switches. We hypothesized that this change would lead to a temporary decrease of the pH in the cytoplasm as a result of proton influx and pH increase in the periplasm as a result of temporary proton depletion. To measure this, we expressed the pH-sensitive pHluorin fluorescent protein in the cytoplasm and in the periplasm. Induction of pHluorin expression in both cell compartments was verified by epifluorescence microscopy, which showed that pHluorin remained cytoplasmic whereas torA-pHluorin localized to the periplasmic space (Fig. 2).

We could further show that the fluorescence emission intensity ratio of pHluorin increased with increasing external pH between 5.5 and 8, confirming previous results by others (Fig. 3) [10]. The emission ratio was a robust parameter and was similar between *E. coli* expressing pHluorin in the cytoplasm or torA-pHluorin in the periplasm. The variation of the ratio among individual cells was low even when the absolute fluorescence emissions varied more from cell to cell (Fig. 3). This showed that the ratio is insensitive to individual cell expression differences and that, therefore, it is a robust proxy to measure pH of the cyto- and periplasm. The emission-ratio versus pH calibration curve (between pH 6 and 8, Fig. 3C) can thus be used to estimate the *equivalent* pH of individual cells during chemotaxis.

Our initial experiments, where we deployed motile cells in solution exposed instantly or not to attractant or repellent, were not satisfactory in terms of reproducible fluorescence emission ratio changes (not shown). We suspected that the difficulty would lay in creating an appropriate chemical gradient and sufficient cells perceiving this gradient. In order to possibly increase the sensitivity of fluorescence ratio measurements, we exploited the agarose plug assay in an epifluorescence microscopy setting. Other results (see Chapter 6) had shown that *E. coli* cells accumulate within 10–15 min after the onset of exposure to a serine gradient diffusing

from a solid 0.1 mM agarose source (see, Fig. 1 in Chapter 6). The difficulty, however, was to obtain sufficient imaging quality of both accumulating cells and their fluorescence at two excitation wavelengths. Because of the time needed for filter change we could not image individual motile cells at high magnification (e.g., 600–1000×). Instead, we relied on lower magnifications, which are less sensitive to cell blurring (200×). Rather surprisingly, we obtained quite robust values of pHluorin and torA-pHluorin emission ratios from accumulating *E. coli* cells as a function of distance to the solid source (Fig. 4). Since cells are in presence of a continuous gradient, they will react during a relatively long time (10–40 min), enabling optimal measurements. As expected, both *E. coli* accumulated very strongly to a 0.1 mM serine source, but not to a source without attractant (Fig. 4). Quite interestingly, the pHluorin emission ratio increased in cells close to the serine source compared to an empty source, whereas the torA-pHluorin emission ratio decreased closed to the serine source (Fig. 4). The inverse response in the cyto- versus periplasm, suggests that the pH of the cytoplasm increases whereas that of the periplasm decreases in chemotaxis-active cells (Fig. 4). The fact that both signals were opposite indicates that they were not artifacts simply due to the cell accumulation close to the source.

When assuming our calibration of pHluorin fluorescence ratios in individual cells as a function of external imposed pH, we can calculate the equivalent pH of the cytoplasm and the periplasm in chemotaxis-active cells. In *E. coli* cells in absence of attractant, the equivalent cytoplasmic pH would correspond to 8 and that of the periplasm of 7.2 (Fig. 5). A lower pH in the periplasm is in general agreement with a net outside proton gradient across cytoplasmic membrane in actively respiring cells. The calculated periplasmic pH also corresponds to the pH of the motility buffer. In contrast, in presence of an attractant, reactive cells showed an increase of 0.4 pH units in the cytoplasm (from pH 8 to 8.4) and a decrease of 0.2 units in the periplasm (from pH 7.2 to 7) (Fig. 5).

These results are not in immediate agreement with our initial hypothesis that increased chemotaxis activity would increase proton flux through the stator of the motor, and, correspondingly, would decrease cytoplasmic pH. Instead, our results suggest that chemotaxis-

active cells increase proton efflux from the cytoplasm to the periplasm, perhaps in order to compensate and sustain the high proton influx through the flagellar motor. The increased proton efflux may find its origin in temporarily higher respiration rates [13]. Less likely, the protons could come from the extracellular medium, but no active transporters are present in the outer membrane to sustain such pH disequilibrium (Fig. 5). The net increase of pH gradient between the periplasm and the cytoplasm would on its turn facilitate the proton requirements by the flagellar motor.

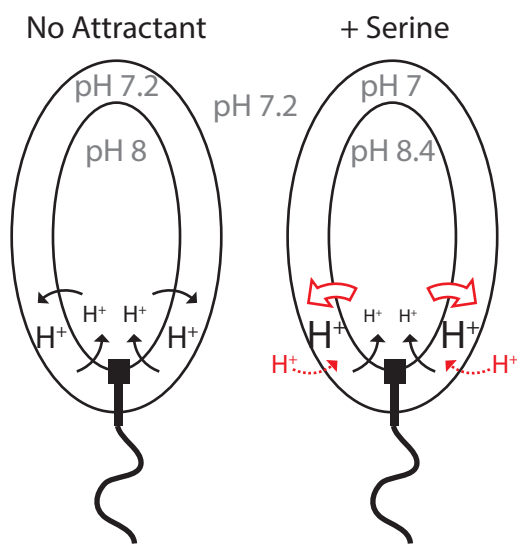


**Figure 5: Model of pH homeostasis in chemotaxis**

Without attractant, cytoplasmic and periplasmic pHs judged from fluorescence calibration are equivalent to 8 and 7.2 (in grey). The rotation of the flagella induces an entry of protons, which is compensated by an efflux of protons from the respiratory chain. In presence of attractant, the cytoplasmic pH increased to 8.4 and the periplasmic pH decreased to 7. This changes implies a net increase of proton efflux from the cytoplasm, perhaps as a result of increased respiratory activity, or further as a result of proton diffusion from the extracellular space.

Although the measured emission ratio change of pHluorin and torA-pHluorin fluorescence in cells accumulating near the serine source was relatively clear, compared to no attraction source (Fig. 4C-D), it is tricky to find appropriate control experiments. To test for the effect of cell accumulation itself on the fluorescence signal, one might produce a control of accumulating motile cells that express (torA-)pHluorin but that do not display chemotaxis

response, but this is difficult to achieve experimentally. One might also think about testing an *E. coli* mutant with deletion of the MotA/B stator complex or without the flagellar motor, which would have no inflow of protons into the cytoplasm. But this mutant would essentially be non-motile, so it would require an artificial cell accumulation close to the source of attractant in order to amplify the signal to the same level as seen in Fig. 4A and B. We can also think of adding antibodies directed against the flagella or sodium azide after cellular accumulation to block respectively flagellar rotation or respiration and thus stop proton flow, but this is also experimentally delicate.

At single cell level it would be interesting to measure whether the observed signal difference in accumulating cells is localized in the cytoplasm and in the periplasm near the flagellar motors. However, the signal localization might be very weak. We think that, in our experiment, the cell accumulation in a serine gradient was the crucial factor to have chemotaxis-active cells and to amplify the signal sufficiently. In order to measure the inflow of proton through the flagellar motor at single cell level, one approach could be to localize more precisely the pHluorin at the motor or at the stator. A fusion protein of pHluorin(M153R) (a more stable and brighter pHluorin variant [14]) with the FliG protein of the motor has been recently used to measure pH variations during flagellum export in YVMN001 strain lacking both the MotA/B stator and the complete export gate [15]. This measurement would require high resolution microscopy, and is technically complicated because the cells have to be immobilized to obtain proper focus while allowing their flagella to turn to produce a proton flux, and will have to be simultaneously embedded in an attractant gradient to show chemotaxis response.

In conclusion, measurement of cytoplasmic and periplasmic pH in chemotaxis-active *E. coli* cells showed a lower pH in the periplasm and a higher pH in the cytoplasm. This could derive from higher respiration rate or influx of protons from extracellular space, but this is difficult to confirm since respiration and motility cannot be dissociated in our current experimental setup.

## Material and methods

### Expression vector construction

In order to express pHluorin in the periplasm, the *torA* signal sequence [11] was added to the 5'-end of the *pHluorin* sequence (AF058694.2) flanked by two NcoI restriction sites. The DNA sequence was synthesized by DNA 2.0 (CA, USA) and delivered in their custom vector pJ201. The whole synthesized sequence was flanked with EcoRI and HindIII restriction sites (Fig. 6). The *torA-pHluorin* sequence was cloned downstream of P<sub>BAD</sub> in pBAD24 using EcoRI and HindIII restriction sites to express the protein after induction with arabinose. After transformation in *E. coli* MG1655 this yielded plasmid pCRO4. From pCRO4, the *torA* signal sequence was removed by digestion with NcoI and recircularization of the vector (pCRO5). Plasmid pCRO5 was used to express pHluorin in the *E. coli* cytoplasm.

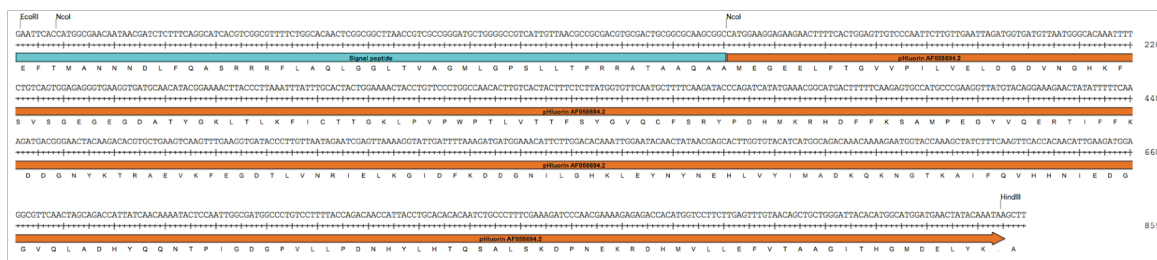


**Figure 6: Sequence of synthesized ‘torA-pHluorin’.** The *torA-pHluorin* sequence is composed of the *torA* signal sequence upstream *pHluorin* sequence (AF058694.2). Two NcoI restriction sites were introduced to allow removal of the *torA* signal sequence and obtain cytoplasmic expression of pHluorin itself. The EcoRI and HindIII restriction sites were used to clone the fragment in pBAD24.

### Bacterial strains and culture conditions

Motile *E. coli* MG1655 wild-type from *E. coli* Genetic Center, Yale (CGSC#8237) were transformed with the constructed plasmid pBAD24-pHluorin (pCRO5) or pBAD24-torA-



pHluorin (pCRO4) (see table 1). The strains were grown at 37°C with 180 rpm shaking in M9-Glc minimal medium (see Chapter 2) supplemented with 100 µg ml<sup>-1</sup> of ampicillin (Ap100).

### *Epifluorescence microscopy*

In order to measure pHluorin or torA-pHluorin expression at single cell level, overnight cultures of *E. coli* MG1655 pCRO5 or MG1655 pCRO4 were diluted in the same medium supplemented without or with a range of L-arabinose concentrations (1%, 0,1%, 0,01%, 0,001% w/v), and were further incubated at 37°C until reaching exponential phase (OD<sub>600</sub> ~ 0.5). *E. coli* containing pCRO5 was then sampled directly and observed under epifluorescence microscopy. To allow export of torA-pHluorin into the periplasm, strain MG1655 pCRO4 was harvested by centrifugation at 2'400 × g for 5 min, then resuspended in the same volume of M9-Glc without arabinose and incubated for a further 2 h at 37°C.

For epifluorescence microscopy, aliquots of 400 µl culture were centrifuged at 2'400 × g for 5 min to pellet the cells. The cell pellet was resuspended in 50 µl of M9-Glc medium without arabinose. A drop of 7 µl of this cell suspension was deposited on a 1% agarose in M9 coated standard microscopy slide and covered with a cover slip (24 × 50 mm, Menzel Gläser). Images were immediately taken with a Zeiss Axioplan II epifluorescence microscope equipped with a 100× Plan Apochromat oil objective lens (Carl Zeiss, Jena, Germany) and a SOLA SE light engine (Lumencor, USA). We used an eGFP HQ excitation filter at 470 nm with a bandwidth of 40 nm and an emission filter at 525 nm with a bandwidth of 50 nm (Chroma Technology Corp, VT, USA).

### *pH sensitivity of pHluorin fluorescence emission ratio*

In order to determine the effect of external pH on (torA-)pHluorin fluorescence emission, overnight cultures of *E. coli* MG1655 pCRO5 and MG1655 pCRO4 were diluted 100-fold in fresh M9-Glc-Ap100 and incubated for 3 hours at 37°C with 180 rpm shaking until they reached exponential phase (OD<sub>600</sub> ~0.5-0.6). Both cultures was centrifuged at 2,400 × g for 5

min, resuspended in motility buffer (see Chapter 2) supplemented by 0.5 % of arabinose and ampicillin ( $100 \mu\text{g ml}^{-1}$ ) and incubated at  $37^\circ\text{C}$  for 2.5 h in order to induce the expression of the pHluorin. At this point *E. coli* MG1655 pCRO5 was used immediately for microscopy, whereas MG1655 pCRO4 was centrifuged at  $2,400 \times g$  for 5 min, resuspended in motility buffer and incubated for a further 2 h at  $37^\circ\text{C}$  to allow the export of torA-pHluorin into the periplasm.

Agarose solutions for slide coating were prepared with three different pHs (pH6, pH7 and pH8) by melting 1% (w/v) agarose in M63 minimal medium [ $0.4 \text{ g L}^{-1} \text{ KH}_2\text{PO}_4$ ,  $0.4 \text{ g L}^{-1} \text{ K}_2\text{HPO}_4$ ,  $2 \text{ g L}^{-1} (\text{NH}_4)_2\text{SO}_4$ ,  $7.45 \text{ g L}^{-1} \text{ KCl}$ ] supplemented with  $2 \text{ g L}^{-1}$  casein hydrolase, 20 mM sodium benzoate and 50 mM of appropriate buffer. For pH 6.0, this consisted of 2-(N-morpholin)ethanesulfonic acid (MES); for pH 7.0, we used 3-morpholinopropane-1-sulfonic acid (MOPS); for pH 8.0, we used N-Tris(hydroxymethyl)methyl-3-amino-propanesulfonic acid (TAPSO)] [12].

Right before microscopy, an aliquot of  $400 \mu\text{l}$  culture was centrifuged at  $2,400 \times g$  for 5 min, and cells were resuspended in  $50 \mu\text{l}$  of M63 minimal medium supplemented by casein hydrolase, sodium benzoate and the respective pH buffer. A drop of  $7 \mu\text{l}$  of bacterial suspension was then deposited on a standard microscopy glass slide coated with the corresponding pH-agarose. Cells were immediately imaged using an sCMOS camera (Flash4.0, Hamamatsu) mounted on an inverted Ti-Eclipse epifluorescence microscope (Nikon) using an Apo PLAN 100 $\times$  oil objective. The excitation was provided by a solid-state light source (SpectraX, Lumencor) at a wavelength of 386 nm (bandwidth: 23 nm) or at a wavelength of 470 nm (bandwidth: 40 nm), and fluorescence emission was detected at a wavelength of 525 nm (bandwidth: 30 nm). The exposure times were 10 ms for the bright field and 10 ms for both fluorescence channels.

Fluorescence of individual cell were quantified on digital images using the MicrobeJ plugin in Image J ([www.microbej.com](http://www.microbej.com)) [16].

Fluorescence sensitivity to pH of *E. coli* MG1655 pCRO5 and MG1655 pCRO4 were also tested in liquid cultures with a fluorimeter. Culture were grown and induced using the same procedure as described just before. Cells were resuspended in M63 minimal medium

supplemented by 2 g L<sup>-1</sup> casein hydrolase, 20 mM sodium benzoate and buffer of pH ranging from 5.5 to 8 (for pH 5.5 and pH 6.0, we used MES buffer; for pH 7.0 and pH 7.5, we used MOPS buffer; for pH 8.0, we used TAPSO buffer). The bacterial cultures were loaded in a 96-well microtiter plate (200 µl) and fluorescence emission was measured at 535 nm (bandwidth 25 nm) with a TriStar<sup>2</sup> fluorimeter (Berthold) at excitation wavelengths of 410 nm (bandwidth 40 nm) and 470 nm (bandwidth 10 nm).

### *pHluorin measurements during source attraction*

Overnight cultures of *E. coli* MG1655 pCRO5 or MG1655 pCRO4 were diluted 100-fold in fresh M9-Glc-Ap100 supplemented with 0.5% of L-arabinose and incubated for 3 h at 37°C with 180 rpm shaking until they reached exponential phase (OD<sub>600</sub> ~0.5-0.6). MG1655 pCRO4 was centrifuged at 2,400 × g for 5 min, resuspended in same volume of motility buffer and incubated 2.5 h at 37°C to allow the export of the pHluorin in the periplasm. MG1655 pCRO5 was used directly; 1 mL of culture was centrifuged at 2,400 × g for 5 min, washed two times with 1 mL of motility buffer and resuspended in 500 µl of motility buffer, which corresponds to a density of ~10<sup>9</sup> cells ml<sup>-1</sup>. This process was repeated for MG1655 pCRO4 after the 2-h-export period.

To prepare the source of serine, 10 µl of serine solution (100 mM) was diluted in 10 ml of a 2% agarose solution (LE, Analytical grade, PROMEGA) in water, molten and kept at 55°C. As a negative control we used 2% agarose in water, molten and kept at 55°C.

On a standard microscopy glass slide (Menzel Gläser, Thermo Scientific), two small coverslips (24 × 24 mm, 0.13-0.17 mm thick, MGF-Slides) were deposited on both extremities, which were maintained in place with a thin layer of 10 µl of tap water. A drop of 5 µl of 55°C agarose solution was deposited in the middle and immediately covered by a cleaned large coverslip (24 × 50 mm, Menzel Gläser) that bridges over the side coverslips and thus creates a chamber with a height of 0.17 mm. An aliquot of 150 µl of freshly washed bacterial suspension in motility buffer was inserted around the agarose plug by pipetting in between the glass slide and the large coverslip.

Bacterial accumulation was imaged close to the source on either side after 15 to 35 min incubation at room temperature with an sCMOS camera (Flash4.0, Hamamatsu) mounted on an inverted Ti-Eclipse epifluorescence microscope (Nikon) using an N PLAN 20× air objective. pHluorin was excited by a solid-state light source (SpectraX, Lumencor) at 386 nm (bandwidth: 23 nm) or 470 nm (bandwidth: 40 nm) as before, whereas fluorescence emission was detected at 525 nm (bandwidth: 30 nm). The exposure times were 10 ms for the bright field and 30 ms for both fluorescence channels. Four independent source or negative control replicates were produced for every strain.

Cells were identified and their abundance was quantified using the “find edges” routine in ImageJ. The intensity values were averaged across successive outward-moving sectors of 25 pixels width (corresponding to 2  $\mu\text{m}$ ) parallel to the border of the agarose source (3 zones within the source and 57 zones outside the plug). Fluorescence values were extracted using the same sectors on respective images. The intensity values were then averaged on both sides and across four replicates, and plotted as a function of distance  $\pm$  one *SD* (Fig. 4).

**Table 1: Strain list**

Strain n°	Host	Plasmid	Relevant characteristics	Source of reference
4648	<i>E. coli</i> DH5 $\alpha$	pJ201	Synthetic torA-pHluorin	This study
4498	<i>E. coli</i> MG1655		Controlled for motility	<i>E. coli</i> Genetic Center, Yale (CGSC#8237)
4655	<i>E. coli</i> MG1655	pCR04	pBAD24-torA-pHluorin	This study
4656	<i>E. coli</i> MG1655	pCR05	pBAD24-pHluorin	This study

## **Acknowledgements**

I thank Giulia Torriani for her help in cloning of pCRO4 and pCRO5, as well as in the microscopy analysis. I acknowledge also Serge Pelet let me use his microscope for my agarose plug experiments.

## References

1. Berg HC (2000) Constraints on models for the flagellar rotary motor. *Philos Trans R Soc Lond B Biol Sci* 355(1396):491-501.
2. Magariyama Y, Sugiyama S, Muramoto K, Kawagishi I, Imae Y, & Kudo S (1995) Simultaneous measurement of bacterial flagellar rotation rate and swimming speed. *Biophys J* 69(5):2154-2162.
3. Blair DF (2003) Flagellar movement driven by proton translocation. *FEBS Lett* 545(1):86-95.
4. Yorimitsu T & Homma M (2001) Na(+)-driven flagellar motor of *Vibrio*. *Biochim Biophys Acta* 1505(1):82-93.
5. DeRosier DJ (1998) The turn of the screw: The bacterial flagellar motor. *Cell* 93(1):17-20.
6. Minamino T, Imae Y, Oosawa F, Kobayashi Y, & Oosawa K (2003) Effect of intracellular pH on rotational speed of bacterial flagellar motors. *J Bacteriol* 185(4):1190-1194.
7. Repaske DR & Adler J (1981) Change in intracellular pH of *Escherichia coli* mediates the chemotactic response to certain attractants and repellents. *J Bacteriol* 145(3):1196-1208.
8. Kihara M & Macnab RM (1981) Cytoplasmic pH mediates pH taxis and weak-acid repellent taxis of bacteria. *J Bacteriol* 145(3):1209-1221.
9. Morimoto YV, Che YS, Minamino T, & Namba K (2010) Proton-conductivity assay of plugged and unplugged MotA/B proton channel by cytoplasmic pHluorin expressed in *Salmonella*. *FEBS Lett* 584(6):1268-1272.
10. Miesenbock G, De Angelis DA, & Rothman JE (1998) Visualizing secretion and synaptic transmission with pH-sensitive green fluorescent proteins. *Nature* 394(6689):192-195.

11. Thomas JD, Daniel RA, Errington J, & Robinson C (2001) Export of active green fluorescent protein to the periplasm by the twin-arginine translocase (Tat) pathway in *Escherichia coli*. *Mol Microbiol* 39(1):47-53.
12. Martinez KA, Kitko RD, Mershon JP, Adcox HE, Malek KA, Berkmen MB, & Slonczewski JL (2012) Cytoplasmic pH response to acid stress in individual cells of *Escherichia coli* and *Bacillus subtilis* observed by fluorescence ratio imaging microscopy. *Applied and Environmental Microbiology* 78(10):3706-3714.
13. Krulwich TA, Sachs G, & Padan E (2011) Molecular aspects of bacterial pH sensing and homeostasis. *Nat Rev Microbiol* 9(5):330-343.
14. Morimoto YV, Kojima S, Namba K, & Minamino T (2011) M153R mutation in a pH-sensitive green fluorescent protein stabilizes its fusion proteins. *PLoS One* 6(5):e19598.
15. Morimoto YV, Kami-Ike N, Miyata T, Kawamoto A, Kato T, Namba K, & Minamino T (2016) High-resolution pH imaging of living bacterial cells to detect local pH differences. *MBio* 7(6):e01911-01916.
16. Ducret A, Quardokus EM, & Brun YV (2016) MicrobeJ, a tool for high throughput bacterial cell detection and quantitative analysis. *Nature Microbiology* 1(7):e16077.

# CHAPTER 6

## CHANGING CHEMOTAXIS SPECIFICITY OF *ESCHERICHIA COLI* BY INTRODUCING HETEROLOGOUS METHYL-ACCEPTING CHEMORECEPTORS

Detection of pollutants using chemotaxis-based biosensors requires the use of bacteria capable to target specific toxic compounds. In addition to the use of species naturally attracted by specific toxic molecules, we envisioned to modify chemotaxis specificity of *Escherichia coli* by introducing an additional chemoreceptor inducing chemotaxis towards a toxic molecule in another species. The advantage of this approach is the use of a well-known model strain, which is easy to manipulate in the laboratory. Therefore we introduced two different chemoreceptors into *E. coli*: McpT, a receptor for toluene from *Pseudomonas putida* MT53 and PcaY, a receptor for benzoate and other molecules originated from *P. putida* F1. Agarose plug assay showed a slight but statistically significant increase of chemotaxis response of the strain expressing McpT compared to the negative controls. The strains expressing PcaY receptor also showed chemotaxis to benzoate but this was similar as *E. coli* wild-type. We conclude that implementing heterologous chemoreceptors in *E. coli* is possible, but the factors determining correct incorporation into the existing chemotaxis network are poorly understood.



## Introduction

In the previous chapters (2-5), we focused on methods to quantify chemotaxis as readout for the development of rapid biosensors. Chemotaxis of *Escherichia coli* appears to be strong and highly reproducible with known and potent chemoattractants, such as serine or aspartate. Apart from the fact that the *E. coli* chemotaxis pathway has been intensively studied and that *E. coli* itself is easily genetically modifiable, it does not show chemotaxis towards molecules of potential interest for environmental monitoring. The use of another species that naturally swims in direction of a toxic molecule can replace *E. coli* in chemotaxis assays, but its response can be very different (see chapter 2) and the strain may be difficult to grow or to modify genetically. An alternative approach would be to modify *E. coli* to force it to respond to other molecules, by modification of the specificity of its receptors [1, 2] or by expression of other chemoreceptors. One important characteristic of methyl-accepting chemotaxis proteins (Mcp) and chemotaxis effector protein (e.g.: CheY) is their structural conservation among bacteria [3-5]. *E. coli* possesses four chemoreceptors but aquatic or soil bacteria frequently possess many more chemoreceptors. For example, *Pseudomonas* sp. can encode more than 20 methyl-accepting chemotaxis protein genes in their genomes [6, 7]. If these chemotaxis proteins are conserved enough among different species, one might be able to introduce new chemotactic specificity in *E. coli* by expressing heterologous chemoreceptors. This was already demonstrated by the expression of methyl-accepting chemotaxis protein from *Shewanella oneidensis* into *E. coli* to identify protein involved in energy taxis [8]. Also Aer-2 (a soluble receptor involved in aerotaxis) from *Pseudomonas aeruginosa* and PctApp (putative amino acid receptors) from *Pseudomonas putida* were shown to partially trigger chemotaxis response when expressed in *E. coli* [9, 10].

Numerous are the species that have been shown to be chemotactic to toxic molecules. A variety of strains have been tested for chemotaxis towards common pollutants, such as (poly-) aromatic hydrocarbons, with the idea to improve bioremediation capability [11-14].

Unfortunately, only a small number of receptors has actually been identified and characterized. Among them, the McpT receptor has been identified in *P. putida* DOT-T1E and is encoded on the self-transmissible pGRT1 plasmid, which gives the strain the ability to swim towards hydrocarbons such as toluene or naphthalene [15, 16]. The *mcpT* gene possesses 99.8% sequence similarity to coding sequences found in other *Pseudomonas* sp., such as on the TOL plasmid pWW53 of *P. putida* MT53 [16]. This strain was mentioned as a moderate chemotactic responder to toluene.

Further chemoreceptors have been characterized in *P. putida* F1. As an example, the PcaY receptor was shown to be involved in chemotaxis towards vanillate, vanillin, 4-hydroxybenzoate, benzoate, protocatechuate, quinate and shikimate [17]. These compounds are not particularly toxic but have the advantage to be water-soluble and non-volatile compared to aromatic molecules such as toluene.

The goal of this work was thus to modify chemotaxis specificity of *E. coli* towards toluene and benzoate, by expressing the *mcpT* gene from *P. putida* MT53 (pWW53) or the *pcaY* gene from *P. putida* F1 under the promoter of *trg* (gene coding for *E. coli* chemoreceptor for ribose and galactose). Chemotaxis was characterized by quantitative agarose plug assays. Localization of the expressed McpT receptor was assessed by constructing a protein fusion with mCherry.

## Results

### *Chemotactic response of E. coli expressing McpT receptor for toluene*

In order to create an *E. coli* strain chemotactic to toluene, we expressed the *mcpT* gene from plasmid pWW53 of *P. putida* MT53 under the control of the promoter of *trg* on a plasmid in *E. coli*. Since Trg is a minor chemoreceptor of *E. coli*, we expected a viable and controlled expression. In first instance, the *mcpT* gene was cloned under a low constitutive promoter ( $P_{AA}$ , see chapter 3) but the few viable transformants obtained always encoded a frameshift mutation in *mcpT* leading to a premature stop codon or a deletion. This suggests that a non-optimized expression of this membrane protein was deleterious for *E. coli*.

Chemotaxis towards toluene was tested by agarose plug assays [18]. In short: a toluene source was created in a droplet of agarose and a homogenous cell suspension was introduced all around the source. The bacteria accumulation close to the solid source was recorded by light microscopy after 15 min incubation. The strain expressing McpT accumulated close to the source with the  $10^{-3}$  toluene dilution (equivalent to 59  $\mu\text{M}$ ), less than in response to 100  $\mu\text{M}$  serine but higher than in response to a negative control source (without attractant). Accumulation was robust across multiple replicates and independent experiments (Fig. 1A). Variation in the strength of the response was more important with the toluene than with the serine source, which is likely due to the difficulties to prepare consistent sources with a volatile attractant. Higher concentrations of toluene (0.6 and 6 mM) did not induce a chemotactic response (Fig. 1A), but caused toxicity, even though the cells were still motile and able to swim close to the source (data not shown). With a tenfold lower toluene concentration (6  $\mu\text{M}$ ) no accumulation was detectable.

*E. coli* containing the empty plasmid pSTV28 but no *mcpT* showed a consistent response to 100  $\mu\text{M}$  serine but did not show any accumulation towards toluene (Fig. 1B). As second negative control, a frameshift mutation was introduced into the coding sequence of *mcpT*, which leads to a premature stop-codon. Similar to the *E. coli* carrying pSTV28, the strain carrying a

plasmid with the frameshifted *mcpT* gene did not display chemotactic response to toluene but accumulated near a serine source (Fig. 1C).

These results suggest that the expression of McpT from *P. putida* MT53 into *E. coli* MG1655 leads to a strain that shows chemotaxis towards toluene at  $\sim 60 \mu\text{M}$  source concentration. It also implies that the chemotaxis effector proteins (CheA, CheY, etc.) from *E. coli* are able to interact with a heterologous receptor.

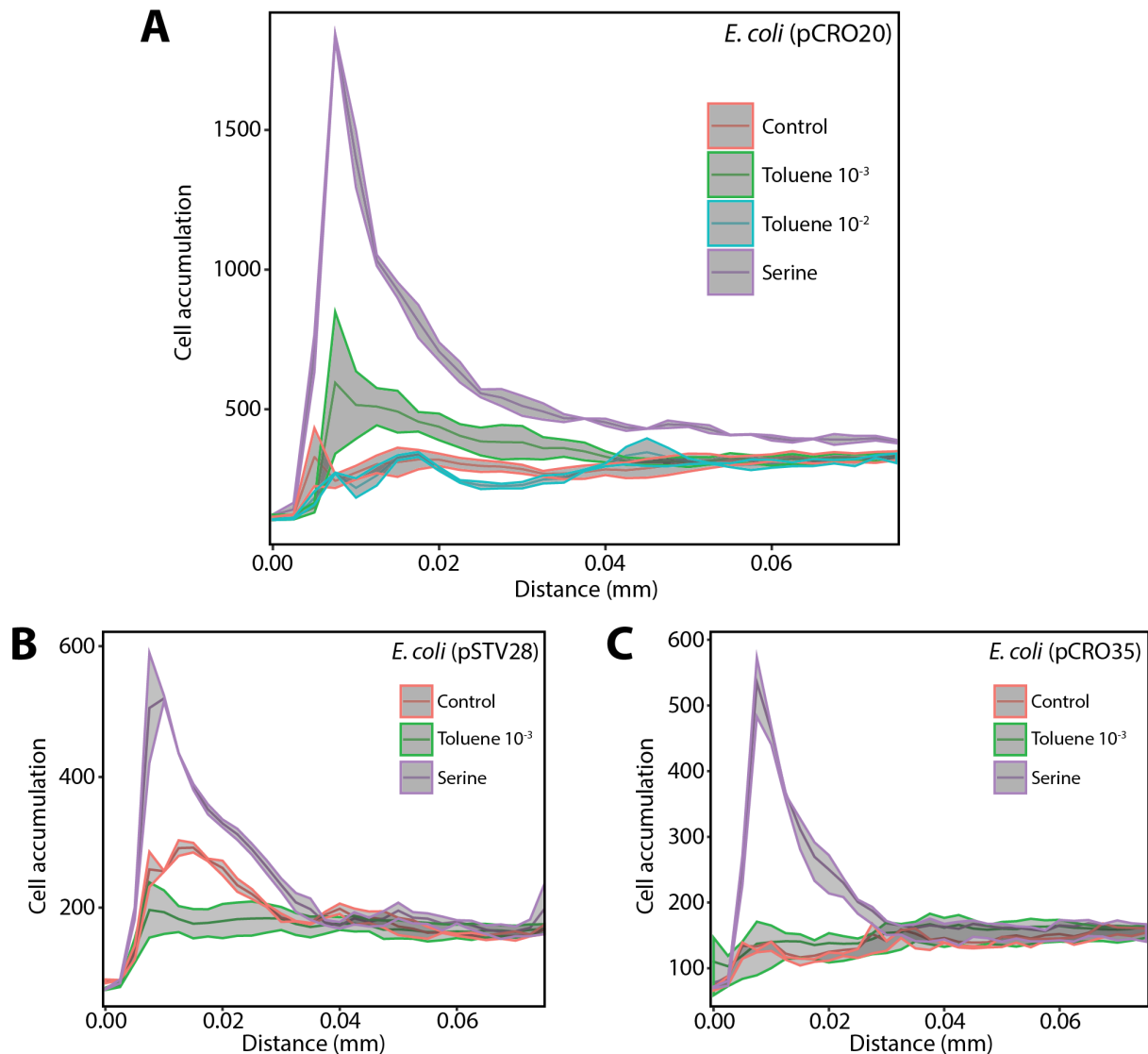


**Figure 1: Chemotaxis of *E. coli* expressing *mcpT* of *P. putida* towards toluene. (A)** Average cell accumulation as a function of distance from the source observed in four biological replicates imaged on both sides of the agarose plug with toluene ( $10^{-2}$   $\sim 590 \mu\text{M}$ , and  $10^{-3}$  dilution,  $\sim 59$

$\mu\text{M}$ ), serine (100  $\mu\text{M}$ ) or no attractant control with *E. coli* MG1566 (pCRO20) expressing the McpT receptor for toluene of *P. putida* MT53. **(B)** As (A) but with *E. coli* MG1655 (pSTV) (empty plasmid). **(C)** As (A) but with *E. coli* MG1655 (pCRO35), which contains a frameshift mutation in *mcpT* causing premature translation stop. Cell accumulation is displayed as the grey intensity of cell outlines on digital images. Ribbon traces show the average of four replicates  $\pm$  one standard deviation.

### *Expression of the McpT receptor in E. coli*

In order to demonstrate whether McpT is properly expressed in *E. coli* and localizes to the membrane, a protein fusion with mCherry was created and expressed under the  $P_{\text{trg}}$  promoter. Epifluorescence microscopy analysis showed that the cells expressing McpT-mCherry were more fluorescent than *E. coli* MG1655, MG1655 expressing McpT, or MG1655 expressing McpT-mCherry protein with a frameshift mutation in *mcpT* (Fig. 2A-B-D). McpT-mCherry fluorescence varied between individual cells (Fig. 2C). As a positive control, we expressed a Tsr-mCherry fusion protein from  $P_{\text{trg}}$  in MG1655, which yielded fluorescent cytoplasmic background and fluorescent foci near the poles and membranes, as expected for the localization of chemoreceptors (Fig. 2F) [19, 20]. A control expressing Tsr alone was not fluorescent (Fig. 2E). In contrast to Tsr-mCherry, therefore, expression of McpT-mCherry was more variable among individual cells and did not show fluorescent foci near poles or membranes (Fig. 2F).

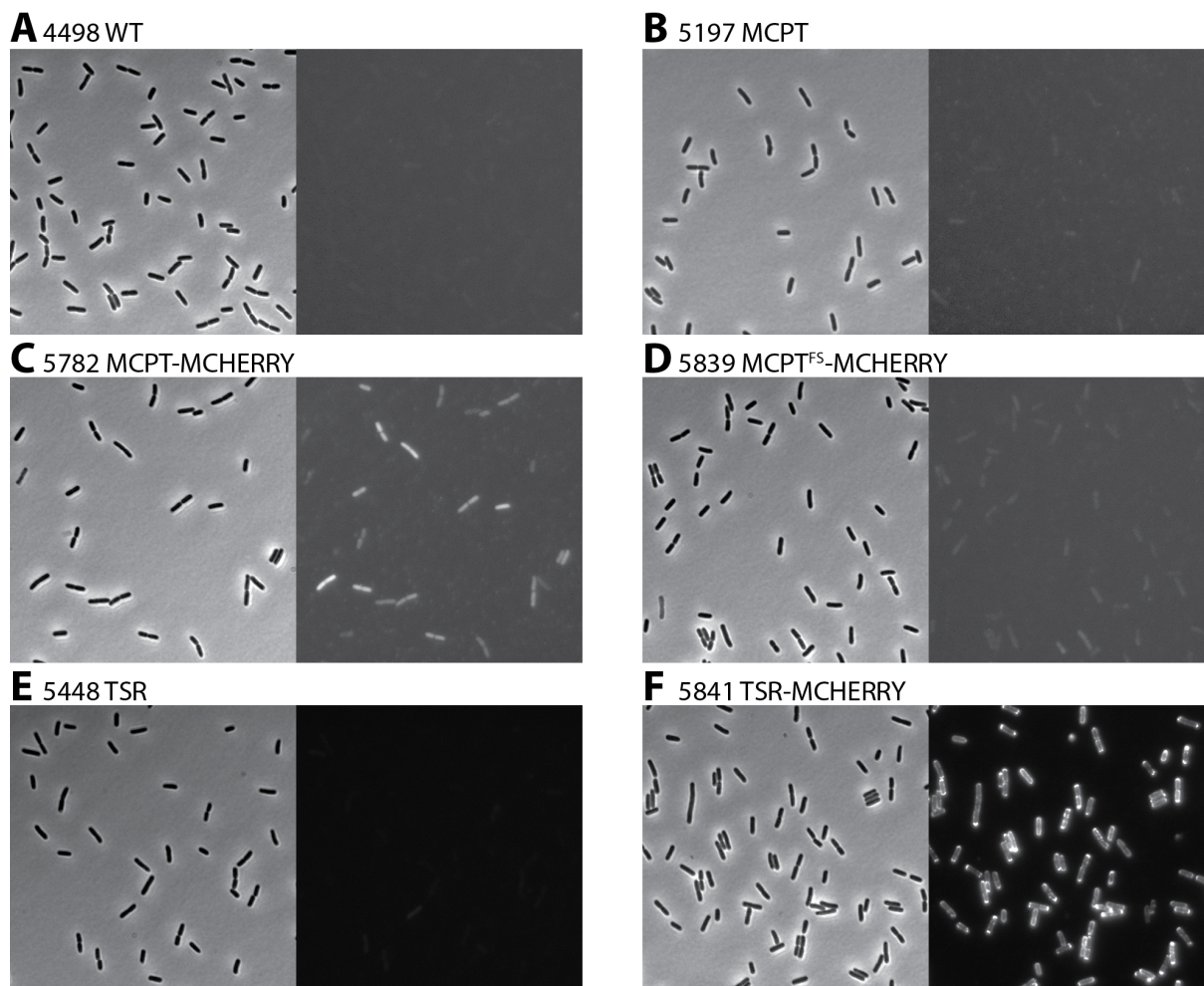


**Figure 2: Characterization of McpT receptor expression by fluorescent protein fusion.** Phase contrast and fluorescence images of **(A)** *E. coli* MG1655 (WT), **(B)** MG1655 + pCRO20 expressing McpT (MCPT), **(C)** MG1655 + pCRO36, expressing a fusion protein of McpT and mCherry (MCPT-MCHERRY), **(D)** MG1655 + pCRO37, expressing the fusion protein but with a frameshift mutation in *mcpT* coding sequence (MCPT<sup>FS</sup>-MCHERRY), **(E)** MG1655 + pCRO34, expressing Tsr receptor in the same conditions as McpT (TSR), **(F)** MG1566 + pCRO38, expressing a fusion protein of Tsr and mCherry (TSR-MCHERRY). Note that fluorescence images A-D and E-F were scaled differently for better visualization.

Fluorescence quantification of four independent replicate cultures showed a higher mean fluorescence of the strain expressing McpT-mCherry compared to the mutated fusion

protein or the wild type McpT (Fig. 3A). However, the variability between the replicates of the strain expressing McpT-mCherry was important, as evident from the large error bars (Fig. 3A). Different replicate cultures presented heterogeneity in fluorescence but also between the different cells in the population (Fig. 3B). The mutated McpT-mCherry showed less heterogeneity within the population and between the replicates (Fig. 3C).

These results suggest that the McpT-mCherry receptor is expressed in *E. coli* but at a lower level than Tsr-mCherry under the same conditions. The heterogeneity of expression between replicate cultures and between individual cells may indicate that expression is still not optimal for McpT in *E. coli*. Given the absence of McpT-mCherry foci, our results do not allow to conclude whether McpT is properly positioned in the membrane.

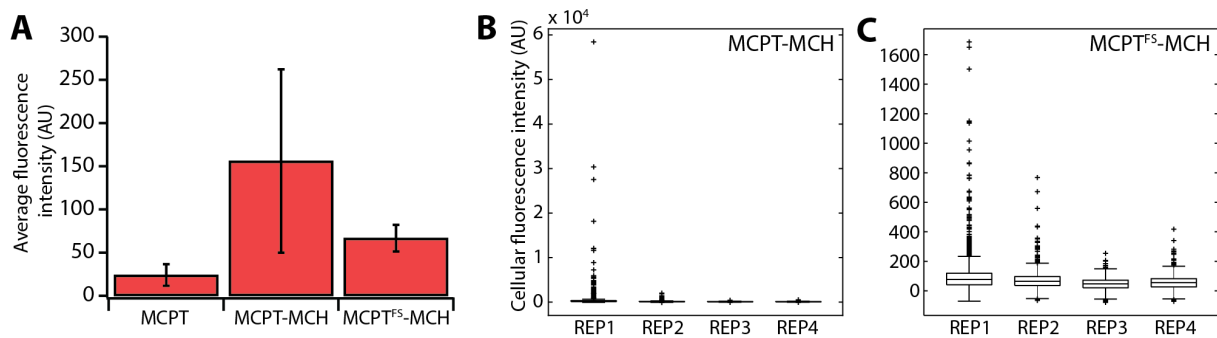


**Figure 3: Fluorescence intensity of *E. coli* expressing McpT.** (A) Average fluorescence intensity of 4 biological replicates of the strains expressing either MG1655 + pCRO20 expressing McpT receptor (MCPT), MG1655 + pCRO36, expressing a fusion protein of McpT and mCherry (MCPT-MCHERRY) or MG1655 + pCRO37, expressing the fusion protein but with a frameshift mutation in *mcpT* coding sequence (MCPT<sup>FS</sup>-MCHERRY) (B) Fluorescence intensity of individual cells of the four replicates of MG1655 + pCRO36 (C) Fluorescence intensity of individual cells of the four replicates of MG1655 + pCRO37. Note that the scales of the graphs are different.

*Chemotactic response of E. coli expressing the PcaY receptor for benzoate*

In addition to the McpT receptor for toluene, we also expressed in *E. coli* MG1655 the gene for the PcaY receptor from *P. putida* F1, which has been reported to induce chemotaxis to molecules such as vanillate, vanillin, 4-hydroxybenzoate, benzoate, protocatechuate, quinate and shikimate [17]. Chemotaxis was again quantified by agarose plug assays, but using sodium benzoate as attractant. *E. coli* MG1655 expressing PcaY showed cell accumulation close to the plug with a 1 mM source concentration of benzoate, which was lower than the response to the serine (Fig. 4A). A lower concentration of benzoate (0.1 mM) did not induce higher cell accumulation than the negative control without attractant (Fig. 4A). Furthermore, *E. coli* MG1655 containing the empty plasmid pSTV28 showed similar attraction to a source concentration of 1 mM benzoate (Fig. 4A).

This result suggests that *E. coli* MG1655 is already slightly attracted to benzoate even without any addition of a new chemoreceptor, and the effect of expressing PcaY cannot be distinguished.

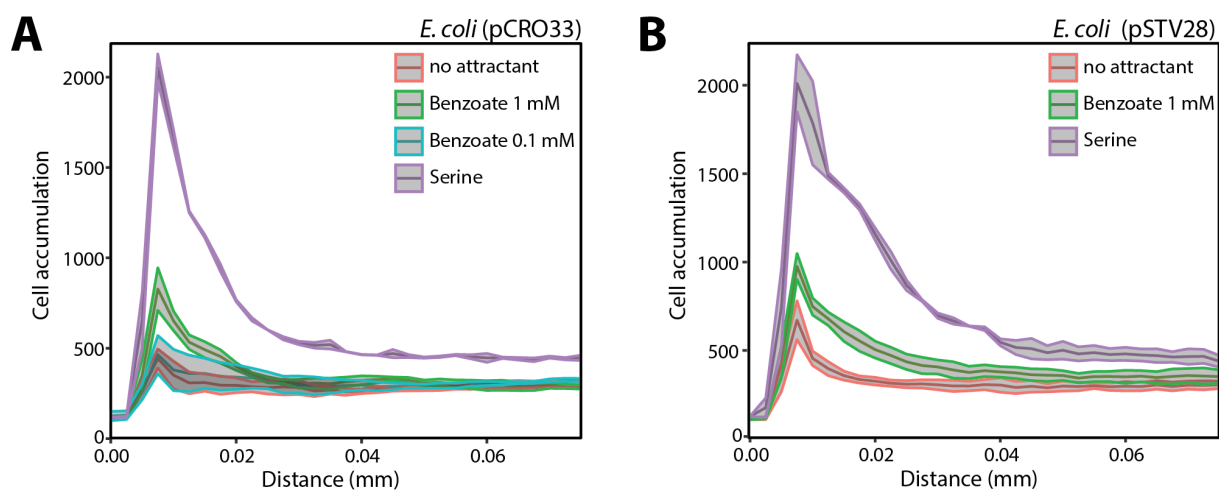


**Figure 4: Chemotaxis response of PcaY expressing *E. coli* MG1655. (A)** Cell accumulation as a function of distance to an agarose plug with benzoate (1 or 0.1 mM), serine (100  $\mu$ M) or no attractant of *E. coli* MG1566 (pCRO33) expressing the PcaY receptor for benzoate of *P. putida* F1. **(B)** As (A) for *E. coli* MG1566 (pSTV) (empty plasmid). Cell accumulation is displayed as the grey



intensity of cell outlines on digital images. Ribbon traces show the average from four independent replicates imaged at both sides of the agarose plug,  $\pm$  standard deviation.

## Discussion

Changing chemotaxis specificity in *E. coli* is an interesting approach for the development of chemotaxis-based biosensors, since *E. coli* chemotaxis is well understood and the strain is easy to modify genetically.

In this chapter, we studied whether introduction of heterologous chemoreceptor genes could produce *E. coli* attracted to toluene or benzoate. As source for the chemoreceptors we used different *P. putida* strains: McpT, a reported receptor for toluene and PcaY, a receptor for various molecules including benzoate. Our results indicated a significant response to toluene of the *E. coli* strain expressing the McpT receptor for toluene in comparison to controls (Fig. 1), whereas the chemotactic response to benzoate of *E. coli* expressing PcaY was not different from that of controls (Fig. 4).

Is the higher cell accumulation nearby a source of toluene (59  $\mu$ M) compared to a source without attractant evidence for genuine chemotactic response of *E. coli* expressing McpT to toluene? Control assays with *E. coli* carrying the empty plasmid or a mutated *mcpT* gene confirmed that the accumulation of *E. coli* McpT is specific. Furthermore, such cells are still chemotactic to serine, indicating that the general chemotaxis pathway is not impaired. Observing attraction to toluene is complicated by the technical difficulties to produce a solid source containing toluene, which is water insoluble and volatile. We could improve consistency by diluting small volumes of toluene liquid directly in agarose at 55°C inside completely filled and closed glass vials. Despite these precautions, chemotaxis response variation to toluene was more important than to serine.

The genuine chemotactic response of *E. coli* to toluene is further supported by visual expression of an McpT-mCherry fusion protein in individual cells, although we could not observe consistent fluorescent foci near the *E. coli* cell poles as in case of Tsr-mCherry (Fig. 2). McpT-mCherry fluorescence was quite variable among individual cells (Fig. 2) and between replicate cultures (Fig. 3), which suggests suboptimal expression and, consequently, variable chemotactic response to toluene. Expression of heterologous chemoreceptors in *E. coli* is delicate, since even

a low constitutive expression of the McpT receptor from  $P_{AA}$  was deleterious for the cells with reproducible selection of frameshift mutations or deletions. In contrast, the expression of McpT under the promoter of *trg*, the gene encoding a minor chemoreceptor of *E. coli*, led to a stable genetic construction without appearance of mutations. Despite this, individual cells with similar constructed  $P_{trg}$ -*mcpT*-*mCherry* on plasmid displayed important variability of McpT-mCherry fluorescence. Other heterologous receptors introduced in *E. coli* have been expressed from inducible promoters, such as *trc* promoter (IPTG inducible) or  $P_{sal}$ , a salicylate inducible promoter [8-10].

When assuming that McpT is correctly membrane incorporated in at least part of the cells, this would mean it is able to interact with cytoplasmic chemotaxis proteins such as CheA and CheY. One approach to confirm this interaction could be to tag CheA with a fluorescent protein and see its proper localization in an *E. coli* mutant devoid of all other chemoreceptors but expressing solely McpT. CheA was shown to localize at the cell poles in wild type *E. coli* (affirming its interaction with pole-localized chemoreceptors), but in the cytoplasm in mutants without any chemoreceptor [21]. This approach was followed to demonstrate proper expression of the *P. aeruginosa* PctApp receptor in an *E. coli* devoid of all naive receptors, in which case a YFP-CheZ fusion protein accumulated near the poles upon expression of PctApp [10]. These results would confirm expression and clustering of the heterologous receptors as well as efficient interactions with other proteins of chemotaxis pathway without modification of the receptor itself by protein fusion.

Contrary to our expectations, expression of PcaY from *P. putida* F1 into *E. coli* under control of the *trg* promoter, did not lead to a specific distinguishable chemotactic response to benzoate. Although *E. coli* cells expressing PcaY accumulated more on the border of a source of benzoate (1 mM) than on a source without any attractant, also *E. coli* containing only the empty plasmid accumulated similarly (Fig. 4). This suggests that *E. coli* MG1655 naturally displays a small positive chemotaxis towards benzoate. Sodium benzoate is a weak acid and has previously been shown to affect chemotaxis in *E. coli* and *Salmonella*, but rather acted as repellent [22]. This

was concluded from increased tumbling or repellent response of surface-tethered cells of *Salmonella* upon addition of 20 mM of sodium benzoate in a medium at pH 7 during 20 min [22]. Testing the effect of PcaY expression may be improved by using an *E. coli* mutant lacking all other chemoreceptors, or testing other possible chemoattractants reported for PcaY, such as vanillate, vanillin, 4-hydroxybenzoate, benzoate, protocatechuate, quinate and shikimate.

In conclusion, introducing new chemoreceptors into *E. coli* is an interesting approach for obtaining new chemotaxis functionalities, but proper receptor expression and functionality has to be tested case to case. Although agarose-plug assays are excellent for their simplicity, they do not necessarily show very weak chemotactic responses, and, in order to firmly demonstrate heterologous receptor functioning, alternative assays would be preferable. This may include producing hybrid receptors fusing ligand-binding domain of the heterologous chemoreceptor to the signaling domain of naive *E. coli* chemoreceptors [1, 2].

## Material and methods

### *Cloning procedures*

The gene for the methyl-accepting chemotaxis receptor (*mcpT*) was amplified from *P. putida* MT53 pWW53 (strain 1127 in our collection) genomic DNA using a Q5 proofreading polymerase and primers 141001 and 141002 (Table 2). The forward primer 141001 contained a BamHI restriction site and reverse primer 141002 was elongated with a ClaI restriction site (Table 2). The PCR fragment was cloned into pGEM-t-Easy® (Promega) and the insert was verified by sequencing. The promoter of *E. coli* chemoreceptor Trg ( $P_{\text{trg}}$ ) was amplified from *E. coli* MG1655 genomic DNA (strain 4498 in our collection) using a Q5 proofreading polymerase and primers 150613 and 150612, elongated with BamHI and SacI restriction sites, and with a N-terminal part of *mcpT* until NheI site (17 bp), respectively.  $P_{\text{trg}}$  was inserted upstream of the *mcpT* sequence in pGEM-t-Easy® by digestion with BamHI and NheI because *mcpT* contains an NheI site 12 nucleotides downstream of its start codon. The correct sequence was finally inserted into pSTV28 by digestion with SacI and ClaI and the plasmid was renamed pCRO20 (Table 1). This plasmid was inserted into a motility-positive strain of *E. coli* MG1655 (*E. coli* Genetic Center, Yale (CGSC#8237) and strain 4498 in our collection).

A frameshift mutation was introduced in *mcpT* to disrupt the coding sequence, by digestion of pCRO20 with NsiI, removal of the 3'-overhang with T4 DNA polymerase (New England Biolabs) treatment of 20 min at 12 °C and recircularization of the plasmid with T4 DNA ligase. This plasmid was renamed pCRO35 (Table 1).

The *mcp-mcherry* fusion was produced by amplification of a '*linker-mcherry*' fragment from plasmid pBAM-link-mcherry [23] using 170239 and 170240 elongated with a BglII restriction site and the C-terminal part of *mcpT* until the MfeI site, respectively (Table 2). The '*link-mcherry*' fragment was inserted in pCRO20 by digestion with BglII and MfeI. This plasmid was renamed pCRO36 (Table 1).

The receptor PcaY from *P. putida* F1 was also cloned under the control of P<sub>trg</sub> promoter. Here its coding sequence *Pput2149* was amplified from *P. putida* F1 genomic DNA using primers 160306 and 160307, as well as the promoter P<sub>trg</sub> using primers 150613 and 160305 (Table 2). Both PCR fragments were fused by sewing PCR and cloned back into pSTV28 by digestion with SacI and ClaI. This plasmid was renamed pCRO33 (Table 1).

The same cloning strategy was used for cloning of the Tsr receptor gene from *E. coli* MG1655 as control. The *tsr* coding sequence was amplified from *E. coli* MG1655 genomic DNA using primer 160309 and 160310 and P<sub>trg</sub> was amplified using primers 150613 and 160308 (Table 2). Both fragments were fused by sewing PCR and subcloned into pGEM-t-Easy®. The whole sequence was introduced into pSTV28 backbone by digestion with SacI and PstI (localized in pGEM-t-Easy®). This plasmid was renamed pCRO34 (Table 1).

A *tsr-mcherry* fusion was produced by amplification of the '*link-mcherry*' fragment from pBAM-link-mcherry using 101003 and 101004 and a '*P<sub>trg</sub>-tsr*' fragment from pCRO34 using primers 070418 and 160308 (Table 2). Both fragments were fused by sewing PCR, subcloned into pGEM-t-Easy® and cloned back into pCRO34 by digestion with SacI and SpeI. This plasmid was renamed pCRO38 (Table 1).

### *Agarose plug assays*

*E. coli* strains were grown overnight in M9-Glc (see Chapter 2) supplemented with 30 µg ml<sup>-1</sup> of chloramphenicol (Cm30). The cultures were diluted 100-fold in fresh M9-Glc-Cm30 and incubated for 3 hours at 37°C with 180 rpm shaking until they reached exponential phase (OD<sub>600</sub> ~0.5-0.6). One milliliter of culture was centrifuged at 2,400 × g for 5 min, washed two times with 1 mL of chemotaxis buffer (see Chapter 2) and resuspended in 500 µl of chemotaxis buffer, which corresponds to a density of ~10<sup>9</sup> cells ml<sup>-1</sup>.

To prepare the source of toluene, 1.8 % of agarose (LE, Analytical grade, PROMEGA) was prepared in tap water and kept at 55°C. 2 ml glass vials with Teflon-lined screw-cap (Supelco Analytical) were filled with 1.6 ml of melted 55°C-warm agarose solution, into which was

dissolved 10  $\mu\text{l}$  of pure toluene. The toluene density is  $0.87 \text{ g mL}^{-1}$  and its molecular mass is  $92.14 \text{ g mol}^{-1}$ ; therefore, adding 10  $\mu\text{l}$  toluene to 1.6 ml volume is equivalent to  $8.7 \text{ mg}/1.6 \text{ ml} = 5.4 \text{ mg mL}^{-1}$  or  $0.059 \text{ mmol mL}^{-1} = 59 \text{ mM}$ . Toluene was serially diluted in prewarmed agarose by adding 0.15 ml of the agarose with the pure toluene source into 1.4 ml of  $55^\circ\text{C}$ -warm agarose solutions, and from there to further agarose solutions. The  $10^{-3}$  dilution is thus equivalent to  $0.059 \text{ mM}$  or  $59 \mu\text{M}$ . As positive control, 1.4 ml of 2% agarose solution at  $55^\circ\text{C}$  was supplemented with 0.15 ml of 1 mM serine solution in water (final concentration =  $100 \mu\text{M}$ ). The negative control consisted of 1.8% agarose solution in tap water.

Sources of benzoate were prepared by 100-fold dilution of a 1 M sodium benzoate stock in 1.8 %  $55^\circ\text{C}$  warm agarose (1.6 ml agarose with 16  $\mu\text{l}$  of 1 M benzoate), which corresponds to a concentration of 10 mM benzoate. From here, benzoate was serially diluted to obtain stocks of 1 and 0.1 mM in 1.8 % agarose. All vials were kept tightly closed in a water bath at  $55^\circ\text{C}$  until preparing the plug assays. Agarose solutions were prepared fresh for every experiment. Toluene attraction assays were repeated in fourfold replicates in series with positive (serine) and negative controls. They were further repeated on at least four independent occasions.

On a standard microscopy glass slide (Menzel Gläser, Thermo Scientific), two small coverslips ( $24 \times 24 \text{ mm}$ , 0.13-0.17 mm thick, MGF-Slides) were deposited on both sides and maintained in place with  $\sim 10 \mu\text{l}$  of tap water. A drop of 4  $\mu\text{l}$  of  $55^\circ\text{C}$  agarose solution was deposited in the middle and immediately covered by a cleaned large coverslip ( $24 \times 50 \text{ mm}$ , Menzel Gläser) that bridges over the side coverslips and thus creates a chamber with a height of 0.17 mm. A freshly grown and washed bacterial suspension in chemotaxis buffer was inserted around the agarose plug by pipetting 150  $\mu\text{l}$  of cell suspension between the glass slide and the large coverslip.

Bacterial accumulation was imaged after 15 min incubation at room temperature ( $20 \pm 2^\circ\text{C}$ ) using a DFC 350 FX R2 Leica camera mounted on an inverted DMI 4000 Leica microscope using a N PLAN 10X objective. For each replicate, one image was taken at each side of the agarose plug. Images were analyzed with ImageJ software. Cells were identified using the “find edges” routine in ImageJ and the accumulated intensity values were quantified per zones of 25 pixels width

parallel to the plug border (3 zones in the plug and 27 zones outside the plug). Chemotactic responses were then averaged from four technical replicates (e.g., as in Fig. 1 and 4).

### *Epifluorescence microscopy of fusion proteins*

For epifluorescence microscopy experiments, strains were grown with the same protocol as for the agarose plug assay. Cells were resuspended in 50  $\mu$ l of chemotaxis buffer after the washing steps. A drop of 7  $\mu$ l of cell suspension was spotted on a 1 % agarose (in chemotaxis buffer) coated microscopy slide and then covered with a regular 0.17-mm thick glass coverslip. Cells were imaged at an exposure time of 50 ms (phase-contrast) or 1 s (mCherry) with a Nikon Eclipse Ti-E inverted microscope, equipped with an ORCA-flah4.0 camera (Hamamatsu) and a Plan Apo  $\lambda$  100 $\times$ 1.45 oil objective (Nikon).

Cell fluorescence intensities were extracted from the images using an in-house written Matlab (R2015b) script (developed by Serge Pelet, University of Lausanne).



**Table 1: strain list**

Strain n°	Host	Plasmid	Relevant characteristics	Source of reference
1127	<i>P. putida</i> MT53 (pWW53)		Non-motile stock	[24]
4498	<i>E. coli</i> MG1655		Verified for motility	<i>E. coli</i> Genetic Center, Yale (CGSC#8237)
5186	<i>E. coli</i> DH5 $\alpha$	pGEM-t-Easy- P <sub>trg</sub> -mcp		This study
5197	<i>E. coli</i> MG1655	pCRO20	McpT expressing strain under P <sub>trg</sub> promoter	This study
5775	<i>E. coli</i> MG1655	pCRO35	Frameshift mutation in <i>mcpT</i> coding sequence	This study
3396	<i>E. coli</i> DH5 $\alpha$	pBAM-link- mcherry		[23]
5782	<i>E. coli</i> MG1655	pCRO36	Protein fusion of McpT with mCherry	This study
5839	<i>E. coli</i> MG1655	pCRO37	Frameshift mutation in <i>mcp-mcherry</i>	This study
5447	<i>E. coli</i> MG1655	pCRO33	Strain expressing PcaY from P <sub>trg</sub> promoter	This study
5448	<i>E. coli</i> MG1655	pCRO34	Strain expressing Tsr from P <sub>trg</sub> promoter	This study
5841	<i>E. coli</i> MG1655	pCRO38	Protein fusion of Tsr with mCherry	This study
5457	<i>E. coli</i> MG1655	pSTV28	Empty plasmid	Takara, Japan (nr. 3331)

**Table 2: primer list**

Primer number	Sequence (5' - 3') <sup>1</sup>	Primer specificities	Amplification target
141001	TGGATCCTCTAGAAATAATTTTGTTTAACT TTAAGAAGGAGATATACATATGAGTGGTTG GCTAGCCCGTTTCTCAATAAAAACC	BamHI restriction site	<i>mcpT</i> from <i>P.putida</i> MT53
141002	ATTGGCAACGGTCAGCTTTATCGATGGAGA TCTCACTAAAGACGGAACATGTGCATCAGA CGCTGAA	Clal restriction site	<i>mcpT</i> from <i>P.putida</i> MT53
150613	AGGATCCTCTGAGCTCCGGTTAGCCTGAAA ACAG	BamHI and SacI restriction sites	P <sub>trg</sub> from <i>E. coli</i> MG1655
150612	<i>GGCTAGCCAACCACTCATTACCGTTGTCTCT</i> CGTCCAGGTTTACTCC	N-terminal part of <i>mcpT</i> until NheI restriction site (in italic)	P <sub>trg</sub> from <i>E. coli</i> MG1655, specific for <i>mcpT</i> cloning
170239	TTTTTAGATCTTTATTTGTACAGCTCATCC ATGCC	BglII restriction site	<i>Linker-mcherry</i> to fuse with <i>mcpT</i>
170240	CGCAATTGGCTTCTCTGGCAAGCCAACTTC AGCGTCTGATGCACATGTTCCGTCTTAAGC TTCCGGAAAATTCGAACG	C-terminal part of <i>mcpT</i> until MfeI restriction site	<i>Linker-mcherry</i> to fuse with <i>mcpT</i>
160305	GAATTTTCAGGTTGGCAAGCATTACCGTTGT CTCTCGTCCAGGTTTACTCC	Overlapping sequence with N-terminal part of <i>pcaY</i> (in italic)	P <sub>trg</sub> from <i>E. coli</i> MG1655, specific for <i>pcaY</i> cloning
160306	ATGCTTGCCAACCTGAAAATTCGCACC	N-terminal part of <i>pcaY</i>	<i>pcaY</i> from <i>P. putida</i> F1
160307	CATCGATTCATCAAACCTTGAACCGCCCCA CCAACG	Clal restriction site	<i>pcaY</i> from <i>P. putida</i> F1

160308	CAATTTTGATACGTTTTAACATTACCGTTGT CTCTCGTCCAGGTTTACTCC	Overlapping sequence with N- terminal part of <i>tsr</i> (in italic)	P <sub>trg</sub> from <i>E. coli</i> MG1655, specific for <i>tsr</i> cloning
160309	ATGTTAAAACGTATCAAAATTGTGACC	N-terminal part of <i>tsr</i>	<i>tsr</i> from <i>E. coli</i> MG1655
160310	CATCGATTCATTTAAAATGTTTCCCAGTTCT CC		<i>tsr</i> from <i>E. coli</i> MG1655
101003	GGGGAAGCTTCCGGAAAATTCGAACGTTAC GCGTCACCGGTCGGCCACCGTTTCCAAGGGC GAGGAGG		<i>Linker-mcherry</i> to fuse with <i>tsr</i>
101004	GGG <b>ACTAG</b> TTTATTTGTACAGTCATCCA TGCC	SpeI restriction site	<i>Linker-mcherry</i> to fuse with <i>tsr</i>
070418	CAGGAAACAGCTATGACC		P <sub>trg-<i>tsr</i></sub> from pCRO34

<sup>1</sup> Restriction sites highlighted in bold

## Acknowledgements

I want to thank Jan Roelof van der Meer for his help for the high throughput agarose plug production and analysis of the microscopy images. I thank Lionel Di Santo who started this project during his short-term master project and Estelle Clerc who worked on the development of a proper way to create a source of toluene and who constructed some of the strains used here (5447, 5448, 5457). I am also grateful for Serge Pelet who developed Matlab scripts for image analysis.

## References

1. Bi SY, Pollard AM, Yang YL, Jin F, & Sourjik V (2016) Engineering hybrid chemotaxis receptors in bacteria. *Acs Synthetic Biology* 5(9):989-1001.
2. Derr P, Boder E, & Goulian M (2006) Changing the specificity of a bacterial chemoreceptor. *J Mol Biol* 355(5):923-932.
3. Alexander RP & Zhulin IB (2007) Evolutionary genomics reveals conserved structural determinants of signaling and adaptation in microbial chemoreceptors. *Proc Natl Acad Sci U S A* 104(8):2885-2890.
4. Lacal J, Garcia-Fontana C, Munoz-Martinez F, Ramos JL, & Krell T (2010) Sensing of environmental signals: classification of chemoreceptors according to the size of their ligand binding regions. *Environ Microbiol* 12(11):2873-2884.
5. Szurmant H & Ordal GW (2004) Diversity in chemotaxis mechanisms among the bacteria and archaea. *Microbiol Mol Biol Rev* 68(2):301-319.
6. Hazelbauer GL, Falke JJ, & Parkinson JS (2008) Bacterial chemoreceptors: high-performance signaling in networked arrays. *Trends Biochem Sci* 33(1):9-19.
7. Sampedro I, Parales RE, Krell T, & Hill JE (2015) *Pseudomonas* chemotaxis. *FEMS Microbiol Rev* 39(1):17-46.
8. Baraquet C, Theraulaz L, Iobbi-Nivol C, Mejean V, & Jourlin-Castelli C (2009) Unexpected chemoreceptors mediate energy taxis towards electron acceptors in *Shewanella oneidensis*. *Mol Microbiol* 73(2):278-290.
9. Watts KJ, Taylor BL, & Johnson MS (2011) PAS/poly-HAMP signalling in Aer-2, a soluble haem-based sensor. *Mol Microbiol* 79(3):686-699.
10. Herrera Seitz MK, Soto D, & Studdert CA (2012) A chemoreceptor from *Pseudomonas putida* forms active signalling complexes in *Escherichia coli*. *Microbiology* 158(Pt 9):2283-2292.

11. Parales RE & Harwood CS (2002) Bacterial chemotaxis to pollutants and plant-derived aromatic molecules. *Curr Opin Microbiol* 5(3):266-273.
12. Krell T, Lacal J, Reyes-Darias JA, Jimenez-Sanchez C, Sungthong R, & Ortega-Calvo JJ (2013) Bioavailability of pollutants and chemotaxis. *Curr Opin Biotechnol* 24(3):451-456.
13. Pandey G & Jain RK (2002) Bacterial chemotaxis toward environmental pollutants: role in bioremediation. *Appl Environ Microbiol* 68(12):5789-5795.
14. Parales RE, Luu RA, Hughes JG, & Ditty JL (2015) Bacterial chemotaxis to xenobiotic chemicals and naturally-occurring analogs. *Curr Opin Biotechnol* 33:318-326.
15. Molina L, Duque E, Gomez MJ, Krell T, Lacal J, Garcia-Puente A, Garcia V, Matilla MA, Ramos JL, & Segura A (2011) The pGRT1 plasmid of *Pseudomonas putida* DOT-T1E encodes functions relevant for survival under harsh conditions in the environment. *Environ Microbiol* 13(8):2315-2327.
16. Lacal J, Munoz-Martinez F, Reyes-Darias JA, Duque E, Matilla M, Segura A, Calvo JJ, Jimenez-Sanchez C, Krell T, & Ramos JL (2011) Bacterial chemotaxis towards aromatic hydrocarbons in *Pseudomonas*. *Environ Microbiol* 13(7):1733-1744.
17. Luu RA, Kootstra JD, Nesteryuk V, Brunton CN, Parales JV, Ditty JL, & Parales RE (2015) Integration of chemotaxis, transport and catabolism in *Pseudomonas putida* and identification of the aromatic acid chemoreceptor PcaY. *Mol Microbiol* 96(1):134-147.
18. Yu HS & Alam M (1997) An agarose-in-plug bridge method to study chemotaxis in the Archaeon *Halobacterium salinarum*. *FEMS Microbiol Lett* 156(2):265-269.
19. Ping L, Weiner B, & Kleckner N (2008) Tsr-GFP accumulates linearly with time at cell poles, and can be used to differentiate 'old' versus 'new' poles, in *Escherichia coli*. *Mol Microbiol* 69(6):1427-1438.
20. Shiomi D, Banno S, Homma M, & Kawagishi I (2005) Stabilization of polar localization of a chemoreceptor via its covalent modifications and its communication with a different chemoreceptor. *J Bacteriol* 187(22):7647-7654.

21. Sourjik V & Berg HC (2000) Localization of components of the chemotaxis machinery of *Escherichia coli* using fluorescent protein fusions. *Mol Microbiol* 37(4):740-751.
22. Kihara M & Macnab RM (1981) Cytoplasmic pH mediates pH taxis and weak-acid repellent taxis of bacteria. *J Bacteriol* 145(3):1209-1221.
23. Miyazaki R, Minoia M, Pradervand N, Sulser S, Reinhard F, & van der Meer JR (2012) Cellular variability of RpoS expression underlies subpopulation activation of an integrative and conjugative element. *PLoS Genet* 8(7):e1002818.
24. Keil H, Keil S, Pickup RW, & Williams PA (1985) Evolutionary conservation of genes coding for meta pathway enzymes within TOL plasmids pWW0 and pWW53. *J Bacteriol* 164(2):887-895.



# **CHAPTER 7**

## **GENERAL DISCUSSION**



## **Microfluidics at the service of chemotaxis quantification**

The aim of this thesis was to find, based on chemotaxis, a new way to decrease the time response of whole-cell bacterial bioreporters.

As first approach, we attempted to measure cellular motility as a proxy of chemotaxis pathway activation. This is a straightforward measurement since we measure the final output of chemotaxis: the biased random swimming. Multiple methods have been developed, such as swimming plates, capillary assays or agarose plug assays in order to describe bacterial chemotaxis. However, most of these methods require time and/or are poorly quantitative (although we tried to improve quantification using the agarose plug assay, see Chapter 6). Micro-scaled gradients can be generated within 20-30 min using microfluidic devices and can be easily abolished and re-established [1-4]. Microfluidic devices had already been developed in order to describe bacterial chemotaxis response [4], but those studies did not focus on the quantification of the attractant concentration using chemotaxis in an environmental perspective.

For this thesis, we developed two microfluidic chips, in which we can generate a gradient thanks to diffusion between a source of attractant and a sink, physically separated by microchannel filters (Chapter 2) or by pressure-driven valves (Chapter 3). Motile bacteria were inserted in the gradient and chemotaxis was quantified either at population level (Chapter 2) or at single-cell level (Chapter 3). We successfully quantified population-level chemotaxis of *Escherichia coli* towards well-known chemoattractants such as serine, aspartate and methylaspartate, as well as quantify the response of *Cupriavidus pinatubonensis* JMP134 towards a herbicide, the 2,4-dichlorophenoxyacetate (Chapter 2). These results show that bacterial cellular motility is a promising readout for bacterial bioreporters. It is a direct measurement of chemotaxis and can be performed with any wild-type culturable bacteria. In our study, we detected bacterial accumulation on the basis of fluorescence signals from tagged bacteria by epifluorescence microscopy. However, it should be possible to detect cellular accumulation near the source borders by light scattering. This would facilitate the detection of the chemotactic response and prevent the need for genetically modified strains.

Interestingly, *E. coli* chemotactic accumulation to serine in the PDMS chip did not show a typical S-shape response as function of serine concentration, but rather a bell-shaped response with an optimum of highest cellular accumulation at 100  $\mu$ M. Most of the bacterial bioreporters developed show a small range of linear or semi-linear response to increasing target concentration, above which the response saturates or diminishes as a result of compound toxicity [5]. The response range is then used as a calibration curve for the reaction to samples with unknown target compound concentration. It is not impossible to use a bell-shape chemotaxis response curve for inferring the target compound concentration in unknown samples, but it is more challenging, because one would have to include sample dilutions in order to decide on which 'side' of the response curve (ascending or descending) one is. Alternatively, one might think of deploying chemotaxis biosensors for ON/OFF signaling. If the cells accumulate in presence of a pollutant, this triggers an alarm signal. This could be used as a first warning system that would detect pollution without determination of the exact concentration to which the cells were exposed. This concept would require rather precise chemotaxis pathway tuning so that the optimal response concentration corresponds to the warning threshold level. As for every newly designed whole cell bioreporter, calibration of the system is a crucial aspect for potential biosensing applications.

Microfluidics is an interesting tool to decrease the observation scale of biological processes and facilitate their integration in miniaturized devices. Microfluidic chips, however, require robust and precise control of the flow. We improved flow control on the first-designed chip from Chapter 2 by addition of pressure-driven valves inside the PDMS structure (Chapter 3). This indeed drastically facilitated the control of the flow since it can be easily stopped by the closure of the valves. Better flow control permitted to follow the behavior of single swimming cells in the created chemical gradients on the chip. In contrast, the results were inconclusive as to those cells being attracted or not to serine and we did not have sufficient time to explore this further. Mathematical modeling of single cell chemotactic behavior suggested some modifications to the set up which might improve the detection of attraction, such as increased

incubation time, increased cell numbers and inlet placement closer to the source. We realized how important the combination of mathematical modeling and collaborative work with physicians is, to guide the design of the chip structure and suggest improvements of the devices. Improvements on the current design might allow chemotaxis quantification within few minutes after cells are exposed to a gradient of attractant, which would decrease significantly the time required to observe and quantify chemotaxis at cellular motility level.

Our developed tools may be used for other fields of the biological research, such as studies on polarized cell growth (neurons, yeast...), leucocyte or other cell-type chemotaxis, cell-to-cell communication or host-pathogen interaction/communication that need devices that generate artificial gradients [6]. Notably, our valve-integrated microfluidic chip could be used for screening for chemotaxis-responsive strains to new molecules or other screening (cell sorting). One can imagine inserting a bacterial community (or a library) and inducing a “bacterial race” towards a molecule of interest and then to sort out the responsive strains by opening the valve close to the source when the first cells reach it.

### **Quantification of chemotaxis pathway activation**

The second approach of my project was to exploit parts of the molecular pathway of chemotaxis for biosensing. On the one hand we measured protein-protein interaction between CheY and CheZ using bimolecular fluorescence complementation (Chapter 4). The other approach consisted of inferring the proton flux during chemotactic attraction using a pH-sensitive fluorescent protein (Chapter 5).

The measurement of the interaction between CheY and CheZ by a split-Gfp approach allowed us to localize of the interaction between these two proteins at subcellular level. Interestingly our mutant analysis showed that this interaction takes place mostly at the motors and less at the receptors, which was unexpected given that previous studies indicated CheY and CheZ mostly localize at the receptor. It would be interesting to widen the analysis with other

mutants (e.g.: mutant lacking all receptors) in order to better understand how and where this interaction takes place.

In general, bimolecular fluorescence complementation assays using split-Gfp are simple tools to visualize and localize protein-protein interactions and we demonstrated that this system could show an increase in the turnover of the protein interaction upon addition of repellent. Unfortunately we realized that the stability of the Gfp prevents the measurement of a decrease of interaction upon exposure to an attractant. The use of dimerization-dependent fluorescent proteins (ddFP) [7, 8] or fluorescence/bioluminescence resonance energy transfer (FRET or BRET) methods might increase the measurement dynamics [9, 10]. BRET measurement is a promising approach to develop biosensors. Thanks to the energy transfer from the Luciferase to a Yellow fluorescent protein (Yfp), there is, in principle, no need of light excitation if the signal is strong enough and may be more easy to set up in comparison to existing FRET approaches.

We also exploited the flagellar properties with the idea to quantify chemotaxis from pH changes (Chapter 5). Since the flagella are powered by an influx of protons, the idea was to measure potential pH differences inside the cells due to the rotational change of the flagella in presence of an attractant. We expressed the pHluorin protein in the cytoplasm and in the periplasm, both of which were robust indicators to the change of pH. In contrast to our initial hypothesis, we measured a pH increase in the cytoplasm and a decrease in the periplasm in chemotaxis-active cells, which suggests an active export of the protons to the outside of the cells, probably to compensate the necessary proton flux through the flagella. One hypothesis could be that this pH efflux is due to an increase in the respiration rate. Is this specific to *E. coli*? Notably *Rhodobacter sphaeroides* possesses a unidirectional flagellum that stops instead of switching rotational direction, such as with *E. coli* [11]. The *R. sphaeroides* motor is also powered by a flux of proton through the membrane. It would be interesting to investigate whether pH would also increase in the cytoplasm during chemotaxis of *R. sphaeroides*.

***Escherichia coli* as chassis for chemotaxis assays**

*E. coli* is the most studied bacterial species for its chemotaxis response. We showed that it strongly and robustly responds to serine at 100  $\mu\text{M}$  in microfluidic chips as well as with agarose plug assays. But is this species the optimal bacterium for chemotaxis-based biosensors development? Of course, it is well known and responds strongly but it is not very sensitive (1-10  $\mu\text{M}$  serine are needed) nor an extremely fast swimmer. Other marine bacterial species swim much faster than *E. coli* and since they are adapted to a low carbon content environment, they are able to detect and swim towards low and transient burst of food more efficiently [12, 13]. For this reason it may be interesting to test other natural chemotactic bacteria in the same microfluidic chips and define the lower gradient thresholds at which cells measurably show chemotaxis.

The advantage of using *E. coli* is for genetic engineering. Synthetic bioreporters based on chemotaxis molecular pathway can be easily engineered using *E. coli* as chassis. However, *E. coli* is not naturally attracted to toxic molecules (i.e., compounds of environmental interest). We showed that a chemoreceptor for toluene originating from *Pseudomonas putida* can be expressed in *E. coli* and can induce a chemotaxis response towards toluene (Chapter 6). This was surprising but shows that the signaling from the toluene-receptor must be sufficiently conserved to link to *E. coli*'s CheY and motors. Likely, the expression of the toluene-receptor is not (yet) completely optimal, because we could not detect membrane localization like for Tsr. In principle, however, *E. coli* expressing heterologous receptors could be used in the microfluidic device of Chapter 2 as sensors for environmentally relevant compounds. (Of note that PDMS is not the best material to use in combination with aqueous samples containing organic solvents such as toluene, because this will dissolve into the PDMS and will reduce the bioavailable concentration). The chemotaxis system of *E. coli* could be further used as a modular unit, for example, by modifying the ligand specificity of *E. coli* periplasmic binding protein that can dock to chemoreceptors [14, 15] or to create chimeric chemoreceptors from heterologous ligand-binding domains fused to conserved signaling domains of *E. coli* [16]. One can also think about

fishing in the natural pool of motile bacteria by designing traps to isolate new strains chemotactic to molecule of environmental interest, which receptors might then be expressed in *E. coli* [17, 18]. This would increase the range of potential target compounds for chemotaxis-based biosensors.

## **Conclusion**

To conclude chemotaxis is an interesting behavior to base the development of new bacterial bioreporters, thanks to its fast response but also thanks to the adaptation feedback. Indeed bacteria react transiently to a sudden increase of attractant/repellent until they adapt. This response allows the development of reversible bioreporters that can be used multiple consecutive times because bacteria intrinsically and rapidly reinitialize their response. This is in contrast to transcription-based bioreporters, which require time to degrade the induced reporter proteins produced (depending on their stability) in order to perform a second measurement on the same cells. Multiple measurements are usually performed on different batches of cells [19, 20] or separated by a certain time (days) [21].

Finally in this work, we investigated different approaches to exploit chemotaxis in order to produce biosensing signals. It is the first time that this universal behavior is used in order to quantify chemical compound in a biosensory perspective. Our results are promising and show that functional biosensors based on chemotaxis may be achieved using a variety of approaches and produce different types of detectable signals.

## Reference

1. Rothbauer M, Wartmann D, Charwat V, & Ertl P (2015) Recent advances and future applications of microfluidic live-cell microarrays. *Biotechnol Adv* 33(6):948-961.
2. Wessel AK, Hmelo L, Parsek MR, & Whiteley M (2013) Going local: technologies for exploring bacterial microenvironments. *Nat Rev Microbiol* 11(5):337-348.
3. Lim JW, Ha D, Lee J, Lee SK, & Kim T (2015) Review of micro/nanotechnologies for microbial biosensors. *Front Bioeng Biotechnol* 3:e61.
4. Ahmed T, Shimizu TS, & Stocker R (2010) Microfluidics for bacterial chemotaxis. *Integr Biol (Camb)* 2(11-12):604-629.
5. Tecon R & Van der Meer JR (2008) Bacterial biosensors for measuring availability of environmental pollutants. *Sensors (Basel)* 8(7):4062-4080.
6. Kim S, Kim HJ, & Jeon NL (2010) Biological applications of microfluidic gradient devices. *Integr Biol (Camb)* 2(11-12):584-603.
7. Alford SC, Abdelfattah AS, Ding Y, & Campbell RE (2012) A fluorogenic red fluorescent protein heterodimer. *Chem Biol* 19(3):353-360.
8. Alford SC, Ding Y, Simmen T, & Campbell RE (2012) Dimerization-dependent green and yellow fluorescent proteins. *ACS Synth Biol* 1(12):569-575.
9. Sourjik V & Berg HC (2002) Receptor sensitivity in bacterial chemotaxis. *Proc Natl Acad Sci U S A* 99(1):123-127.
10. Cui B, Wang Y, Song Y, Wang T, Li C, Wei Y, Luo ZQ, & Shen X (2014) Bioluminescence resonance energy transfer system for measuring dynamic protein-protein interactions in bacteria. *MBio* 5(3):e01050-01014.
11. Armitage JP & Macnab RM (1987) Unidirectional, intermittent rotation of the flagellum of *Rhodobacter sphaeroides*. *J Bacteriol* 169(2):514-518.

12. Mitchell JG, Pearson L, Dillon S, & Kantalis K (1995) Natural assemblages of marine bacteria exhibiting high-speed motility and large accelerations. *Appl Environ Microbiol* 61(12):4436-4440.
13. Stocker R, Seymour JR, Samadani A, Hunt DE, & Polz MF (2008) Rapid chemotactic response enables marine bacteria to exploit ephemeral microscale nutrient patches. *Proc Natl Acad Sci U S A* 105(11):4209-4214.
14. Derr P, Boder E, & Goulian M (2006) Changing the specificity of a bacterial chemoreceptor. *J Mol Biol* 355(5):923-932.
15. Looger LL, Dwyer MA, Smith JJ, & Hellinga HW (2003) Computational design of receptor and sensor proteins with novel functions. *Nature* 423(6936):185-190.
16. Bi SY, Pollard AM, Yang YL, Jin F, & Sourjik V (2016) Engineering hybrid chemotaxis receptors in bacteria. *Acs Synthetic Biology* 5(9):989-1001.
17. Di Giacomo R, Krodel S, Maresca B, Benzoni P, Rusconi R, Stocker R, & Daraio C (2017) Deployable micro-traps to sequester motile bacteria. *Sci Rep* 7:e45897.
18. Tandogan N, Abadian PN, Epstein S, Aoi Y, & Goluch ED (2014) Isolation of microorganisms using sub-micrometer constrictions. *PLoS One* 9(6):e101429.
19. Siegfried K, Endes C, Bhuiyan AF, Kuppardt A, Mattusch J, van der Meer JR, Chatzinotas A, & Harms H (2012) Field testing of arsenic in groundwater samples of Bangladesh using a test kit based on lyophilized bioreporter bacteria. *Environ Sci Technol* 46(6):3281-3287.
20. Buffi N, Beggah S, Truffer F, Geiser M, van Lintel H, Renaud P, & van der Meer JR (2016) An automated microreactor for semi-continuous biosensor measurements. *Lab Chip* 16(8):1383-1392.
21. Elad T, Almog R, Yagur-Kroll S, Levkov K, Melamed S, Shacham-Diamand Y, & Belkin S (2011) Online monitoring of water toxicity by use of bioluminescent reporter bacterial biochips. *Environ Sci Technol* 45(19):8536-8544.







# CURRICULUM VITAE

Name	Clémence
Surname	Roggo
Birthday	13 <sup>th</sup> of March 1989 (Morges, Switzerland)
Origin	Fribourg, Switzerland

## **2012 - 2017**

PhD student  
Department of Fundamental Microbiology  
Faculty of Biology and Medicine  
University of Lausanne, Switzerland

## **2010 - 2012**

Master of Science (MSc) in Molecular Life Sciences  
Thesis title: Identification of genes involved in the water stress response in *Sphingomonas wittichii* RW1  
Best Master Project Award  
Director: Jan Roelof van der Meer  
Department of Fundamental Microbiology  
University of Lausanne, Switzerland

## **2007 - 2010**

Bachelor of Science (BSc)  
University of Lausanne, Switzerland

## **AWARDS**

UNIL DDay 2016, best poster Award (Lausanne, Switzerland, 2016)

Batsheva de Rothshild Seminar on New Concepts in Biosensing, best presentation Award (Dead Sea, Israel, 2017)

## LIST OF PUBLICATIONS

**Roggo, C.**, and van der Meer, J.R., *Miniaturized and integrated whole cell living bacterial sensors in field applicable autonomous devices*. *Curr Opin Biotechnol*, 2017. **45**: p. 24-33.

Miyazaki, R., Bertelli, C., Benaglio, P., Canton, J., De Coi, N., Gharib, W.H., Gjoksi, B., Goesmann, A., Greub, G., Harshman, K., Linke, B., Mikulic, J., Mueller L., Nicolas, D., Robinson-Rechavi, M., Rivolta, C., **Roggo, C.**, Roy, S., Sentchilo, V., Siebenthal, A. V., Falquet, L., van der Meer, J. R., *Comparative genome analysis of Pseudomonas knackmussii B13, the first bacterium known to degrade chloroaromatic compounds*. *Environ Microbiol*, 2015. **17**(1): p. 91-104.

Coronado, E., **Roggo, C.**, and van der Meer, J.R., *Identification of genes potentially involved in solute stress response in Sphingomonas wittichii RW1 by transposon mutant recovery*. *Front Microbiol*, 2014. **5**: p. 585.

**Roggo, C.**, Coronado, E., Moreno-Forero, S.K., Harshman, K., Weber, J., and van der Meer, J.R., *Genome-wide transposon insertion scanning of environmental survival functions in the polycyclic aromatic hydrocarbon degrading bacterium Sphingomonas wittichii RW1*. *Environ Microbiol*, 2013. **15**(10): p. 2681-95.

Coronado, E., **Roggo, C.**, Johnson, D.R., and van der Meer, J.R., *Genome-Wide Analysis of Salicylate and Dibenzofuran Metabolism in Sphingomonas Wittichii RW1*. *Front Microbiol*, 2012. **3**: p. 300.

# LIST OF CONFERENCES

## 2012

An international workshop on systems and synthetic Biology, Mallorca, Spain (Poster presentation)

## 2013

71<sup>st</sup> Annual congress of the Swiss Society of Microbiology, Interlaken, Switzerland (Poster presentation)

10<sup>th</sup> Horizons in Molecular Biology, Göttingen, Germany (Poster presentation)

## 2014

LS<sup>2</sup> Annual Meeting 2014, Lausanne Switzerland (Poster presentation)

72<sup>st</sup> Annual assembly of the Swiss Society of Microbiology, Grange-Paccot, Switzerland (Poster presentation)

15<sup>th</sup> International Symposium on Microbial Ecology (ISME15), Seoul, South Korea (Poster presentation)

## 2015

73<sup>rd</sup> Annual assembly of the Swiss Society of Microbiology, Lugano, Switzerland (Oral and poster presentation)

13<sup>th</sup> symposium on bacterial Genetics and Ecology (BAGECO), Milano, Italy (Poster presentation)

## 2016

74<sup>th</sup> Annual assembly of the Swiss Society of Microbiology, Bern, Switzerland (Oral and poster presentation)

BRAAVOO Marine Biosensors Workshop, Villars-sur-Ollon, Switzerland (Oral presentation)

## 2017

Batsheva de Rothschild Seminar on New Concepts in Biosensing,, Dead Sea, Israel (oral presentation)



# ACKNOWLEDGEMENTS

I want first to thank my thesis director, Jan Roelof van der Meer, who gave me the opportunity to work in his lab and to start a PhD on a very exciting and multi-disciplinary project. Thanks you sincerely for everything, your support, your advices and your infinite positivism.

Good science can be achieved only in a pleasant environment. So thanks to all group members, first the former ones: Artur, François, Sandra, Ryo, Silvia, Davide, Nicolas, Erika, Eric and Berra, as well as the current members: Andrea, Marian, Birge, Siham, Noushin, Vitali, Manu, Yves, Nicolas, Diogo, Renyi and Vladimir. I want also to thank the administrative staff of the department who really helps us to focus on science: Nadine, Aline, Nazife, Maria and Lydie. The DMF is a fantastic place to work and to meet amazing people, so thanks to all collaborators of the department. A special thanks to Serge Pelet who let me use his microscope for my pHLuorin experiments.

I acknowledge all the students who participated to this project for a summer project or a master project: Giulia, Lavinia, Lionel and Duygu. I am especially grateful for Roxane who did her long Master project with me. Even if her project was not very successful, she was always kept her motivation. Actually she will continue with a PhD in this lab, which is also a kind of great success for me.

I am also grateful for the CMI staff members of the cleanroom in EPFL who taught me how to work with the machines and how to produce my own microfluidic chips, as well as the Envirobot project members, especially Harald, for the discussions during our meetings.

I also acknowledge the members of my committee: the experts, Victor de Lorenzo and Victor Sourjik and the president Bengt Kayser.

Finally I am sincerely grateful for my family, my parents, who always supported me, financially and morally, during my long studies, as well as my brother and Anne-Laure. And of course, Eric, who had to support me even in the worse moments but he was always present and helped me a lot to be more self-confident.

